Solar Polarimetry: Techniques and Applications

A Thesis

Submitted for the Degree of

Doctor of Philosophy

In

Faculty of Physics

Bangalore University

By

K. Sankarasubramanian

Indian Institute of Astrophysics

Bangalore 560 034, India

August, 2000

Declaration

I hereby declare that this thesis, submitted to Bangalore University, Bangalore, for the award of a Ph.D. degree, is a result of the investigations carried out by me at Indian Institute of Astrophysics, Bangalore, under the supervision of Professor P. Venkatakrishnan. The results presented herein have not been subject to scrutiny, by any university or institute, for the award of a degree, diploma, associateship or fellowship whatsoever.

K. Sankarasubramanian
(Ph.D. Candidate)

Indian Institute of Astrophysics
Bangalore 560 034, India
August 20, 2000

Certificate

This is to certify that the thesis entitled **'Solar Polarimetry: Techniques and Applications'** submitted to the Bangalore University by **Mr. K. Sankarasubramanian** for the award of the degree of Doctor of Philosophy in the faculty of Physics, is based on the results of the investigations carried out by him under my supervision and guidance, at the Indian Institute of Astrophysics. This thesis has not been submitted for the award of any degree, diploma, associateship, fellowship, etc. of any university or institute.

Prof. P. Venkatakrishnan
(Supervisor)

Bangalore 560 034
August, 2000

To my beloved parents and cute sisters

Acknowledgments

It is my great pleasure to thank my supervisor Prof. P. Venkatakrishnan for his valuable guidance through out this work. He gave me lots of encouragement and confidence in pursuing this thesis whenever I was stuck with some problem. Apart from the scientific discussions, the lunch time discussions we had in his house with his family is another great inspiration in successfully completing this thesis. I thank his family members for this.

I thank Prof. Ramanath Cowsik, Director, Indian Institute of Astrophysics, for all the facilities provided to me. I thank the chairman and members of the Board of Graduate studies for all their help during my stay at IIA and their help in connection with the Bangalore University formalities.

I thank Prof. Anandaram, the Chairman, Physics department, Bangalore university and also the earlier Chairmen, for their cordial and smooth manner in which the formalities related to the University were conducted. The discussion with them was invaluable in the smooth progress with the Bangalore University.

I thank the photonics section of IIA for lending me some of the valuable items. I thank Mr. J. P. A. Samson and Mr. P. K. Mahesh for their engineering design for the polarimeter and the ellipsometer used for this thesis. The mechanical work of Mr. Sagayanathan is very much appreciated. The very precise movement control which he made for our ellipsometer and polarimeter is wonderful.

I thank the observing staff Mr. P. Devendran and Mr. Hariharan at the tunnel telescope of the Kodaikanal Observatory, for their efficient assistance and also for providing a very friendly atmosphere. They taught me some of the observing tactics which they learned through their experience. I also thank the mechanical staff at Kodaikanal Observatory and Mr. Jayavel for their help in assembling the polarimeter and the ellipsometer. I thank the resident scientist of Kodaikanal Observatory, Dr. S. S. Gupta and the other scientific and non-scientific staff for teaching me some of the solar physics and taking care of my stay at Kodaikanal in those happy as well

as depressing periods.

I specially thank the scientific staff at Sacramento-Peak Observatory, particularly Drs. Thomas Rimmele, K. S. Balasubramaniam, Michael Sigwarth and Richard Radick for their sharing of knowledge with me. The ASP-inversion code which I learned from them was very useful and it has been used in this thesis. I also thank, Drs. Bary LaBonte and Richard Canfield for providing me the Mees Solar Observatory (MSO) data to compare with our results. I thank the people who were involved in obtaining the data at MSO.

The Faculty and the scientific staff of IIA are thanked for their support. The collaboration with Drs. K. E. Rangarajan and K. B. Ramesh gave some valuable data presented in this thesis. I thank for their help. I also thank Dr. K. E. Rangarajan for his help in correcting my thesis. The help of the Librarian Ms. A. Vagiswari and the library staff members are acknowledged. The library with the wealth of knowledge in the form of books and journals is one of the helping hands whenever I had doubts related or unrelated to this thesis. The Computer Center (CC) headed by Mr. A. V. Ananth is another source of knowledge with the fast internet facility and fast data processing units. The help rendered by Mr. J. S. Nathan is acknowledged with gratitude. I also thank Mr. K.T. Rajan, Mrs. Pramila, Mr. S. B. Ramesh, Mr. Mohan Kumar, Mr. Nagaraj, Mr. K. Sankaranarayanan (Telephone exchange) and Mr. Md. Khan for their good services right from my first days at IIA.

I thank Mr. P.N. Prabhakara, Mr. D. Kanagaraj and Thiyagaraj who took care of the photocopying and binding of this thesis. I thank all of them profusely for their help. I thank the staff club of IIA for providing us the recreation to refresh our minds.

I thank my beloved seniors, especially Drs. V. Krishnakumar, R. Ramesh, and Ms. T. Sivarani in giving me company when I was in need. Also, they helped me by giving advises in depressing days. I thank all my batch mates, Rajesh, Pavan, Sonjoy, Jana and Mangala for their wonderful company in the first and the subsequent years. I still remember those first year when we used to discuss together and also play TT,

Kabadi for relaxing.

As a senior most student now, I have quite a number of juniors who gave me company. I thank the company of Mr. R. Sridharan, my hostel room-mate. Also, the cricket playing group, Nagaraj, Dharam, Manoj, Ravindra, Kathiravan, Maheswar, Ravinder, and Sahoo are thanked for bearing with me. Apart from cricket, the volleyball group, Selvam, Muralidass, Mani, and Mohan are thanked. The friendship of Mrs. K .P .Geetha is acknowledged. The lovely environment provided by Raji, Suresh, Preeti, Geetanjali, Latha, Ambika, Ramachandra, Rabbi, Shanmuga Sundaram, Srik, Rajaguru, and Shalima cannot be forgotten. My office room-mate Swara and my office neighbor Pandey are thanked for their discussions of Astrophysics outside my thesis topic.

I thank my friends at IISc for their help in using the facilities at IISc and their lively company. I thank my friends at Institute for Plasma Research for giving me some technical details and encouragement. I thank the staff members of Udaipur Solar Observatory (USO) and the students at USO for their help in my stay at USO during the thesis writing phase. Some of the discussions with the scientific staff at USO helped in enhancing the quality of the thesis. I owe a lot of thanks to all my friends all of whom I cannot name because of space constraint.

I thank my pet sister Miss. S. Lakshmi for her encouragement during the last phase of my work. Also, I thank my cousin sister at Bangalore for the company she gave when I was in need.

Finally, but not the least, I thank my family for whom this thesis is dedicated. Without their encouragement and support it would have been very difficult to finish this thesis. They gave me enough support without bothering me which made me to concentrate on the work much more than what I could have. I thank all of them for this. I hope they will continue their support in the same way in the coming years to give me enough confidence.

Solar Polarimetry: Techniques and Applications

Abstract:

Magnetic fields on the sun play a major role in the physical processes which are observed. The only consistent way to study the magnetic fields is through polarimetry even though qualitative information about it can be obtained using a narrow band imaging. The polarisation of any source can be specified completely by the Stokes parameters. The Stokes parameters observed along the spectral profile (called as Stokes profiles) completely specifies the field configuration present in the observing region. The observation of the complete Stokes profiles brings out the magnetic field configuration more accurately. However, this requires a high dispersion spectrograph and a polarimeter with a symmetric telescope in order to keep the instrumental polarisation minimum. With the availability of an existing high dispersion spectrograph at the Kodaikanal Tower Telescope (KTT), it is possible to observe the Stokes profiles. However, the oblique reflection of the coelostat at KTT complicates the measurement as the instrumental polarisation corrupts the incoming radiation. Hence, a systematic study of the instrumental polarisation is needed in order to bring out the uncorrupted Stokes profiles from the observation.

Once the observed profiles are corrected for the instrumental polarisation, an inversion of the polarimetric data is needed to determine the magnetic field. This inversion depends on the process of line formation involving polarised radiative transfer. The problem gets complicated if the observing region is more complex in nature. From the low spatial resolution point of view, the vector magnetic field derived with a zeroth order approximation of the model atmosphere appear fairly consistent considering the simplicity of the computer codes used. These field values can be used to map the magnetic field region of a sunspot. A systematic study of these magnetic regions can bring out some of the key features which are needed to understand the role played

by the magnetic field in solar phenomenon. Also, the energetic processes like flares and coronal mass ejections which affect the earth directly, can be studied with such a measurement. This requires a long term observations of different sunspots.

Contents

List of Figures

List of Tables

Chapter 1

INTRODUCTION

1.1 General Introduction

The physical properties of the stellar atmosphere can be studied only through the photons received from them. The photon has three basic principle properties which contain the information about the source,

- The energy content of the photon for different wavelength bands like Ultra Violet (UV), Visible, Infra Red (IR) etc.
- The relative absorption of photons at a spectral line because of atoms present in the atmosphere.
- The polarisation state of the light.

The first principle which is known as photometry in general gives information about the temperature of the source. The second principle known as spectroscopy gives a wealth of information about the abundance of different elements present in the stellar atmosphere. These two put together is used to test all the stellar theory including the behavior of stars of different mass at different stages of evolution in the

HR diagram. The third principle, which was later employed, added more information about the magnetic fields present as well as the scattering processes involved in the atmosphere. In effect, it decides the validity of certain assumptions used in the general stellar theory. The assumption of no magnetic field and LTE can become very crude in certain regime. For example, photosphere of the sun has different structures primarily due to the presence of magnetic field and the assumption of LTE is no longer valid in chromosphere and corona. Hence, for refined models, study of the influence of magnetic fields and the non-LTE theory is important.

1.2 Representation of Polarised Light

The polarisation state of light can be completely specified by four quantities called the Stokes parameters. They are represented as $[I, Q, U, V]^T$ where superscript 'T' represents the transpose operation. These four parameters have the units of intensity and corresponds to a time-averaged intensity which is the observable in any experiment. The first parameter 'I' is the total intensity of the light which contains both polarised part and unpolarised part in partially polarised light. Q and U represents the linear polarisation state of the source whereas V represents the circular polarisation state. Any partially elliptically polarised light, which is the most general case, can be expressed in terms of the sum of a completely unpolarised component and a completely elliptically polarised component. The former component will have only intensity I_{up}, where the subscript '*up*' means 'unpolarised', whereas the later component will have all the four components with non-zero values. The intensity, I_p corresponds to the polarised intensity and is related to the other three components as,

$$I_p = \sqrt{Q^2 + U^2 + V^2} \tag{1.1}$$

The completely elliptically polarised component can in turn be split into a linear component plus a circular component and hence Q, U and V will have non-zero values.

This is the most general case and the specific case of completely linearly polarised light can be represented by zero value of V and the circularly polarised case by zero values of Q and U. Hence, the complete specification of the polarisation state requires the measurement of all the four Stokes parameters.

1.2.1 Mueller Matrix

Any optical system used to measure the polarisation state of the light can be represented by a 4×4 matrix called Mueller matrix (Gerrard and Burch, 1975; Mueller, 1948). The output and the input Stokes vector for the optical system is related through this Mueller matrix as,

$$I_{out} = MI_{in}. \tag{1.2}$$

Where I_{out} and I_{in} are the four component input and output Stokes vector. Each of an optical element say polaroid, quarter-wave plate (QWP), and etc. can be represented by a single Mueller matrix for polarisation measurement. If an optical system has a train of optical elements say $\epsilon_1, \epsilon_2, ..., \epsilon_n$ with the first element close to an input source, the overall Mueller matrix of the optical system can be constructed by multiplying in order, the Mueller matrix of each element. *i.e.*,,

$$M = M_n.....M_2M_1. \tag{1.3}$$

M is the combined Mueller matrix & M_1, M_2, ..., M_n are the Mueller matrices of the optical elements 1, 2,...,n respectively.

Mueller calculation makes the calibration of the optical system much easier for polarisation measurement. To calibrate any optical system, the combined Mueller matrix need to be calculated. Ideally, an identity matrix is preferred for the optical setup in order to get the input Stokes profile exactly at the output. However, in practice, the Mueller matrix is never going to be an identity matrix. This deviation from the identity matrix can be corrected off-line by multiplying the inverse of the

measured Mueller matrix with the observed Stokes parameters. From Equation 1.2, it can be seen that,

$$I_{in} = M^{-1} I_{out} \tag{1.4}$$

1.3 Solar Magnetic Fields

It is now realised that most of the physical processes happening on the outer layers of the sun are governed by magnetic fields. All the manifestations of solar activity like sunspots, plages, pores, flares, prominences, spicules, are caused by magnetic fields. Apart from these structures, there are diffuse magnetic structures like a background magnetic field on the sun (Stenflo, 1973). The presence of bright points associated with magnetic activity proposes the need for high-resolution studies since the observed bright points have sizes smaller than the diffraction limit of the biggest telescope available currently (Muller, 1985). These small scale magnetic features are predicted to be associated with the heating of the upper layer of the solar atmosphere (Van Ballegooijen, 1986). The physical processes behind the formation of these different scale structure is not yet clearly understood (Thomas, 1992). Whether the large scale structure like sunspot is formed by the segregation of small-scale fields or the small-scale structure is formed by the breaking up of the large scale structure is not yet clear.

However, it is well understood that the magnetic field plays an important role in the energy balance of the atmosphere of sun as well as stars, particularly, the solar-type stars. It is now generally believed that solar magnetic fields are produced by dynamo processes at the base of the convection zone and they emerge in the form of flux loops giving rise to the observed magnetic activity (Parker, 1955; Zwann, 1978; Parker, 1984). In order to understand the various physical mechanisms which form different structures on the solar surface at different scales, it is necessary to quantitatively study the magnetic fields. Although qualitative information on the presence

of magnetic fields and the shapes of the field lines can be obtained by observing the shapes of the emission structures with filters at various wavelengths, quantitative information requires polarisation measurements.

1.4 Solar Polarimetry

Solar polarimetry is the study of the polarisation state of light received from the sun. The only consistent way of studying the magnetic fields on the sun is through polarimetry (Stenflo, 1994). There are two possible mechanisms adapted until now to study the magnetic fields present on the sun. They are,

- Zeeman effect, to study the strong magnetic fields.
- Hanle effect, to study the weak diffuse background magnetic fields.

1.4.1 Zeeman Effect

Zeeman effect is the splitting of a spectral line when an atom emitting or absorbing light is subjected to a magnetic field (Zeeman, 1896; White, 1934). The magnetic field causes the splitting of atomic energy levels due to precession of the atom around the magnetic field axis. In other words, the Zeeman effect capitalises on lifting of the degeneracy of atomic eigenstates by magnetic fields. Figure 1.1 shows a schematic picture of the classical analogue of an atomic system as a three-axis damped oscillator having a resonant frequency ν_0 of the spectral line. The atomic oscillator is represented by a system consisting of a linear oscillator along the direction of the magnetic field vector $\mathbf{B}$ (called as the π component) plus two circular oscillators of opposite directions, both lying in a plane perpendicular to $\mathbf{B}$ (called as the σ components and represented as σ_R and σ_L).

Figure 1.1 shows two different configurations of interaction of the oscillator with incident electro magnetic radiation, one is called as longitudinal Zeeman effect (top

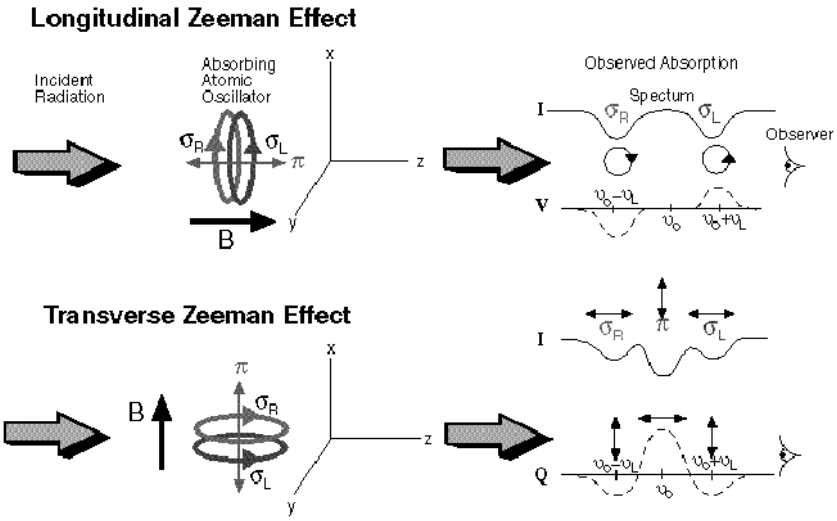

Figure 1.1: A classical analogue of the atom as an oscillator to illustrate the Zeeman effect. This figure is obtained from the High Altitude Observatory (HAO) website (*http://www.hao.ucar.edu/public/research*). See the text for details.

figure) and the other as transverse Zeeman effect (bottom figure). The longitudinal Zeeman effect occurs when a plane wave propagating in the direction of **B** excites both circular modes, σ_R and σ_L, corresponding to right- and left- circular polarisation respectively. This excitation leads to the absorption of circularly polarised light at $\nu_0 \mp \nu_L$ where ν_L is the well known Larmor frequency ($\nu_L = \mathrm{e}\mathbf{B}/4\pi\mathrm{mc}$, e and m are the electronic charge and mass respectively). In this special case, the incident electro magnetic wave has no oscillatory component along the linear oscillator parallel to **B** (since the electro magnetic waves are transverse in nature). Hence, absorption of the π component cannot occur. Because the background continuum is unpolarised, the absorption of right-(left-) circular polarisation results in an excess of left-(right-) circular polarisation as shown in Figure 1.1. In the other special case of transverse Zeeman effect, the propagating wave excites both the σ and π components. The

latter is unshifted in wavelength by the magnetic field. The former is shifted in wavelength according to the Larmor frequency but is linearly polarised rather than circularly polarised. The direction of linear polarisation for this transverse case is depicted in the bottom figure of Figure 1.1. In general, where **B** can be in any direction, both longitudinal and transverse Zeeman effects act together. The shapes of the Stokes profiles of Zeeman sensitive spectral lines contain the information about the full vector **B**. However, there is an uncertainty of 180° in the calculation of the azimuthal field since the transverse Zeeman effect is similar for an azimuthal field configuration separated by 180°. Note that this classical picture is applicable only to the normal Zeeman effect where the transition is from $\mathbf{J} = 0$ to $\mathbf{J} = 1$ which makes the spectral line split into three.

For a normal Zeeman effect, the amount of splitting, $\Delta\lambda_B$ (in Å) is proportional to the magnetic field strength and is given by,

$$\Delta\lambda_B = 4.67 \times 10^{-13} \lambda_0^2 g B, \tag{1.5}$$

where λ_0 is the central wavelength in Å and B is the field strength in Gauss. 'g' is the Lande factor of the upper energy level. Under the Russel-Saunders coupling (Condon and Shortley, 1935; White, 1934),

$$g = 1 + \frac{J(J+1) + S(S+1) - L(L+1)}{2J(J+1)}.$$

Where L, S and J are the angular momentum, spin angular momentum and total angular momentum quantum numbers of the atomic states involved in the transition, respectively.

The Zeeman effect studied in the laboratory, which is called here as direct Zeeman effect, can be applied only to emission lines. Fraunhofer lines formed in the solar atmosphere are absorption lines. They display the so called *inverse Zeeman effect*, where the polarisation sense is reversed. The Zeeman pattern shown in Figure 1.1

actually corresponds to the inverse Zeeman effect. The differences between the direct and the inverse Zeeman effect are (Ye Shi-hui, 1994),

- For the longitudinal magnetic field, the direction of circular polarisation for the corresponding two σ components are opposite.
- In the transverse magnetic field, the direction of polarisation of the π and σ components provided by the direct and inverse effects are perpendicular to each other.
- In the transverse field, the two σ components of the inverse Zeeman effect are only partially polarised, while for the direct effect the polarisation is complete.
- In the case of inverse Zeeman effect, the azimuth of the observed polarisation is the same as that of the magnetic field present.

In this thesis the magnetic field is studied using absorption lines and we have used the term Zeeman effect rather than the term inverse Zeeman effect. The actual situation in stellar atmosphere is more complex than the case of pure Zeeman effect. This is due to the following reasons,

- Stellar atmosphere can simultaneously absorb, scatter and re-emit radiation and also the scattering need not be coherent.
- The magnetic fields are not strong enough to completely split the line, at least in the optical region, for the observation of sun where the Doppler broadening is more than the magnetic splitting.
- The inhomogeneity of stellar atmosphere and the presence of magnetic field makes it much more difficult to infer the physical conditions present in them.

For the sun, the direct way of finding the splitting is possible only in IR wavelength region because the Doppler broadening in the visible region is more than the magnetic field splitting. As shown in Figure 1.1, in Zeeman effect, apart from the splitting of the

spectral line, the σ and π components exhibit a characteristic circular (Stokes V) or linear (Stokes Q & U) polarization. The state of polarisation depends on the strength of the magnetic field and its orientation with respect to the line of sight. Hence, the Zeeman effect is a method of choice for diagnosing the presence of magnetic fields that are sufficiently strong (in excess of a few hundred Gauss) to compete with the micro-turbulent Doppler broadening of the line profiles.

1.4.2 Hanle Effect

A different class of polarisation effects, due to coherent scattering can also be used for magnetic field diagnostics. Like the blue sky is polarised due to Rayleigh scattering by molecules, certain lines in the solar spectrum become polarised when they are partly formed by coherent scattering. When a magnetic field is present in a coherent scattering system, the precession of the atom induces a modification called the Hanle effect of this scattering polarisation. Hanle effect reduces the degree of polarisation produced by the coherent scattering and rotates the plane of polarisation. Figure 1.2 shows a picture of the classical analogue of an atom as an oscillator to illustrate the Hanle effect.

Three criteria must be fulfilled in order for the Hanle effect to be operative,

- The Larmor frequency must satisfy the condition, $\nu_L \approx \ \mathrm{A}_{ij}$, where A_{ij} is the spontaneous emission rate of the atomic transition.
- The plasma densities must be low enough and the radiation intensity must be high enough that radiative excitation of the atom is more common than collisional excitation.
- The radiation field incident upon the scattering atoms must be anisotropic.

Figure 1.2(a) represents a scattering system illuminated anisotropically by a plane wave propagating along the x-axis. Assume the magnetic field is along the y-axis and

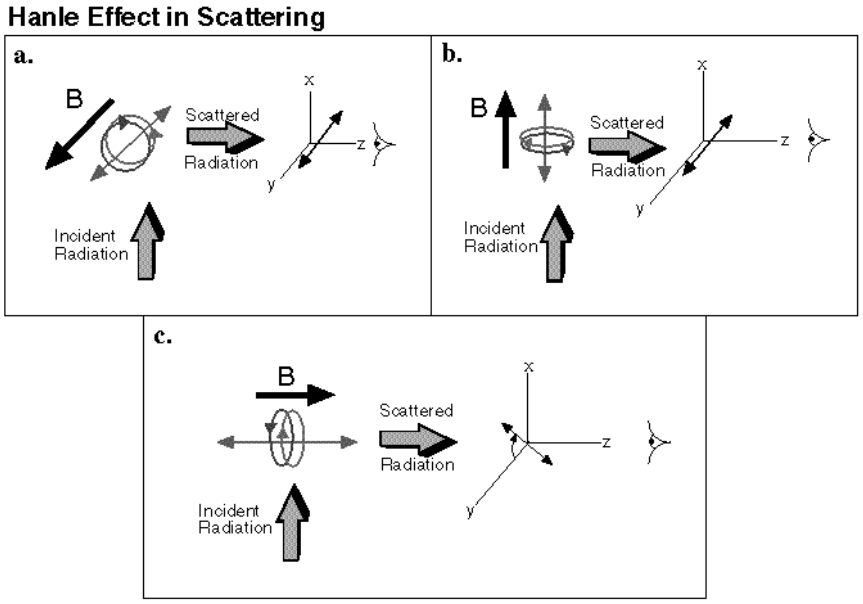

Figure 1.2: Classical analogue of the atom as an oscillator to illustrate the Hanle effect. This figure is taken from the HAO web page. See the text for details.

the observer is positioned along the z-axis. Similar to Zeeman effect, the atomic system is represented by a combination of a linear oscillator along y-axis and two oppositely rotating circular oscillators in the x-z plane. For pure scattering in the absence of magnetic field, the observer would measure a linear polarisation parallel to the y-axis. In the presence of magnetic field, the field-aligned state mixes with the circular states causing some re-emission polarised along the x-axis and hence reduces the net polarisation of the scattered radiation. In the case of Figure 1.2(b), the magnetic field mixes the radiatively excited circular oscillator states into linear oscillator state aligned with the magnetic field and hence depolarisation occurs. A very interesting special case is depicted in Figure 1.2(c) where the field is aligned along

the line of sight (along z-axis). A pure scattering in the limit of no magnetic field, results in observed linear polarisation along y-axis since both the circular states are excited in phase with the resultant oscillation perpendicular to the line of sight. The magnetic field alters the phase relation between these two oscillators, and the finite life time of the re-emission process causes the damping of both circular oscillators. This time-dependent variation of the oscillators results in both a reduction of net polarisation and a rotation of the plane of polarisation.

For a complete understanding of the Zeeman and Hanle effect applied to the sun, refer to the book by Stenflo (1994). This thesis deals only with the Zeeman effect and hence Hanle effect will not be discussed anymore except in the last chapter highlighting the potential application of Hanle effect in diagonising weak magnetic fields in the solar atmosphere.

1.5 Solar Polarimetry: Techniques

The first detection of magnetic field on heavenly bodies was done by Hale, 1908 even though it was predicted by several authors before him (Bigelow, 1889; Schuster, 1892; Stromer, 1892). Hale measured the magnetic field in a sunspot by measuring the amount of circular polarisation in the wings of a spectral line. From observations of the magnetic field on the entire sun, he first arrived at the conclusion that the general magnetic field of sun is about 50 Gauss. The observations of Hale were put on a sound theoretical basis by Sears (1913). He developed the Sears formula to understand the magnetic configuration of sunspots from the observed Stokes profiles.

The technical developments of the instrument for the vector magnetic field study is very interesting to look at. After the demonstration of the Zeeman effect in the sunspot by Hale, the real improvement in the measurement accuracy was given by Babcock in 1953 (Babcock, 1953) with his longitudinal magnetograph. The famous Babcock magnetograph measures the line of sight magnetic field with greater accu-

racy and better technique compared to the earlier techniques. The development of an electro-optic modulator using a birefringent crystal, helped Babcock to design an instrument which operates as fast as 50MHz to beat the seeing variations and hence in the improvement of the polarisation accuracy. In his work, the polarisation of the beam was modulated at the entrance slit of the spectrograph with the help of an electro-optic modulator followed by a polariser to alternately isolate the right and left circular polarisation from the spectral line wings. Photomultipliers at the exit slits detected the circular polarisation which was then fed to a differential amplifier whose output signal was proportional to the magnetic field. Babcock's magnetograph was able to measure fields up to about 20 G in the lower limit. Using the magnetograph, he produced maps of the general magnetic field on the sun. Instruments similar to Babcock's magnetograph has been developed since then and used in several observatories until now. However, the limitation of his system is that it can produce only the line of sight magnetic field.

The first transverse magnetic field was measured by Severny and his co-workers at the Crimean astrophysical observatory (Stepanov and Severny, 1962; Severny, 1964a; Severny, 1964b; Severny, 1965). This transverse magnetograph was a modification of an existing longitudinal magnetograph at the $\lambda\lambda$5250.2Å spectral line. A quarter-waveplate (QWP) was introduced in addition to the existing quarter wave electro-optic modulator, to achieve, a half-wave modulation to detect the linear polarisation. The signals from the photomultipliers located at the wings of the Zeeman sensitive spectral line was added instead of subtracting them as in the Babcock's scheme.

Leighton (1959) invented a method to get the longitudinal magnetic fields at one-stroke of the entire sun. He used two spectro-heliograms recorded simultaneously in each wing of the spectral line on a photographic plate. While one spectro-heliogram is for the right circular polarisation intensities, the other is for the left circular polarisation intensities. By adding one negative photograph with the other positive photograph, the circular polarisation intensity is produced over the whole sun. The

limitation of the technique is a poor calibration of the magnetic field even though the magnetic field of the entire disk of the sun could be measured in few minutes. Apart from these, there are different techniques developed in this period to consistently study the magnetic field on the sun. The technique by Trenor, (1960) and Adams (1963) are few examples.

With the development of Fabry-Perot spectrometer (FP) and narrow band filters, it is becoming increasingly easier to record longitudinal magnetic fields almost instantaneously over an entire active region on the sun. Instrument which uses an FP or a birefringent filter to record both transverse and longitudinal magnetic fields is called a vector magnetograph. Regular maps of vector magnetic field in the form of transverse and longitudinal contour maps can be produced using the vector magnetograph (Hagyard *et al.,* 1982; Hagyard, Cumings, and West, 1983; Makita, Hamana, and Nishi, 1985; Mickey *et al.,* 1996). However, the prime limitation of this method is that the complete information is not fully extracted. Zeeman saturation occurs because of non-linear behavior of the Stokes V with the line of sight component of the magnetic field. The physical nature of the spectral line forming region is not completely extracted. However, there were attempts to use such an instrument to get the polarised line profiles in order to extract the complete physical picture of the line forming region (Balasubramaniam and West, 1991; Leka, Mickey, and LaBonte, 1999).

The other type of instrument which uses a spectrograph to record the full Stokes line profiles has the advantage of extracting the complete information including the macroscopic physical parameters like temperature, pressure etc. of the observing region. Instruments which use the full Stokes polarised line profile measurements are called Stokes polarimeters. In this case, the image or the slit of the spectrograph has to be stepped to map the two-dimensional region of interest. Hence, one complete vector magnetograph of an active region requires considerable amount of time. Currently, these two different instruments are used in different types of studies. Any

fast changing field configurations like flares can be studied through the filter magnetograph. In this case, only the change in the morphology of the field structure were studied and not the intrinsic field strength variations. The Stokes polarimetry is used to study magnetic fields which are fairly stable over a considerable amount of time. Lites, Martinez Pillet, and Skumanich (1994) discusses, the advantages and disadvantages of these two different techniques.

1.5.1 Radiative Transfer

It has been pointed out that the actual situation in the stellar atmosphere is quite complicated than the pure Zeeman effect. After the measurement of the polarised line profiles, it is needed to interpret the polarisation in terms of the magnetic field parameters like the field strength, line of sight inclination and the azimuth of the field vector. The theoretical formulation of the Zeeman effect in different atmospheric conditions were developed in the 1950's. Unno (1956) first developed the theory of polarised radiative transfer of a spectral line formed in a magnetic field. His theory is based on pure absorption and a Milne-Eddington model atmosphere. Stepanov (1960), Rachovsky (1962) and Beckers (1969) improved the theory to include the physical conditions like the magneto-optical effect. Numerical studies to include both LTE and non-LTE was made by Moe (1968) and Rees (1969).

Wittman (1974a, 1977) was the first to develop radiative transfer codes to generate the solar spectrum using a detailed model atmosphere. Starting from the basic atomic physics and quantum mechanical formulations, Landi Degl$'$ Innocenti and Landi Degl$'$ Innocenti (1972) developed the equations for the polarised radiative transfer in the most self consistent way, that included all possible physical processes. One of the problem with the spectrograph based Stokes polarimetry was the extraction of the vector magnetic field and other physical parameters from the observations by comparing it with a model atmosphere. Wittman (1974b) synthesized the Stokes profiles

and compared with the observed data. Since, the synthesis itself is a laborious, time consuming and involved process, it has not appealed as a quick and a relatively less model dependent method.

1.5.2 Inversion Techniques

The first non-linear least square method was developed by Auer, Heasely, and House (1977), called as AHH routine. In this routine, all the four observed Stokes profiles were attempted to fit with those of the profiles generated from the analytical solutions of the radiative transfer equations. The AHH routine incorporated several simplifications to the line formation in a magnetic field and had ignored the magneto-optical effects. They had effectively used a four parameter fit viz., Doppler width, the ratio of line center to the continuum optical depth, the magnetic field strength and the inclination of the magnetic field to the line of sight. Landolfi, Landi Degl′ Innocenti, and Arena (1984), refined this technique to include the magneto-optical effects and the damping parameter and called it as ALL routine. This routine used a six parameter fit to their solution.

Skumanich and Lites (1987) self consistently derived the Stokes profiles using a simple classical theory approach. A slight modification to take an exponential chromospheric rise of the source function into account was presented by Lites *et al.,* (1988). The main strength of this inversion technique lies in the simplicity of its assumption of a Milne-Eddington (ME) atmosphere. The solution of the radiative transfer equation for this atmosphere is analytic and hence it is easy to implement in a computer code. Nine parameters are used as free parameters for the inversion. The nine parameters are: two parameters to specify the source function, the *constant* magnetic field vector (described by three parameters), the line of sight velocity, the ratio of line-to-continuum absorption coefficients, the Doppler width of the line and the damping parameter. A tenth free parameter is added to account for a non-magnetic back-

ground in the observations, either by stray-light contamination or by lack of spatial resolution. This technique is used for the Stokes profiles observed with the Advanced Stokes Polarimeter (ASP) (Elmore *et al.,* 1992). This high accuracy polarimeter has given 2D maps of four Stokes parameters with high spatial and spectral resolution of entire active and quiet regions (Skumanich, Lites and Martinez Pillet, 1994; Lites *et al.,* 1995; Keppens and Martinez Pillet, 1996; Martinez Pillet, Lites and Skumanich, 1997; Lites *et al.,* 1998).

The inversion technique developed by the Zurich group is discussed in Keller *et al.,* (1990) and Solanki, Montana and Livingston (1994). They developed a methodology to use infra-red lines to measure the magnetic field (Solanki and Bruls, 1994; Solanki, 1997). This methodology allows for the variations of the physical parameters along the line of sight. They extensively used infra-red observations in order to understand the magnetic field topology (Solanki, Ruedi and Livingston, 1992a; Solanki, Ruedi and Livingston, 1992b; Solanki, Walther and Livingston, 1993; Ruedi, Solanki and Livingston, 1995).

The Stokes Inversion based on Response function (SIR) developed by Ruiz Cobo and del Toro Iniesta (1992) works independent of the initial guess value for the free parameters whereas all the other inversion technique discussed, do require a reasonable initial guess value. The distinctive feature of the SIR technique is the inclusion of the variation of the physical quantities. Inferences of stratification of all those quantities are sought. Through linearisation of the radiative transfer equation, the sensitivity of the Stokes profiles to such quantities in a first-order approximation is given by the so-called response function (RF) (Ruiz Cobo and del Toro Iniesta, 1994). RFs are indeed the main trunk of this inversion technique.

To accept a given model as a final solution, a quantitative reproduction of the Stokes profiles are needed for all the inversion techniques to check for the reliability. With the development of high polarimetric accuracy polarimeters (Elmore *et al.,* 1992; Povel, 1995), it has been recognised that there are asymmetries in the observed Stokes

profiles. These asymmetries which have long been recognised in sunspots (Moe, 1967; Beckers and Schroter, 1969; Grigorjev and Katz, 1972; Makita, 1979) are currently been seen practically everywhere in the sun particularly in the magnetic structures at all scales (Sanchez Almeida and Lites, 1992; Solanki, 1993; Martinez Pillet, Lites and Skumanich, 1997). A coherent explanation of the Stokes profile asymmetries constitute one of the most exciting and still unsolved problem to understand the dynamics of solar magnetic structures (Solanki, 1997). With the SIR technique this asymmetry problem has been addressed (Westendorp Plaza *et al.,* 1997a). The LOS variation of the physical parameters of the observed region can now be calculated from the observed Stokes profiles. In effect, a tomographic picture of an active region can be made from these observed Stokes profiles (Westendorp Plaza *et al.,* 1997b; Westendorp Plaza *et al.,* 1998.). However, this kind of inversion code needs enormous amount of computation time and hence used only in a limited way.

1.6 Motivation for this Thesis

With the success of the inversion codes, the measurement of full Stokes profiles or the Stokes polarimetry brings out much more physical insight of the active region than the vector magnetograph based systems. With the possibility of a bigger ground based telescope like Advanced Solar Telescope (AST) (*http:// www.noao.sunspot.noao.edu/ AST/*) and the success of the Adaptive Optics system (Rimmele and Radick, 1998), fast vector polarimetric measurement will be possible in the near future. With all these developments discussed above, it can be realised that a Stokes polarimeter is essential in any solar observatory in order to understand the magnetic field structure on the sun. Since, the Kodaikanal Tower Telescope (KTT) (Bappu, 1967) has a high resolution spectrograph with spectral resolution comparable to the spectrograph used by ASP, we decided to build a Stokes polarimeter at KTT.

There were attempts to build a Stokes polarimeter in India (Balasubramaniam,

1988; Ananth *et al.,* 1994). However, until now there is no consistent measurement of vector magnetic fields even though the line of sight magnetic field measurements were done successfully (Bhattacharyya, 1965; Mathew, 1998).

In this thesis, I report on the development of a Stokes polarimeter using the KTT to consistently study the magnetic field of sunspot. The main difficulty in removing the telescope polarisation because of oblique reflection is successfully handled within a percent accuracy. The limits up to which the magnetic field measurement can be carried out at the KTT have been calculated. This puts the constraint on the kind of problems one can deal with using such kinds of oblique reflecting telescope. Several techniques were developed to study different contaminations coming into the measurement of the magnetic field and ways were developed to remove it from the observed Stokes profiles in order to study the magnetic field configuration of sunspot.

The structure of the thesis is the following:

- The second chapter discusses the development of an optical method to measure the refractive indices of the mirror coatings of the KTT in order to calculate the instrumental polarisation produced by it. A computer simulation was carried out initially to understand the critical parameters involved in the measurement. The oxide layer formed on the mirror surfaces are detected.

- The development of a Stokes polarimeter using a rotating Glan-Thomson prism polaroid (GTP) and a masked CCD as a detector is discussed in third chapter. The masked CCD is used to integrate the charges inside the CCD which increases the signal-to-noise ratio and also reduces the seeing induced spurious polarisation signal. The laboratory and the field testing of the polarimeter is explained. A CCD based polarisation interferometric technique is developed to measure the retardance of the quarter-waveplate used in the Stokes polarimeter.

- Fourth chapter concentrates on the observation of Stokes profiles in the disk center to measure the daily variation of the instrumental polarisation. The model of

the KTT developed by Balasubramaniam, Venkatakrishnan and Bhattacharyya (1985) is modified to include the initial rotation from the sky plane to the plane of incidence of the first mirror. The measured data point is fitted with the model to derive the refractive indices of the coating which were then used to remove the instrumental polarisation produced during these observations. The model developed for the KTT now includes the oxide layer formed on the three mirrors of the KTT.

- Chapter five discusses the observation of a sunspot KKL 21263 (NOAA 8516) and the inversion code used to get the physical parameters for this sunspot. The complicated profiles observed in the neutral line of this sunspot are fitted with a two magnetic component model. The observations of one another sunspot and the inversion results are given in this chapter and compared with the observations taken from the Mees Solar Observatory.

- Chapter six discusses the polarisation profile obtained for the metallic lines Ti I and Sc I. These two lines are sensitive to temperature and forms only in the umbra of the sunspot. Also, this produces an anomalous Zeeman effect compared to the Fe I lines ($\lambda\lambda$ 6301.5Å and $\lambda\lambda$ 6302.5Å) which produces normal Zeeman effect. This chapter also summarises the thesis and discusses the future improvements that need to be made.

We conclude the thesis by discussing the potential use of this instrument and the limitation of the system. Even though the system as of now cannot be compared with the accuracies achieved by ASP and ZIMPOL, we suggest certain class of problems that can be studied with this instrument. Since each chapter is written in such a way that it can be understood independently, some of the repetition could not be avoided.

Chapter 2

Ellipsometry of Reflecting Mirrors

2.1 Summary

In this chapter, measurement of the Mueller matrix of each individual mirrors of the three mirror coelostat system at the Kodaikanal Tower Telescope is described. An optical method is devised using a Babinet compensator as the main optical element for the measurement of refractive indices of the mirror coatings. The importance of the oxide layer formed on the mirror coatings are demonstrated through the measurements. A model for a single mirror reflection with an aluminium coating including the oxide layer is developed.

2.2 Introduction

The Kodaikanal Tower Telescope (KTT) is a three mirror coelostat system, with each mirror having an aperture of about 61 cm (Bappu, 1967). The primary mirror is on an equatorial mount (latitude $10°14'$ N). The sunlight from the primary mirror is reflected to the secondary which in turn reflects the light vertically down to a third

mirror which is kept fixed at 45° inclination. Hence the reflected light from the third mirror will be parallel to the ground. The light then passes through a 38 cm lens which images the sun on to the slit of a spectrograph.

Any oblique reflection changes the state of polarisation of the input beam. For example, an unpolarised light incident on a dielectric surface like glass plate at Brewster angle will become completely linearly polarised after reflection (Born and Wolf, 1984) . Let R_{pa} and R_{pe} be the complex amplitudes of reflection of two orthogonally polarised waves reflected from a surface. The subscript '*pa*' and '*pe*' represents the components parallel to the plane of incidence and perpendicular to it, respectively. The plane of incidence is defined as the plane containing the incident beam, the reflected beam and the normal to the surface on which the light gets reflected. Figure 2.1 shows the variation of modulus square of R_{pa} and R_{pe} for different angles of incidence for a dielectric medium with refractive index 1.5. Variation of $|R_{pa}|^2$ and $|R_{pe}|^2$ is represented as solid and dashed line respectively in Figure 2.1. It can be seen that the reflection coefficient parallel to the plane of incidence goes to zero at a critical angle which is called as the Brewster angle. At this angle the reflected light will be completely linearly polarised in the plane of incidence.

In the case of reflection at a dielectric medium (like glass plate) mentioned above there will be only amplitude changes between the two orthogonally polarised components as shown in Figure 2.1. However, in the case of reflection at a metallic surface like an aluminum coated mirror, there will be a phase difference between the two orthogonally polarised components apart from the amplitude changes. This phase difference arises because of the complex refractive index for a metal and does change with the angle of incidence. Figures 2.2 and 2.3 show the variation of the modulus square of the complex amplitudes of reflection and the phase difference respectively for these two orthogonally polarised component. In this case, $|R_{pa}|^2$ does not go to zero for any angle of incidence and hence the reflected light will never be completely polarised. However, because of the phase difference introduced between the two or-

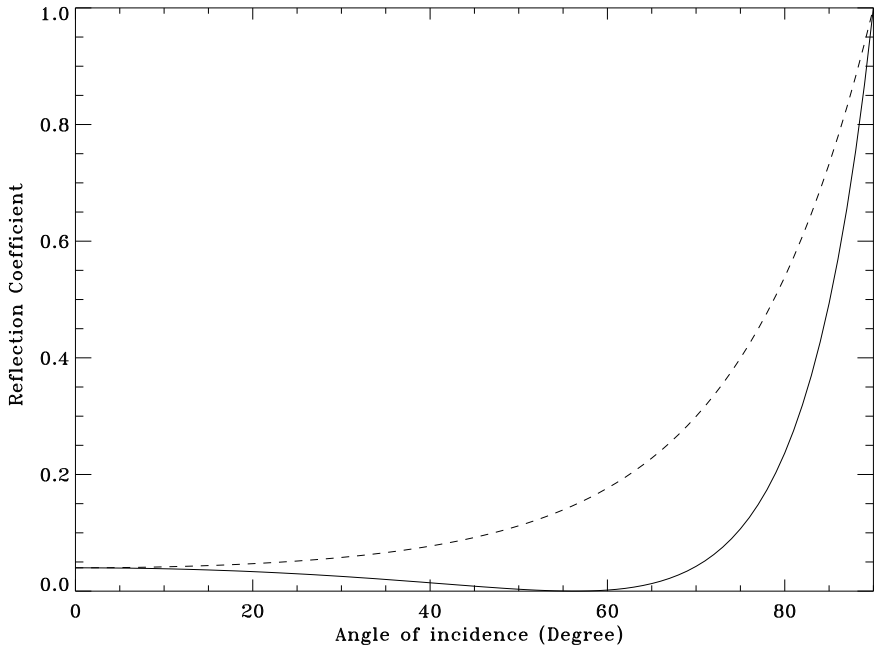

Figure 2.1: Variation of the modulus square of the complex amplitudes of reflection with angle of incidence for a dielectric medium with refractive index 1.5. The parallel component to the plane of incidence $|R_{pa}|^2$ is represented by solid line whereas the perpendicular component $|R_{pe}|^2$ is represented by dashed line.

thogonally polarised components, the reflected light will be elliptically polarised in general rather than linearly polarised as in the case of a dielectric medium.

For polarisation measurements, one should try to avoid oblique reflections and hence ideally a symmetric optical system is preferred. However, oblique reflections cannot be avoided in existing installations not originally meant for polarisation measurements. Hence the study of instrumental polarisation is essential in order to remove it from the actual polarimetric observations. Several methods have been adopted to characterise the instrumental polarisation of oblique reflecting systems (Makita and Nishi, 1970; Livingston and Harvey, 1971; Capitani *et al.,* 1989; Demidov, 1991). In general, the complete Mueller matrix of the combined system which includes all the optical components have to be found out in order to evaluate the cross-talks

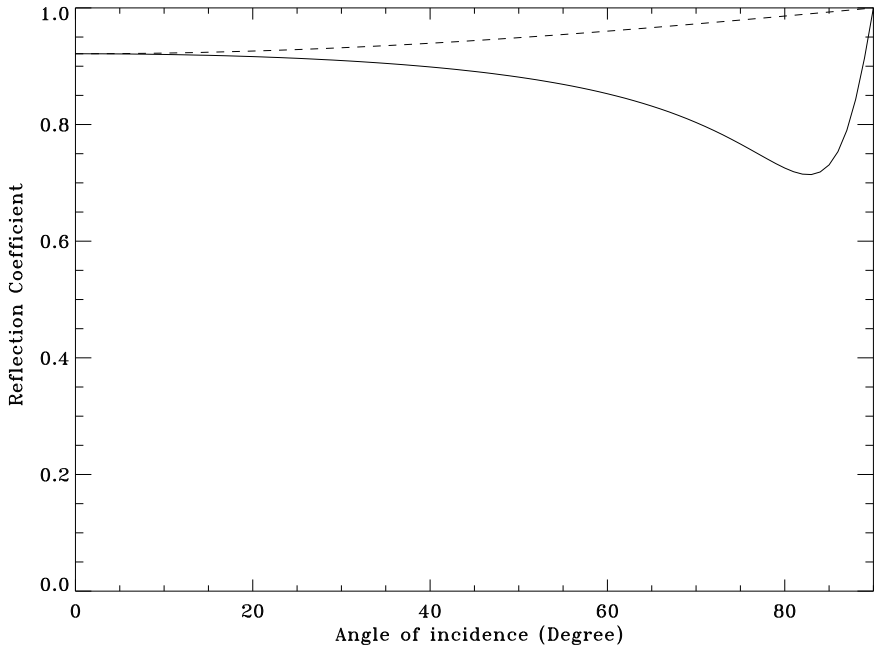

Figure 2.2: Variation of the modulus square of the complex amplitudes of reflection with angle of incidence for a metallic surface with a value of 1.3 for real and 7.8 for complex part of the refractive index. The parallel component to the plane of incidence $|R_{pa}|^2$ is represented by solid line whereas the perpendicular component $|R_{pe}|^2$ is represented by dashed line.

between the various Stokes parameters which characterise the input polarised light. The Mueller matrix for any optical system is usually determined by measuring the Stokes vector at the output for various input Stokes vectors (Gerrard and Burch, 1975). Atleast four linearly independent input Stokes vectors are needed to completely specify the 4×4 Mueller matrix. This requirement poses serious difficulties for large coelostats because of the requirement of large polarising optical components with uniform optical quality over the large area and also the need to characterise the system for all the possible angles of incidence involved in the solar observations. However, calculating the Mueller matrix of each mirror of the coelostat separately offer certain simplifications as explained below compared to the measurement of the

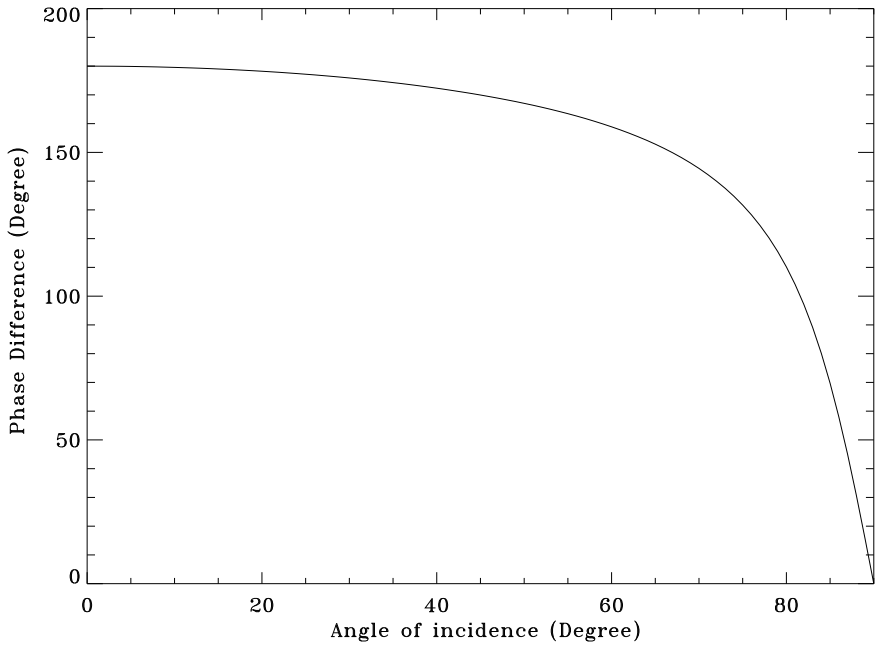

Figure 2.3: Variation of the phase difference between the two orthogonally polarised component with angle of incidence for a metallic surface with a value of 1.3 for real and 7.8 for complex part of the refractive index.

combined system. It is shown in the next section that the Mueller matrix of a single reflecting surface depends on two parameters, the refractive index of the mirror coating and the angle of incidence of the incident beam at the reflecting surface. Refractive index of the coating does not change with the angle of incidence. If the refractive index of the coating is measured independently, then the Mueller matrix of the reflecting surface can be calculated for any angle of incidence and hence avoids the need to measure the Mueller matrix for all angles of incidence. In this chapter, an optical method which was used to measure the refractive index of mirror coatings of the KTT is described. The results from the measurements are discussed.

2.3 Mueller matrix of a Reflecting Surface

The Mueller matrix of a single mirror is given by (Kawakami, 1983; Stenflo, 1994),

$$[M] = \tfrac{1}{2} \begin{pmatrix} 1+X^2 & 1-X^2 & 0 & 0 \\ 1-X^2 & 1+X^2 & 0 & 0 \\ 0 & 0 & 2X\cos(\tau) & 2X\sin(\tau) \\ 0 & 0 & -2X\sin(\tau) & 2X\cos(\tau) \end{pmatrix}.$$

X^2 is the ratio of the modulus square of the reflection coefficient of the two orthogonally polarised components (R_{pa} and R_{pe}) whereas τ is the phase difference between the two. i.e.,

$$X^2 = \frac{|R_{pa}|^2}{|R_{pe}|^2} \qquad \& \qquad \tau = \delta_{pa} - \delta_{pe}.$$

The values of X^2 and τ can be derived from the Fresnel formulae for reflection at a conducting layer as (Born and Wolf, 1984),

$$\tan(\tau) = \frac{2b\sin(i)\tan(i)}{\sin^2 i \tan^2 i - (a^2+b^2)}, \tag{2.1}$$

$$X^2 = \frac{a^2+b^2-2a\sin(i)\tan(i)+\sin^2 i\tan^2 i}{a^2+b^2+2a\sin(i)\tan(i)+\sin^2 i\tan^2 i}. \tag{2.2}$$

Where,

$$a^2 = \frac{1}{2}[\eta^2-\kappa^2-\sin^2 i + \sqrt{(\eta^2-\kappa^2-\sin^2 i)^2+4\eta^2\kappa^2}],$$
$$b^2 = \frac{1}{2}[-\eta^2+\kappa^2+\sin^2 i + \sqrt{(\eta^2-\kappa^2-\sin^2 i)^2+4\eta^2\kappa^2}].$$

It can be seen from the above formulae that the Mueller matrix of a single reflecting mirror is a function of the complex refractive index (η, κ) of the coating, where η is the real part and κ is the imaginary part of the refractive index. The Mueller matrix also depends on the angle of incidence, i. The refractive index is constant for different angles of incidence of the input beam. The angle of incidence for solar observation

can be obtained using spherical trigonometry and hence the problem reduces to the measurement of the constant refractive index of the optical coatings used. The theoretical instrumental polarisation for KTT has already been calculated using spherical trigonometry (Balasubramaniam, Venkatakrishnan and Bhattacharyya, 1985). It is used with some improvement and explained in Chapter 4 of this thesis. The refractive index of bulk aluminium coating was assumed in the earlier calculations of the instrumental polarisation at KTT (Balasubramaniam, Venkatakrishnan and Bhattacharyya, 1985). For a coating with thickness greater than (λ/κ), the 'skin depth', the layer can be treated as a bulk material (Makita and Nishi, 1970), where λ is the wavelength of observation and κ is the imaginary part of the complex refractive index of the coating. However, the refractive index measured by Capitani *et al.,* (1989) for their telescope coating showed a considerable difference from the bulk value. Hence, the assumption of bulk aluminium value for the coating will lead to a considerable error in the calculation of instrumental polarisation. To conclude, the refractive index of the optical coating has to be measured for proper modeling of the instrumental polarisation of an oblique reflecting telescope.

2.4 Ellipsometry of Coelostat Coating

Ellipsometry, which is the measurement of ellipticity of the polarisation state of light, can be used to measure the refractive index of any optical coatings (Azzam and Bashara, 1977; Riedling, 1987). The principle of the method is the determination of refractive index of the optical coatings from the measured values of X^2 and τ. By measuring the changes in the amplitudes and phases during reflection of the two orthogonally polarised component, one parallel to the plane of incidence and the other perpendicular to it, the values of X^2 and τ can be calculated. There are several different ellipsometric methods to measure the values of X^2 and τ (Heavens, 1991; Abeles, 1971; Hjortsberg, 1980; Hass, Heaney, and Hunter, 1982) for thick as well as

thin metallic films. The chief consideration for the measurement at KTT is the fact that the three mirrors of the coelostat system should remain in their respective cells during measurement, and also that the measurements are done without physically touching the mirrors to avoid damage to the surfaces.

One way to evaluate the optical constants η (the real part) and κ (the imaginary part) requires the measurement of the transmittance T at the normal incidence and the reflectance at near-normal incidence (Nilsson, 1968). This can only be applicable for transparent objects. For reflecting surfaces, η and κ are determined by measuring the reflection coefficient at two different angles of incidence and by using the graphical method as explained by Tousey (1939). However the accuracy achieved in the calculation of η and κ is of the order of 4% (Avery, 1952). The accuracy can be improved by measuring the X^2 as well as τ for several different angles of incidence of the input beam and by using a non-linear minimisation technique. An ellipsometer using a Babinet Compensator (BC) as the main optical element is developed to measure the value of X^2 and τ for different angles of incidence. A non-linear least squares method is used to derive the optical constants of the mirror coating from these measurements. Initially, a computer simulation was carried out in order to estimate the critical parameters necessary for the design of the ellipsometer. Based on the results from this simulation an ellipsometer was designed.

2.4.1 Computer Simulation

In the proposed method, an input unpolarised light beam is linearly polarised using a polaroid with its transmission axis kept at 45° to the plane of incidence. The polarised beam is then reflected from the mirror surface at an angle of incidence, i. The beam after reflection is intercepted by a BC. The BC consist of two wedges made from a birefringent material, usually quartz (refer to Figure 2.4). The optic axis of these two wedges are kept at 0° and 90° to the plane of incidence respectively. In Figure 2.4,

the plane of incidence is the plane of the paper and the optic axis of the two wedges are marked (optic axes lie along the x and y-axis). This configuration of the BC will introduce a systematic phase differences between the two orthogonal polarisation, one polarised parallel to the plane of incidence and the other perpendicular to it. At the center of the BC where the beam travels equal distance within the two quartz wedge, the phase difference introduced by the BC will be zero. The phase difference will increase linearly with increasing distance from the center in both directions along the x-axis. The output beam from the BC is analysed using a polaroid (P2) kept with its transmission axis crossed to the transmission axis of the input polaroid (not shown in Figure 2.4), *i.e.,* the transmission axis of the analyser is kept at 135° from the plane of incidence. The analysed beam will form a set of fringes at the detector plane which is at the output of the analyser. The fringes lie in the xy-plane with the intensity modulation along the x-axis since the phase difference changes only along the x-axis.

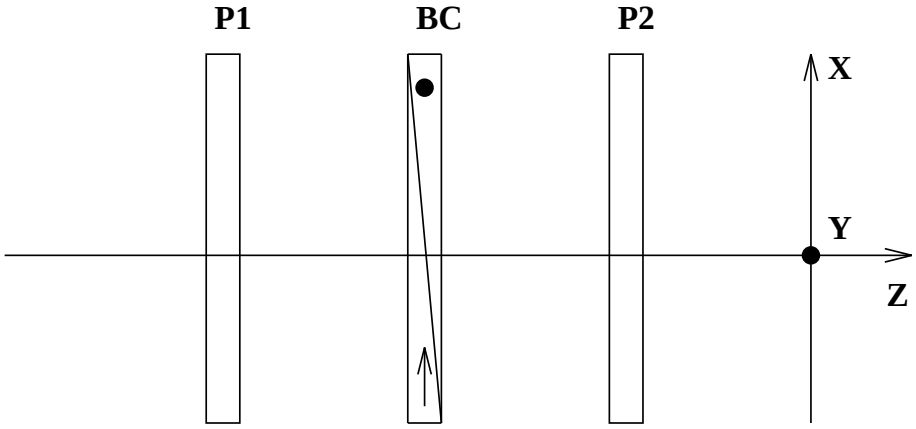

Figure 2.4: A schematic layout of the measurement of X^2 and τ using a Babinet Compensator (BC). The input beam is the reflected beam from a mirror surface (which is not shown in this figure) and it enters the system in the extreme left of the figure. P1 is the insertable reference polaroid and P2 is the analyser. P1 and P2 are kept crossed. The transmission axis of P1 is kept at an angle 45° to the plane of incidence.

Reference fringes are obtained by inserting a reference polaroid marked as P1

in Figure 2.4. The transmission axis of P1 is matched with the transmission axis of the input polaroid (*i.e.,* 45° to the plane of incidence). In this reference fringe, the minimum of the fringe intensity lies exactly on the center of the BC. When the reference polaroid is removed, the fringes are shifted along the x-direction depending on the phase difference introduced by the reflecting surface which in turn depends on the angle of incidence of the input beam with the reflecting surface. The values of τ can be obtained from this fringe shift measurement. Because of unequal reflection of the two polarisation components in and orthogonal to the plane of incidence at the mirror surface, the position angle of the resulting elliptical polarisation will rotate producing a decrease in the fringe contrast, to that of the reference fringe. The contrast can be maximised once again by rotating the polaroid (P2) around z-axis. If θ is the angle of rotation then the value of X^2 is given by (Born and Wolf, 1984),

$$X^2 = \tan(45 + \theta). \tag{2.3}$$

For the simulation, a particular value for the complex refractive index is assumed. The values of τ and X^2 are then obtained from equations 2.1 and 2.2 for different values of the angle of incidence. While generating the value of τ, the maximum error in the fringe shift measurement (which can be as low as 1μ for CCD detection of fringes using a BC with a wedge angle of 0.5°) is taken as the sensitivity of the system to the fringe shift measurement. Also, the systematic error in the measurement of angle of incidence is included. The data points are obtained by varying the angle of incidence by keeping the refractive index of the mirror coating fixed. While generating the experimental value of X^2, the systematic error of the fringe contrast measurement which is limited by the photometric accuracy of the detector is added. For a well exposed CCD frame with 8 bits of digitization, this turns out to be ≈ 0.4 %. Having generated such 'experimental' values τ_{exp} and X^2_{exp} for several angles of incidence, the following minimization functions are calculated, viz.,

$$\sigma_\tau^2 = \sum_i (\tau_{the} - \tau_{exp})^2 \tag{2.4}$$

$$\sigma_X^2 = \sum_i (X_{the}^2 - X_{exp}^2)^2 \tag{2.5}$$

where the summation is over the angle of incidence i and the theoretical values τ_{the} and X_{the}^2 are obtained by substituting arbitrary values of κ and η into equations 2.1 and 2.2. Thus, $\sigma_{\tau,X}^2$ are surfaces in κ, η space. The minimum of these surfaces yield the required value of κ and η. The σ_τ^2 function has a sharper minimum in the κ direction than in the η direction. It is for this reason that the determination of κ alone from the τ measurement is preferred. Then, use this value of κ in the X^2 measurement to determine η.

2.4.2 Results from the Simulation

The deviation of κ and η, determined using the minima of σ_τ^2 and σ_X^2, from the input values of κ and η can be considered as estimates of the errors of the method. The results of these simulation show that the errors of the κ determination chiefly depend on the errors in the measurement of the angle of incidence. In Figure 2.5, the κ errors are plotted as a function of the error in i, the angle of incidence. Each curve is for a specific wavelength as described in the figure caption. The conclusion is that the angle of incidence must be measurable with an accuracy better than 0.04° to obtain a κ determination to better than 1% accuracy. This is an important consideration while designing the ellipsometer. In Figure 2.6, the error in η determination is plotted as a function of error in κ measurement for different wavelengths assuming eight bit digitization of the intensity data. Figure 2.6 shows that for a 1% accuracy in κ determination, the accuracy in η will be better than 1% for all wavelengths.

The model used above is valid for a film whose thickness is larger than the skin depth. The skin depth increases with wavelength and hence the material will act as

a thin film at longer wavelengths. In those cases, the Fresnel formulae have to be modified. The modified formulae would depend on the number $'n'$ of layers one would like to model. So, from the two sets of measurements of τ and X^2, $3n$ parameters (η, κ and the film thickness of each layer) have to be determined (See, however, Bosch and Monzonis, 1995 for some recent attempts on ellipsometry of samples with arbitrary number of layers).

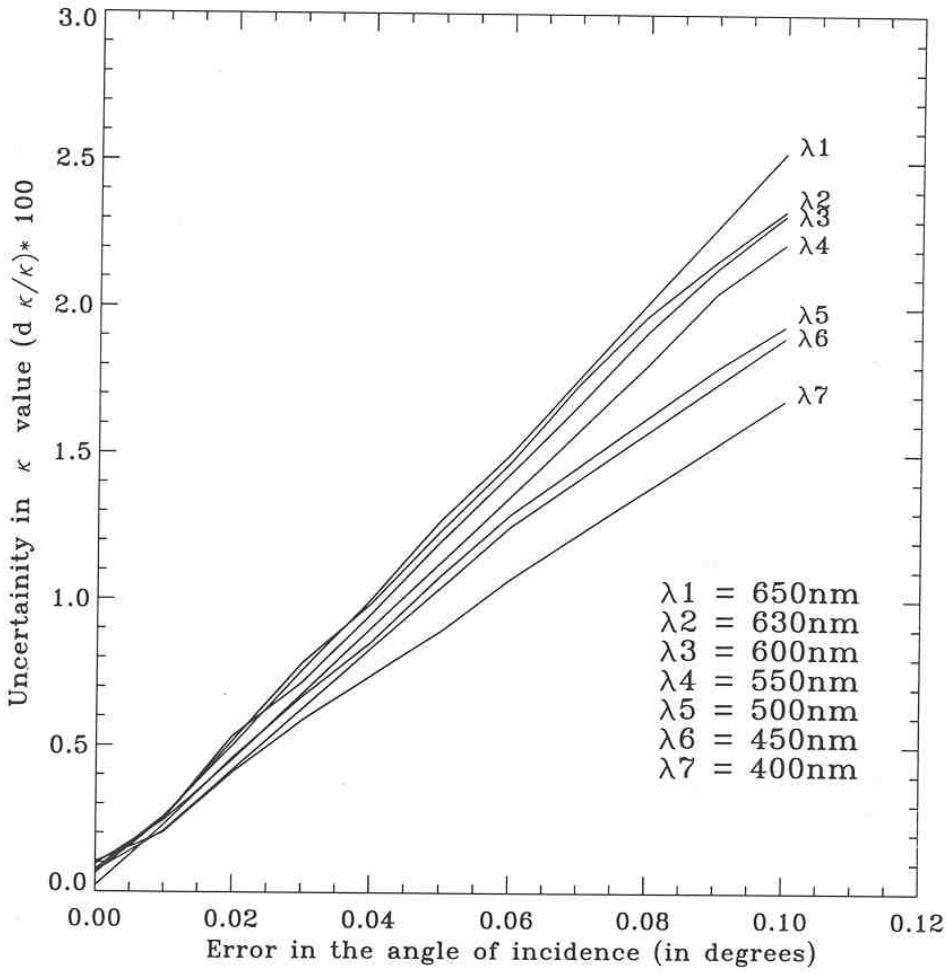

Figure 2.5: Variation of the percentage error in κ with the error in the angle of incidence measurement for different wavelengths mentioned in the figure

From the η and κ calculated using the bulk material approximation, the Mueller matrix [M] for a single reflecting mirror can be calculated. It can be seen that the

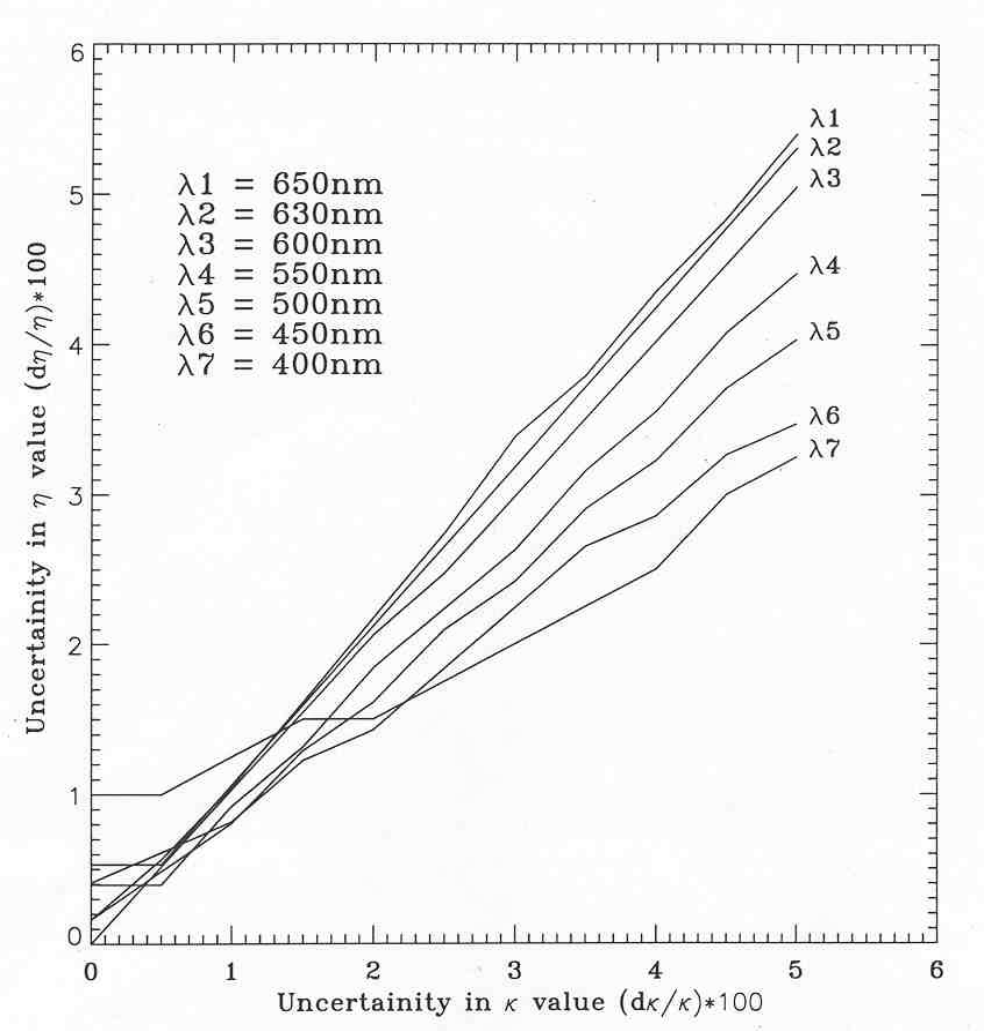

Figure 2.6: Variation of the percentage error in η with the percentage error in κ

errors in η and κ estimation would result in errors in [M] and finally errors in the magnetic field value derived from the observed Stokes' parameters. An error of 1% in η and κ can grow into an error of a few percent in the corresponding Mueller matrix for the Kodaikanal installation (Balasubramaniam, 1988). For example, a 10% crosstalk of V into Q or U would result in a spurious value of 10% for Q or U if V is 100%. If the error in compensation is a few percent, then this leaves a residual error of $\leq$ 1% in Q or U after applying the compensation. This limits the sensitivity of the transverse field measurements for weak fields ($\leq$100G) but poses no serious difficulty for moderate fields ($\geq$ 500G).

The technique suggested for measuring η and κ is also useful for monitoring the weathering of the coelostat mirrors and for determining the uniformity of the coatings over the mirror surface. One consequence of weathering would be the formation of an oxide layer on the aluminium coating. To simulate the oxide layer, the thickness as well as the refractive index of the layer should be known. In the case of solar telescopes, this cannot be known *a priori*. The thickness of the layer will depend on the time of exposure, humidity etc. Hence, it will be different for different observation sites and could also be a function of time. Modeling a reflecting surface as oxide free even in the presence of a thin oxide layer results in a drastic reduction of the equivalent η and κ values. However, the predicted X^2 and τ values using these pseudo values of η and κ compared well with the experimentally determined values (Burge and Bennett, 1964). For example, pseudo value of the refractive index η and κ calculated with the bulk material approximation will be a systematic function of the angle of incidence. The variation in these pseudo values turns out to be less than 3% for aluminium for angle of incidence greater than 20° (Burge and Bennett, 1964). Hence, the bulk material approximation is valid to within an error of 3% for large angles of incidence. However, for small angles of incidence the errors can be large. The variation of X^2 and τ has to be measured experimentally and a model with the oxide layer has to be fitted with the experimental data in order to achieve greater accuracy.

In conclusion, this study serves to highlight the areas in the experimental set up where special care must be maintained. We conclude that the τ measurement is ideal for estimating κ, but the chief source of error is in the measurement of angle of incidence. The X^2 measurement is ideal for estimating η and is limited only by the accuracy of the intensity measurement.

2.4.3 Measurement of the Refractive Indices

An ellipsometer is designed using a BC based on the above inputs. The optical layout of the ellipsometer is given in Figure 2.7. The instrument consists of two parts, a source and a detector part. The source part consists of a He-Ne laser, folding optics and a wedge to get the required angle of incidence (left side part of the Figure 2.7). The He-Ne laser is chosen because the wavelength of this source (6328 Å) is very close to the wavelength of interest for the solar observation, which is 6302 Å. The beam from the He-Ne laser is folded by a 45° prism. The folded beam is then split into two by a glass plate. The reflected beam from the glass plate is used as a reference beam and the transmitted beam is bent by a wedge of angle about 9.9°. The wedge angle determines the angle of incidence on the mirror. A polaroid sheet with its transmission axis at 45° to the base plane of the prism is pasted in the front side of the wedge. This polarises the input beam with the plane of polarisation at 45° to the plane of incidence. The wedge can be rotated through an axis perpendicular to the beam direction and hence the angle of incidence on the mirror can be varied by this rotation. However, the rotation makes the beam to move on the mirror thereby preventing the measurement at a single point for different angles of incidence. To compensate for this motion, the source unit is moved using a translation stage. For this, the reference beam is used to fix the measurement point.

A horizontal and a vertical scale, fixed with the source part, measures respectively the position of the reference beam on the mirror from the wedge surface. The tangent of the ratio of vertical to the horizontal scale reading gives the angle of incidence on the mirror surface when subtracted from 90°.

The detector part consists of an insertable polaroid, a BC and a rotatable polaroid (see the inset of Figure 2.7). The insertable polaroid is used to take the reference fringe and the fringe shift measured for different angles of incidence can be related to the phase difference τ. The rotatable polaroid is used to maximise the contrast of the fringe. The rotation angle of this polaroid needed to maximise the contrast is

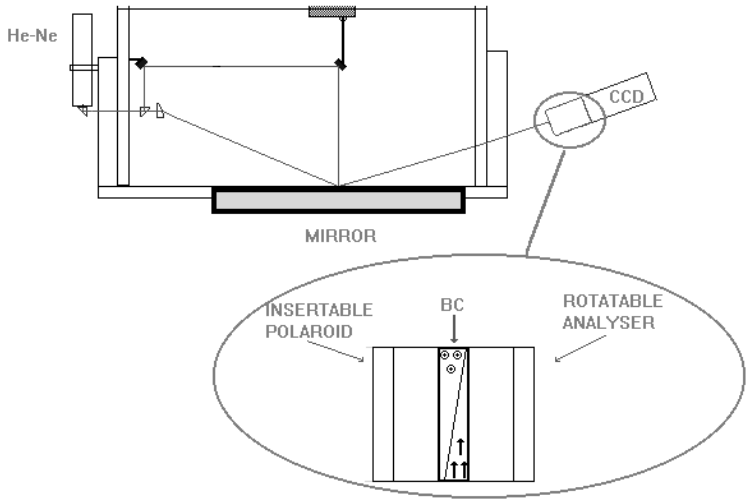

Figure 2.7: Optical layout of the ellipsometer

related to X^2.

The parameters of the instrument are,

- Range of angles of incidence: $\approx 5°$
- Measurement accuracy in angle of incidence: $\pm 0.15°$
- Rotation Accuracy of the Analyser: $\pm 0.02°$
- 8-bit digitisation level for the CCD-camera
- Wedge angle of the BC: $5°$

2.4.4 Results from the Measurement

The ellipsometer described above was used to measure the X^2 and τ values for different angles of incidence on the three mirrors of the KTT. Figure 2.8 shows the variation of the measured τ and X^2 for different angles of incidence for the first mirror. The solid line shows the variation of the same parameter for the bulk aluminium model. The inconsistency of these measured and theoretical values clearly shows the failure of

the bulk aluminium values. The measured data can be fitted by varying the complex refractive index of the bulk aluminium in the model. However, it has been shown that, a thin oxide layer formed on the aluminium coating can drastically change the computed pseudo-index of refraction (as named by Burge and Bennett, 1964) if the oxide layer is neglected in the model. The calculated pseudo-index of refraction will always be lower than the bulk aluminium value if the model does not include the oxide layer.

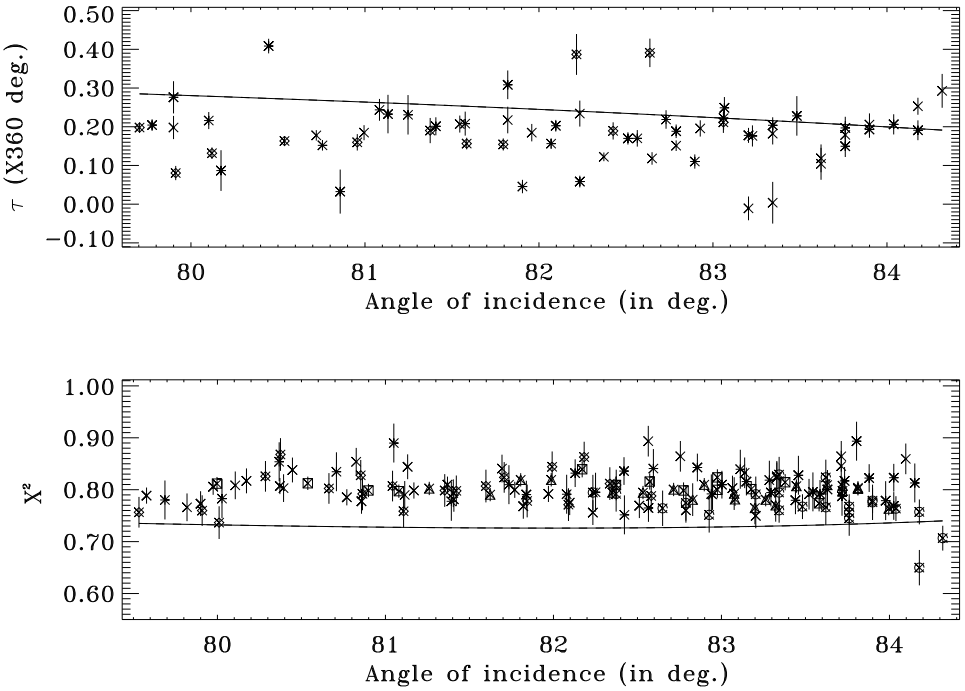

Figure 2.8: Variation of the measured τ and X^2 with angles of incidence, for the first mirror of the KTT, are shown as data points. The different symbols represent the data taken at different regions on the mirror. The solid line is the bulk aluminium model.

For our analysis of the measured data we assumed a model of a plane, semi-infinite substrate covered by a thin non-absorbing oxide layer. The optical constants are assumed to have the same value throughout the oxide film or aluminium substrate. The Mueller matrix given above still holds good for this new model. The inclusion of

the oxide layer changes the reflection coefficient and the phase difference and hence the value of X^2 and τ. The reflection coefficient of a single oxide layer on an aluminium surface is given by (Heavens, 1991),

$$R = \frac{r_1 + r_2 exp(-2j\delta)}{1 + r_1 r_2 exp(-2j\delta)}$$

where, $\delta = \frac{2\pi}{\lambda}$h cos$(i)$, h is the thickness of the oxide layer, r_1 and r_2 are the Fresnel reflection coefficients for the oxide and the aluminium surfaces, respectively. The Fresnel reflection coefficient for the parallel and perpendicular components are given by,

$$r_{pa} = \frac{\sin(i_1 - i)}{\sin(i_1 + i)} \qquad \& \qquad r_{pe} = \frac{\tan(i_1 - i)}{\tan(i_1 + i)}$$

where i and i_1 are the angle of incidence and angle of refraction at the corresponding surface, respectively. The value of i is the angle of incidence measured from the ratio of the vertical to the horizontal scale reading and i_1 is calculated using Snell's law. A value of 1.77 is assumed for the refractive index of the oxide layer (Lide, 1995).

Initially, a least square fit is done for the τ measurement by varying the value of κ. The value of η is fixed to be 1.30, the bulk aluminium value (Lide, 1995). The thickness of the oxide layer was taken to be zero. The value of κ at which the least squares minimisation gave the best fit was taken as the initial guess value. Similarly, the X^2 measurements are minimised by varying the value of η and fixing κ to 7.5, the bulk aluminium value. A numerical simulation of the model was done for different values of the oxide layer thickness, the complex refractive index of the aluminium η and κ around the initial guess value. These simulated values were fitted with the data points in the least square sense and the best fit parameters are determined. The results for the fitted parameters of the three mirrors are shown in Table 2.1. The value obtained for the bulk aluminium from these least squares method shows a considerable difference from the bulk aluminium value quoted in the literature. However, values of $\eta = 1.13$ and $\kappa = 6.36$ were obtained for bulk aluminium (Heavens, 1991) since the actual value of η and κ depends on the purity of the aluminium.

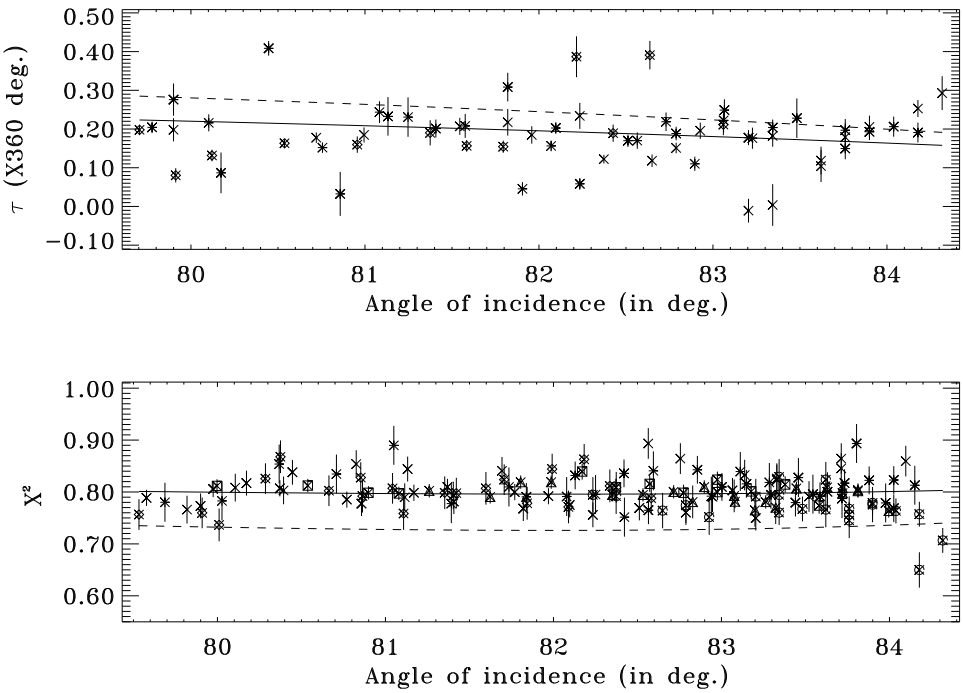

Figure 2.9: Same as Figure 2.8 except that the solid line is the model fit after including the oxide layer and the dashed line is for bulk aluminium model

Figure 2.9 shows the variation of the τ and X^2 for different angles of incidence and it can be seen that the fit of the data points with the model that includes the oxide layer is better than the model without the oxide layer. Figure 2.10 and Figure 2.11 show the same for the second and the third mirrors, respectively.

We conclude that the complex refractive index measurement of the optical coating of the oblique reflecting telescope is necessary in order to model the instrumental polarisation accurately. The inclusion of the oxide layer into the model is needed to get the correct complex refractive index value as well as the correct model for the instrumental polarisation. Ignoring the oxide layer in the model can produce a large error in the instrumental polarisation calculation.

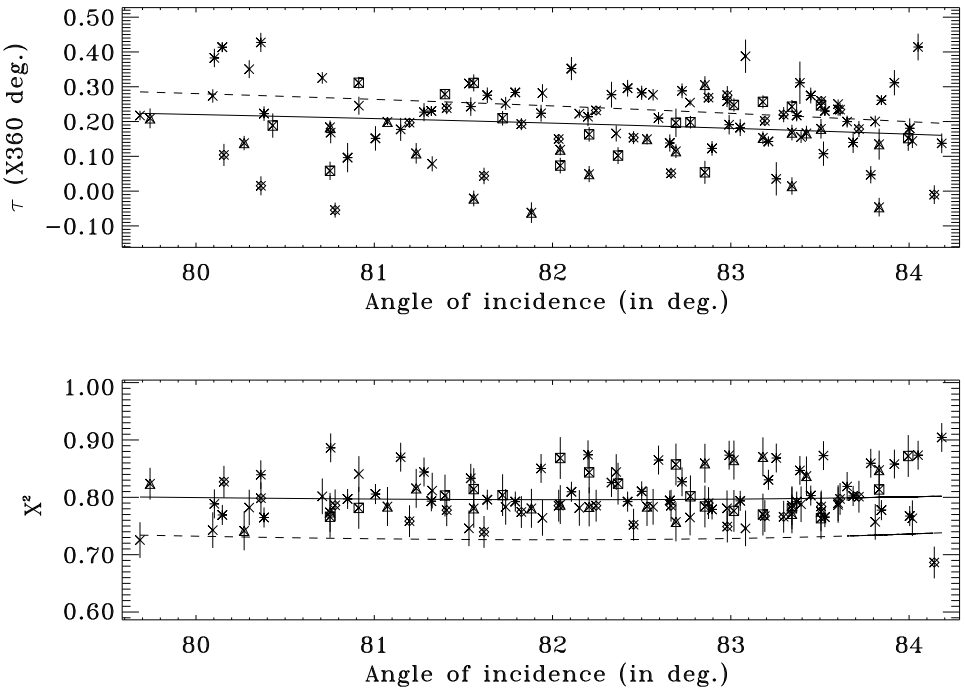

Figure 2.10: Same as Figure 2.9 except that the data are taken for the second mirror of the KTT.

2.5 Conclusions

The measurement of the change of polarisation by reflection of solar optical telescope is needed in order to measure the magnetic fields of high resolution magnetic structure in the sun (Lites, 1987; Lites, 1997; Lites, Scharmer, and Skumanich, 1990; November, 1991). Hence, the accurate measurement of the complex refractive indices of the reflecting mirrors, used in the solar telescope, is necessary. One of the optical method named as ellipsometry using a Babinet compensator was described and demonstrated with the actual measurement. The parameters for which care should be taken while designing the instrument was discussed using a computer simulation. The conclusions from the simulation are,

- The κ should be calculated using the measurement of τ.

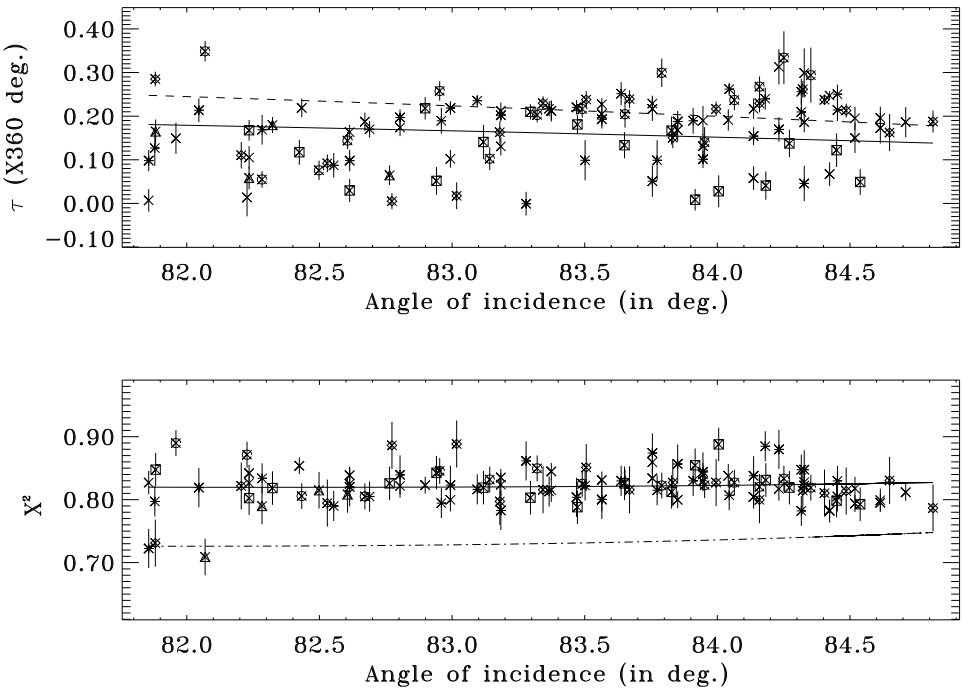

Figure 2.11: Same as Figure 2.9 except that the data are taken for the third mirror of the KTT.

- The η should be determined with X^2 measurements.
- The angle of incidence measurement should be accurate to 0.1°.
- Region of angle of incidence to measure X^2 and τ is 70° to 90° in order to take advantage of the large variation of X^2 and τ in this region which makes the determination of η and κ more accurate.
- Minimum of 8-bit digitisation levels are needed.
- Minimum wedge angle of BC is about 5°.

An ellipsometer is designed with all these input and the measurements of X^2 and τ were carried out at different regions on the three mirror surfaces. It was found that the model with bulk aluminium value does not fit the measurement well. The inclusion of the oxide layer in the model demonstrates the better accuracy achieved in

Table 2.1: The best-fit parameters for the three mirrors

Mirror	η	κ	h
I	1.13±0.02	6.89±0.04	$\frac{\lambda}{14}$
II	1.13±0.02	6.89±0.03	$\frac{\lambda}{11}$
III	1.13±0.01	6.89±0.04	$\frac{\lambda}{12}$

the calculation of the instrumental polarisation. The refractive indices of the mirror coatings and the thickness of the oxide layer of the three mirrors of the coelostat at KTT was measured.

Chapter 3

Stokes Polarimeter at the KTT

3.1 Summary

The Stokes polarimeter developed for the KTT is explained in this chapter. Two optical methods were used to test different components of the polarimeter individually. The whole polarimeter was tested in the laboratory and in the field. The details of the experimental setup and the theory needed to extract the misalignments of the optical components are explained. An interferometric method was used to find out the retardance of the quarter-wave plate.

3.2 Introduction

A Stokes polarimeter measures the polarisation state of an input beam by measuring the Stokes parameters which is represented as a column vector $[I, Q, U, V]^T$, where the superscript 'T' represents the transpose operation. A generalised polarimeter is shown in Figure 3.1.

Consider a beam of partially polarised light, $[I, Q, U, V]^T$, which passes through

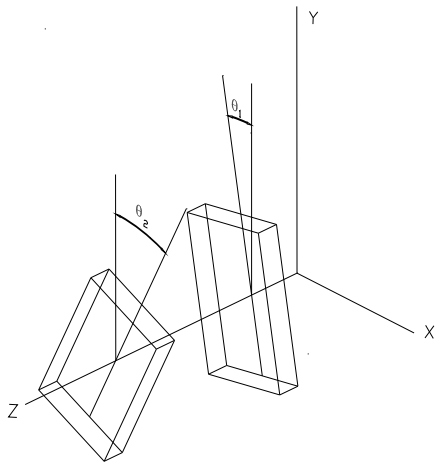

Figure 3.1: Block diagram of a generalised polarimetric arrangement

a retarder of retardance 'Δ' with its optic axis kept at an angle 'θ_1' with respect to a reference axis. In Figure 3.1, y-axis is taken as the reference axis. The angle is measured positive in the clock wise direction when the observer is looking at the source. The beam of light then passes through a polariser with its transmission axis kept at an angle 'θ_2' from the y-axis. Then the output emerging light from the polariser is represented by,

$$[Ip, Qp, Up, Vp]^T = [M2][M1][I, Q, U, V]^T \tag{3.1}$$

where $[Ip, Qp, Up, Vp]^T$ is the output Stokes vector and [M1] & [M2] are the 4×4 Mueller matrices for the retarder and the polariser respectively. The Mueller matrices [M1] and [M2] are defined as,

$$[M1] = \begin{pmatrix} 1 & 0 & 0 & 0 \\ 0 & c_{21}^2 + s_{21}^2.\beta & c_{21}.s_{21}.(1-\beta) & -s_{21}.\mu \\ 0 & c_{21}.s_{21}.(1-\beta) & s_{21}^2 + c_{21}^2.\beta & c_{21}.\mu \\ 0 & s_{21}.\mu & -c_{21}.\mu & \beta \end{pmatrix}$$

where,

$$c_{21} = \cos(2\theta_1) \quad \& \quad s_{21} = \sin(2\theta_1)$$

$$\beta \;=\; \cos(\Delta) \qquad \& \qquad \mu = \sin(\Delta)$$

and

$$[M2] = \tfrac{1}{2} \begin{pmatrix} 1 & c_{22} & s_{22} & 0 \\ c_{22} & c_{22}^2 & c_{22}.s_{22} & 0 \\ s_{22} & c_{22}.s_{22} & s_{22}^2 & 0 \\ 0 & 0 & 0 & 0 \end{pmatrix}$$

where,

$$c_{22} = \cos(2\theta_2) \qquad \& \qquad s_{22} = \sin(2\theta_2)$$

Note that the [M1] and [M2] defined above is general. The Mueller matrix [M1] is applicable to any ideal retarder with retardance Δ, with its optic axis kept at an angle θ_1 from the reference axis. The Mueller matrix [M2] is applicable to any polariser with its transmission axis kept at an angle θ_2 from the reference axis. However, [M1] and [M2] does not include the depolarisation effects and other defects which are possible during the manufacturing process.

By substituting [M1] and [M2] in the Equation 3.1, the output intensity in terms of the input Stokes parameters for the system shown in Figure 3.1 can be calculated and is given by,

$$\begin{aligned} Ip = \frac{1}{2}\{I + Q.[c_{22}.(c_{21}^2 + s_{21}^2.\beta) + s_{22}.c_{21}.s_{21}.(1-\beta)] \\ +U.[c_{22}.c_{21}.s_{21}.(1-\beta) + s_{22}.(s_{21}^2 + c_{21}^2.\beta)] \\ +V.[-c_{22}.s_{21}.\mu + s_{22}.c_{21}.\mu]\} \end{aligned} \tag{3.2}$$

Equation 3.2 shows that there are several ways of combining different optical components to calculate all the four Stokes parameters by measuring the output intensity, I_p (Shurcliff, 1962; Clarke and Grainger, 1971; Stenflo, 1984). Table 3.1 lists the different combinations of the retardance Δ, the angle θ_1 & θ_2 and the associated quantity measured.

Table 3.1: Broad classification of polarimetric methods

Sr. No.	Method	Conditions on the variable	Quantity Measurable
1.	Polariser at different orientation + No retarder	θ_2 variable, θ_1 constant and zero, Δ constant and zero	I, Q and U
2.	Retarder at a fixed orientation and fixed retardance + Polariser at different orientation	θ_2 variable, θ_1 constant, Δ constant	I, Q, U and V
3.	Retarder at different orientation and fixed retardance + Polariser at fixed orientation	θ_2 constant, θ_1 variable, Δ constant	I, Q, U and V
4.	Retarder + Polariser combination at different orientation with their relative orientation fixed and fixed retardance	θ_2 variable, θ_1 variable, $(\theta_2 - \theta_1)$ constant, Δ constant	I, Q, U and V
5.	Variable retarder with fixed orientation + Polariser at fixed orientation	θ_2 constant, θ_1 constant and Δ variable	I, Q, U and V

Each method, listed in Table 3.1, has its own advantages and disadvantages (Clarke and Grainger, 1971). The polarimeter which is developed at the KTT is a rotating prism polaroid with an insertable quarter waveplate (QWP) and hence is the combination of method 1 and 2. The linear polarisation (Q and U) is measured without any retarder (hence method 1) and the circular polarisation is measured by inserting a fixed retarder (quarter wave retarder) at a fixed orientation (hence method 2). The chief consideration for using a rotating prism polaroid rather than a rotating half waveplate (HWP) is that the cross-talk between the Stokes param-

eters arising from the retardance error in the waveplate can be avoided completely. Otherwise, the error in the retardance produces a cross-talk from V (circular) into Q and U (linear) component and *vice versa*. This can be severe in the case of sunspot measurement where the amount of V is large compared to Q and U, at the umbral region of the sunspot.

For example, if δ is the error in the retardance of a HWP, then the error in the measurement of U can be calculated as,

$$\frac{\delta U}{U} = \frac{1}{2}.(\cos\delta - 1) - \frac{V}{2U}.\sin\delta.$$

For very small errors in the retardance, the first term in the above equation can be neglected and hence the residual error in U, *i.e.,* δU is $\frac{V}{2}\delta$. An error of 0.1° in the retardance (i.e., $\delta = 0.1°$) and for a value of 20% in V and 1% in U (typical observational value at the umbra of a sunspot which is very close to the disk center), the error in U (i.e., δU) is about 0.017%. Similarly, the residual error in Q can be calculated as, $\delta Q = \frac{V}{\sqrt{2}}\delta$ and hence an error of about 0.024% for the same observational parameter.

In this chapter, the design of a polarimeter for modulating the input polarised signal and the demodulation scheme using a CCD chip is discussed. Also, the testing of the polarimeter, both in the laboratory and with the KTT is described.

3.3 Polarimeter and the Spectrograph

The Stokes polarimeter designed for the KTT is used in the converging beam of the telescope since the f-ratio of the telescope is high (f-90). The polarimeter consists of a manually insertable QWP, a rotating Glan-Thompson prism polaroid (GTP) as analyser and an insertable polaroid (called as compensating polaroid) for the Stokes U-measurement (Figure 3.2).

An IR sensor with the associated electronics is used to sense the reference position

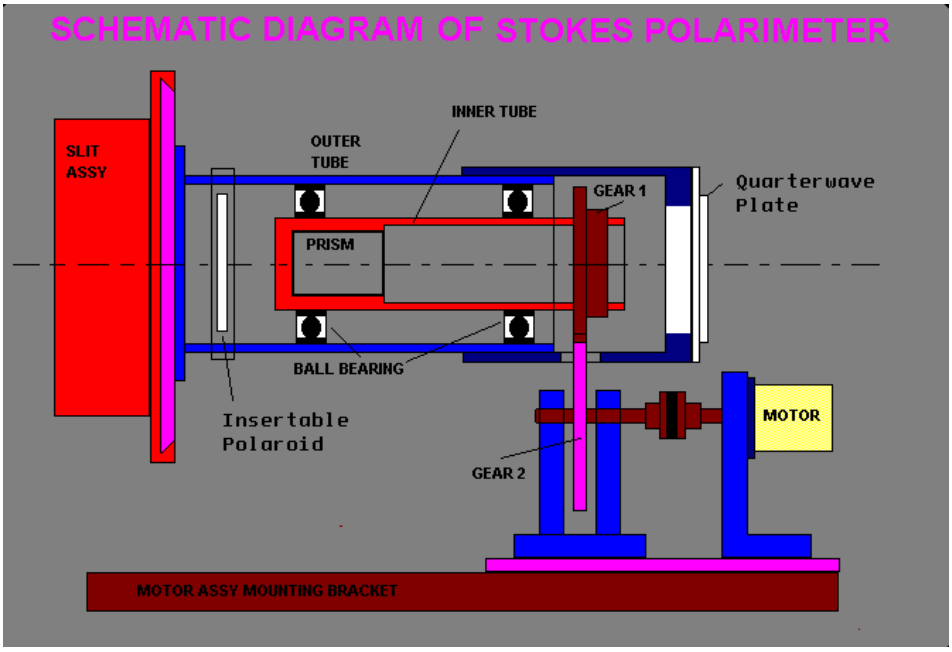

Figure 3.2: Block diagram of the Stokes polarimeter

which is set at 45° from the slit direction in this case. The transmission axis of the GTP is matched with the sensor position. The compensating polaroid for the Stokes U-measurement is used to compensate the spurious polarisation produced because of the differential grating response to the two orthogonal polarisation, one along the grating groove direction and the other perpendicular to it. The details of the grating response to different input polarisation state and the function of the compensating polaroid will be discussed later in this chapter (refer section 3.5). The whole polarimeter slides on to the slit of the spectrograph in order to minimise vignetting since the polarimeter is used in the converging beam of the telescope. The image plane of the telescope coincides with the slit of the spectrograph. The objective of the telescope can be moved to adjust the focal plane. Since the focal ratio of the objective is f-90, it has a very large depth of focus. Any minor defocusing due to the polarimetric optics can be readjusted by repositioning the imaging objective of the telescope. The acceptance angle constraint posed by the polariser and the QWP is well within the focal ratio of the telescope.

3.3.1 Spectrograph

The spectrograph is a Littrow mount spectrograph whose entrance slit is located at the image plane of the KTT. The spectrograph is housed in a long cylindrical tube running along the length of the tunnel in order to reduce the scattered light from the surrounding. The light from the slit of the spectrograph falls on a 18.3 m focal length, two-element Hilger achromat, in conjunction with a 600 lines/mm Babcock grating, ruled over an area of 200×135 mm and blazed in the fifth order at $\lambda\lambda$5000Å. The theoretical resolving power of the spectrograph is 600,000. The advantage of the Littrow mount spectrograph is that the Hilger achromat itself acts as a camera lens to image the spectrum on to a CCD which is kept below the slit. A one-to-one correspondence exists between every point along the length of the slit and the length of the spectrum in a direction perpendicular to the dispersion direction.

3.4 Detector

The data discussed in this thesis are obtained with two types of charge-coupled device (CCD). The first detector is an EEV P8603 CCD [1]. Let us call this as Det-1. The other CCD is a Photometrics CCD [2]. Let us call this as Det-2.

3.4.1 Detector-1 (Det-1)

Det-1 is an analogue integrated circuit with 576×385 picture elements (pixels) that are light sensitive. It is cooled to temperatures of between 120K to 180K to reduce the thermal dark current generated within the device. At the end of an exposure the

[1] CCD 2000 Imaging system reference manual, 19000-M-02 Issue 4, 16 November 1984, Cambridge Electronic imaging, 53, Hamilton Road, Cambridge CB4 1BP, Telephone (0223)-63737

[2] Photometrics Reference Manual, 1993, Photometrics Ltd., 3440 East Britannia Drive, Tucson, Arizona 85706, (602) 889-9933

device is read out one pixel at a time under the control of the host computer that has to generate signals to cause the device to transfer charge in the two directions and to return the data value to the computer. This CCD is mounted in a liquid nitrogen cooled dewar and connected to the CCD 2000 driver electronics rack by a single flat cable. As a minimum the system must include bias, clock modules, the double-correlated sampling (DCS) module. The modules communicate with a tri-state bus on the driver electronics rack to enable the system to be operated at a distance from the host computer. A bidirectional very high speed (8 Megabaud) serial data link is used that reduces the interface to a single co-axial cable, transformer isolated at each end. There is an optional facility to measure various analogue and power supply levels both with a built in digital voltmeter and remotely under computer control with the analogue to digital converter on the DCS module. This allows both local and remote checking very rapidly of the system set-up parameters. Provision is also made for measuring and (optionally) controlling the operating temperature of the CCD within the dewar.

The CCD 2000 imaging system consist of three major assemblies. These are,

1. The computer interface unit which transmits control data to and receives data from the CCD driver electronics rack.

2. **The CCD driver electronics rack:** This generates the necessary DC supplies (bias module) and clock waveforms (clocks module) to drive the CCD in the dewar. The output signal is processed in the double correlated sampling module where the detected signal is digitised for return to the host computer. A transmitter/receiver module handles communications with the computer and a multiplexer module decodes the received control words and routes them to the appropriate module. In order to facilitate system checkout and alignment a run/display module is included which will drive the CCD camera without a host computer and generate three analogue signals that may be used to give an intensity modulated XY display on a suitable monitor oscilloscope. The temperature of the CCD and of the electronics rack may be sensed

by the monitor/thermal module which can also control the temperature of the CCD mount with the dewar. This module also permits remote monitoring of most of the critical potentials in the system electronics rack by the host computer.

3. **Dewar with CCD:** Det-1 is mounted inside a dewar cooled with liquid nitrogen.

The sensor array is divided into three regions using an aluminium mask of 1 mm thickness, 12.7 mm length and 8.3 mm breadth. It is held on to the surface of the CCD mount. This mask allows the central (197 pixels; 4.3 mm) region to be exposed to light and the upper and lower regions shielded from the light beam (Refer to Figure 3.3). This demodulation scheme is very similar to the one used by Stockman (1982). The sensor is kept in a liquid nitrogen cooled dewar. The controller is from Astromed, UK. The controller has the necessary clock generation, bias voltages, signal processing, data conversion and data transmission electronics built into it. It operates in slow scan mode with double correlated sampling (DCS) with full 15-bit data conversion. A serial cable link connect the parallel port of the PC to the controller through an external parallel to serial converter. A three meter cable connects the dewar to the controller.

The software has been developed under Linux (a UNIX variant) environment. The application program comprises Graphical User Interface (GUI), image display, a driver software for image data acquisition based on X-windows system and polaroid movements. The software features include simple diagnostic routines for testing the CCD controller and electronics, file handling routines to store and restore image files in 'Flexible Image Transfer Software (FITS)' format, image data acquisition routines for acquiring bias, dark or object and simple quick look functions for image data analysis. The hardware and software part of this detector is developed by our engineers Mr. G. Srinivasulu and Mr. A. V. Ananth.

3.4.2 Detector-2 (Det-2)

Det-2 is a Photometrics AT200 CCD camera system. It includes three hardware components, (i) An AT200 camera controller, (ii) A CE200A camera electronics unit and (iii) A liquid cooled CH250 camera head. A liquid circulation unit is used for the cooling of the camera head. These components are linked by custom cables and controlled by a host computer.

AT200 camera controller: The AT200 camera controller manages communications between a host computer and a CE200A camera electronics unit. A digital signal processor sends control signals to the CE200A via the camera controller cable. CCD data are received through the same cable. The AT200 has no memory of its own, so incoming data must be promptly stored in host RAM. Once collected into host memory, the data can be manipulated by software on the host computer. The AT200 can be synchronised to external equipment or to a manual trigger with the User I/O connector. This feature is used to control the Stokes polarimeter, like sensing the reference position and rotating the stepper motor.

CE200A camera electronics unit: The CE200A camera electronics unit contains signal processing, camera control, and temperature control systems. It produces CCD clocking signals for the CCD camera head and manages the transfer of raw CCD data to the AT200.

CCD camera heads: Photometrics CCD camera head is cooled to reduce dark current, the spontaneous charge generated by heat and other non-photon sources. Cooling is achieved by thermoelectric (peltier) cooling. The camera head is composed of a sealed CCD enclosure, a shutter assembly. The head contains electronics that are directly associated with CCD operation. The camera head cable transmits voltages and signals to and from the CE200A. A preamplifier raises the CCD output signal to a high level for digitisation.

3.5 Function of the Polarimeter

The function of the polarimeter with Det-1 is as follows, the GTP is brought to the reference position. The Stokes Q measurement corresponds to this position. Spectra from this polarisation state, I+Q is made to fall on the window of the CCD sensor (Det-1) and integrated for 100 msec and then the shutter is closed. Subsequently the GTP is moved to the orthogonal position, I-Q in 60 msec. During this period the exposed region is moved to one of the unexposed region *i.e.,* the masked region. In this position, shutter is opened again and charge integration for 100 msec is performed. After the charge integration, the shutter is closed and this completes one full charge shifting operation. After completing one full operation, the GTP is moved again to the orthogonal position, I+Q and while the charges are shifted in the opposite direction so that the previously exposed charges corresponding to I+Q will now be in the window. The shutter is opened at this position for next 100 msec exposure and the new charges will get added with the old one. The back and forth movement of the charges in the imaging area is achieved by forward/reverse parallel shift in the CCD sensor. These operations, depicted in Figure 3.3, continue until the necessary signal to noise ratio is achieved. The number of full charge shifting operations is nothing but the ratio of the total integration time in msec to 100 msec which is the exposure time for a single spectra in one polarisation state. The number of full charge shifting operations has to be integer multiple in order to get equal total exposure time for both the orthogonal polarisation (I$\pm$Q).

Once, the I$\pm$Q measurement is over, the GTP is rotated to an angle of 45° from the reference position. The compensating polaroid with its transmission axis at 45° from the slit direction is now inserted at the back (before the slit) of the GTP. Now, the polarimeter is ready for the measurement of I$\pm$U. Similar charge shifting operations were carried out as was done for I$\pm$Q. However, longer exposure times (i.e., more number of charge shifting operations) are needed because of the light loss due to the

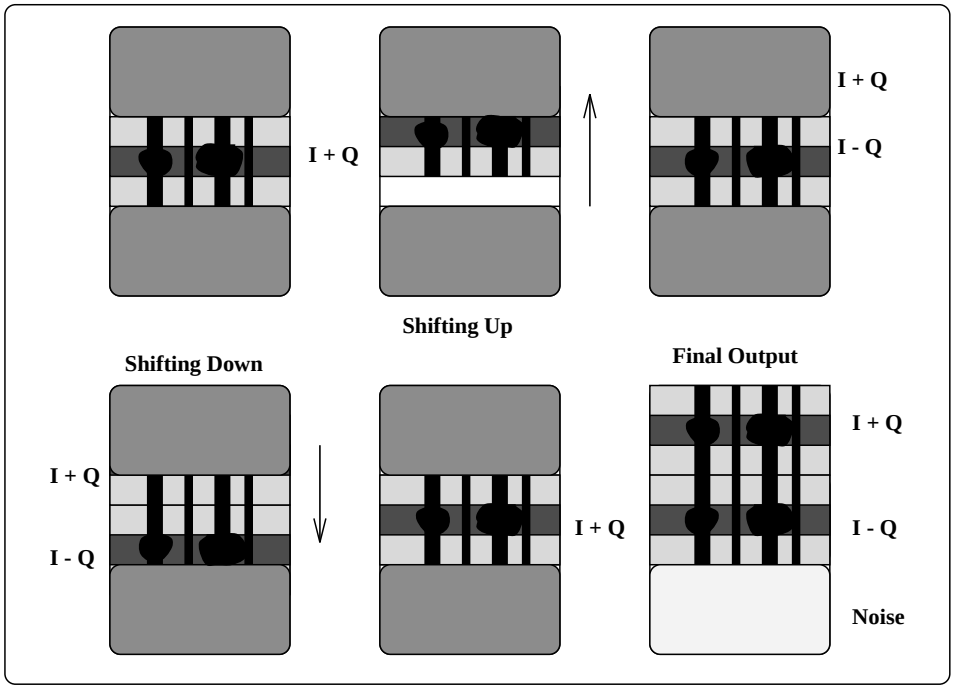

Figure 3.3: Charge Integration inside CCD

extra polaroid inserted. In practice, the same signal to noise ratio was never achieved. The signal to noise ratio in I±U measurement is lower by a factor of two to that of the I±Q measurement. For the circular polarisation measurement (V), a QWP with its optics axis at 90° to the slit direction is manually inserted in front of the GTP and the compensating polaroid inserted at the back of the GTP for U measurement is removed. Charge shifting is done with the GTP position similar to that of the I±Q measurement.

The operation of the polarimeter with Det-2 is very similar to the one described above except that there is no charge shifting within this CCD. The two orthogonal polarisation states (say, I±Q) are exposed independently and stored in the buffer. However, in order to save the writing time to the computer, a three dimensional data cube is created in the buffer to store all the six measurements (I±Q, I±U and I±V). At first the polarimeter senses the reference position using the IR-sensor and the GTP is positioned for the I + Q measurement. The spectra corresponding to I + Q is exposed. The exposure time used for our observations varies from 100 msec to

500 msec depending on the sky transparency to achieve a good signal to noise ratio. The spectra exposed is transfered to the buffer and the polarimeter rotates to position the GTP in the orthogonal polarisation position for the I - Q measurement. Instead of coming back to the reference position again for the U-measurement, the polarimeter is rotated in the same direction for 45° and then 90° more to obtain the I±U spectra. The compensating polaroid is inserted behind (in front of the slit) the GTP before the U-exposure takes place. The I±V measurement is carried out by rotating the polarimeter to 45° and then 90° more from the end position of U-measurement. The compensating polaroid is removed and a QWP is inserted in front of the GTP for the V-measurement. All these six images were stored in the buffer. At the end of the V-measurement, this three dimensional data cube is saved into the computer memory in 'FITS' format. The control software is written using the macros available with the Photometrics software. This includes the sensing of the initial position using the IR sensor, movement of the stepper motor to rotate the GTP and controlling the mechanical shutter in front of the CCD to expose the spectra at the correct moment. With the availability of a pentium processor, these measurements are done quickly. All the six measurements for a slit position is done within about 1 minute. This way of measurement will introduce spurious polarisation signal if the sky condition is not good. However, this CCD has the advantage that it is larger in size and hence a larger field of view can be obtained with few more Zeeman sensitive spectral lines in the spectral direction apart from the lines Fe I 6301.5Å and Fe I 6302.5Å.

The polarimeter was tested in the laboratory and in the field with the KTT before the data for the sunspots were obtained. The retardance error in the QWP is tested using a polarisation interferometric technique. Also, the positional alignment error of the QWP, the GTP and the compensating polaroid is tested in the laboratory. Appendix A summarises the algorithm used to find out the Mueller matrix of the polarimeter when errors are present in the alignment of the optic axis of the QWP, retardance of the QWP and the alignment of the GTP, the compensating polaroid.

This algorithm is used to remove the cross-talks between the Stokes parameters introduced by the polarimeter alone.

3.6 Testing of Waveplate

Waveplates or retarders are essential in any polarimetric system which measures all the four Stokes parameters. It is necessary to know the characteristics of the waveplate before using it in any scientific instrument. The errors in the waveplate can limit the accuracy of the polarimetric system (West and Smith, 1995). Hence, the accurate measurement of the retardance and the direction of the optic axis is needed before using the waveplate for polarisation analysis. The optical properties of the waveplate, made from a birefringent material, has been studied using different techniques in order to measure the phase retardation precisely (Walter, 1978; Nakadate, 1990; Chidester, Harvey and Hubbard, 1991; Shyu, Chen and Su, 1993). Different methods use different techniques and in general a precision ellipsometric system is needed to measure any arbitrary retardance. Interferometric ellipsometry can be used for the measurement of retardance quite accurately.

3.6.1 Method

Babinet Compensator (BC) can be used as an ellipsometer to measure the ellipsometric angles of any retarding system (Azzam and Bashara, 1977; Born and Wolf, 1984; Sankarasubramanian and Venkatakrishnan, 1996). The principle of the method is the following. When a collimated linearly polarised beam is analysed after passing through the BC, fringes are formed (as explained in Chapter 2; Section 2.4). The contrast and the position of the fringes depend on the input state of polarisation. Hence the fringes formed at the BC gets shifted and the contrast reduces, whenever a waveplate is introduced in front of the BC. From the measurement of the fringe shift

the phase difference which has been introduced by the waveplate can be calculated. However, the fringe shift produced by the waveplate not only depends on the phase difference introduced at the waveplate, but also depends on the angle between the optic axis of the waveplate and the direction of vibration of the input linearly polarised light. The measurement of the fringe shift for different orientation of the optic axis has been taken in this experiment to find out the retardance with better accuracy.

There are several methods to measure the retardance using a BC with high accuracies (Jerrard, 1948). The accuracies involved in the double-pass method used by Hariharan and Sen (1960) is found to be better than the retardance calculated using fringe shift measurement. But the double-pass method needs better photometric accuracies and a stable source to achieve an accuracy of 0.5° in the retardance. The initial knowledge about the orientation of the optic axis of the waveplate is essential in all the methods. The optic axis of the crystal has to be kept at 45° to the direction of vibration of the input linearly polarised light. Again finding out the optic axis of a waveplate requires a crossed polaroid arrangement and the accuracy in finding out the direction of the optic axis depends on the sensitivity of the setup to intensity variations. The inaccuracies in the optic axis determination can give a wrong estimation of the retardance. The determination of the retardance using the heterodyne interferometric techniques developed recently is much superior in terms of the accuracies achieved (Lin, Chou and Chang, 1990; Chou, Huang and Chang, 1997) but it has not yet been applied to the mapping of the retardance errors on the waveplate. An optical setup is developed which measures the retardance of birefringent waveplates without requiring the knowledge about the optic axis. In fact a proper analysis gives the optic axis orientation also with better accuracy.

The measurement of the retardance using BC has been discussed long back (Hariharan and Sen, 1960). In all the cases, the BCs used were variable compensators and the fringe shift was measured using a telescope and a micrometer screw arrangement with manual adjustment. The waveplates were kept with its optic axis at 45° to the

input linearly polarised light. The accuracy with such a system was shown to be of the order of few degrees (Hariharan and Sen, 1960). Using a two dimensional detector (CCD) in place of the micrometer screw-telescope arrangement to record the fringes and analysing the recorded fringes further to measure the fringe shift with a fraction of a pixel accuracy, lead to an accuracy in the retardance measurement of about 2°. By finding the fringe shift for different orientations of the optic axis of the waveplate and fitting a model for the observed fringe shift will increase the accuracy in the retardance calculation further.

3.6.2 Experiment

The experimental setup is given in Figure 3.4. Light from a monochromator is passed through a BC, which is kept in between a crossed polariser (P1 and P2 in Figure 3.4). An EEV-CCD is used to record the fringes formed at the BC with the help of a frame grabber DT-IRIS 2861. The whole setup is aligned and adjusted such that the fringes are along the CCD row and of good contrast in the full field of view. The waveplate to be tested is mounted on a rotating system (R1), which rotates with the help of a stepper motor with a step correspond to an angle of 4.5°, and kept in the collimated beam between the input polariser and the BC to enable the measurement of the fringe shift for different orientation of the optic axis of the waveplate. This rotating system is a part of the polarimeter developed for the polarisation observation of sun at the KTT (Ananth *et al*, 1994). Fifteen frames for fifteen orientations of the optic axis of the waveplate are taken in this experiment to calculate the retardance.

The stepper motor, CCD and the DT-IRIS 2861 are interfaced to a 286 computer and signals for the integration time (to get a good signal to noise ratio), number of frames to be taken for different orientation of the optic axis of the waveplate and the steps between each frame (minimum of 4.5°) can be given by the user with the help of a FORTRAN program. The reference position marked in the rotating system

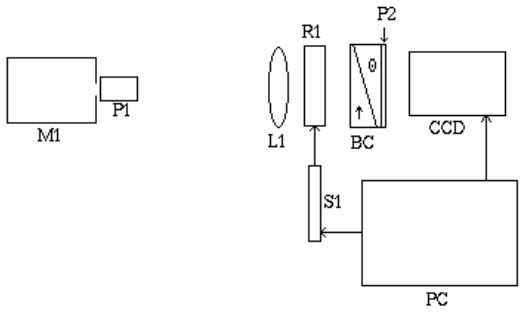

Figure 3.4: Block diagram of the experimental setup. M1 - Monochromator, P1 - Prism polariser, L1 - Collimating lens of 20 cm focal length, R1 - Stepper motor controlled rotating stage, S1 - Stepper motor controller, BC - Babinet compensator, P2 - Analyser crossed with P1, CCD - Charge coupled detector, PC - 286 PC to control the stepper motor and the CCD.

can be sensed by an IR sensor and used as a reference for finding out the optic axis of the waveplate from the fringe shift calculation. The axis of the waveplate can be kept at an arbitrary angle to this reference position. A maximum of fifteen frames corresponding to the fifteen orientations of the waveplate optic axis can be frame grabbed online with the frame grabber card DT-IRIS 2861. To cover the fringe shift in both direction of the reference fringe a rotation of 180° in the waveplate orientation is required. A rotation of 13.5°, which corresponds to three steps in the stepper motor used in this experiment, is chosen so that a rotation of 202.5° of the waveplate can be covered with fifteen frames.

The procedure of the experiment is the following: At first the reference position is sensed by the IR sensor and the stepper motor stops at that position. Then the exposure time (t), number of positions of the optic axis of the waveplate (nop) required and the number of steps (n) between each position is fed by the user. The

first frame, which contains the fringes formed by the waveplate, BC and polaroid assembly, is grabbed for this reference position. Once, the frame is grabbed for this position as signaled by the DT-IRIS 2861 card, the stepper motor steps 'n' number of steps and stays at that position for the next frame to be grabbed. This repeats for 'nop' positions and the grabbed frames which are temporarily stored in the frame grabber buffer are then transfered to the hard disk of the 286 computer. The further analysis are done on a sun workstation to get better accuracies using Interactive data language (IDL) software. All these procedure can be easily implemented as an online process by using a 486/pentium processor with a FORTRAN compiler.

3.6.3 Theory

Each of the optical components in the experimental setup given in Figure 3.4 can be represented by a Mueller matrix (only for polarisation analysis) and the final Mueller matrix can be calculated by just multiplying the individual Mueller matrices in order (Shurcliff, 1962). Assuming θ as the angle of the optic axis of the waveplate with respect to the axis of the BC and Δ as the retardance of the waveplate, it can be shown that the output intensity of the above described setup is,

$$I(x,y) = \frac{1}{4}[1 - \sin^2 2\theta \cos\delta(y) - \cos^2 2\theta \cos\delta(y)\cos\Delta + \cos 2\theta \sin\Delta \sin\delta(y)] \quad (3.3)$$

where, δ(y) = $\frac{4\pi}{\lambda}$ (n_e-n_o) y tan(A)

A = Angle of the wedge of BC

λ = wavelength of the light used.

y = The spatial position in the y-direction

Equation 3.3 gives the intensity in the detector plane which is a function of the spatial direction x and y. However, since the parameter δ, which is the retardance introduced by the BC, is only a function of y, the output intensity is independent of x. The fringes are aligned with the CCD row (x direction), so that the shift in the

fringes will be only along the y-direction (CCD column). Differentiating Equation 3.3 with respect to y, the position of the intensity minima are given as,

$$y_{min} = \frac{1}{C}\tan^{-1}[\frac{\cos 2\theta \sin \Delta}{(1-\cos\Delta)\cos^2 2\theta - 1} + m\pi], m = 0, 1, ... \tag{3.4}$$

where C is a constant for a particular wavelength which converts the retardance in radians to the fringe shift in number of pixels.

$$C = \frac{4\pi(n_e - n_o)\tan(A)}{\lambda} pixsiz \tag{3.5}$$

where pixsiz is the size of a pixel which here is 22μ.

It can be seen from the Equation 3.5 that when the waveplate is introduced with its optic axis at 0° to that of the BC (i.e., $\theta = 0°$) the fringe shift will be proportional to the retardance Δ introduced by the waveplate. Assuming θ_1 as the angle between the optic axis of the waveplate and a reference position in the rotating system (θ_1 can be called as an initial off-set angle), n as the number for each frame which is captured and $\delta\theta$ as the angle between each steps then, the position of intensity minima y^n_{min} for m=0 can be written as,

$$y^n_{min} = \frac{1}{C}\tan^{-1}[\frac{\cos 2(\theta_1 + n\delta\theta)\sin\Delta}{(1-\cos\Delta)\cos^2 2(\theta_1 + n\delta\theta) - 1}] \tag{3.6}$$

The above equation is consistent for the optical system described above and used for further analysis of the fringe shifts.

Once the fifteen frames are taken for different orientations of the optic axis of the waveplate, the fringe shift for each frame are calculated using the phase shift matching technique (Wang, Bryanston-cross and Whitehouse, 1996a). The first frame (i.e., n=0 in Equation 3.6) is taken as the reference frame and the other frames (i.e., n=1 to 14) are compared with this. The phase shift matching technique, used for calculating the phase difference between two interferograms, is used to calculate the fringe shift. The complete algorithm with simulation and experimental verification is given by Wang, Bryanston-cross and Whitehouse (1996a) and Wang *et al* (1996b) which can be referred for the details. The principle of the method is to reduce the rms residue

of the difference of a region of the two interferograms by shifting one with respect to the other. The shift which gives the minimum rms residue will be the true shift. A phase curve which is the plot between the shift in pixels to the rms residue is obtained. The minimum in this phase curve will give the value of the fringe shift in pixels. An interpolation scheme is used around this minimum of the phase curve in order to increase the determination of the minimum to sub-pixel accuracy. The simulation without noise shows an achievable accuracy of one hundredth of a pixel in the fringe shift calculation. For the real case with noise the accuracy in the fringe shift calculation is one tenth of a pixel. The advantage of this method over other methods is that it gives reasonably correct fringe shifts even in the presence of noise since the phase shifts are modulated in a particular frequency bin and extracted back by picking up only that frequency bin whereas the white noise will exist equally in all the frequency bins.

3.6.4 Mica Waveplates

Zero-order quarter waveplate for λ=6122Å, which is a magnetically sensitive line for Zeeman polarisation measurement of magnetic regions on the sun (Rust and O'byrne, 1990), was made from mica sheets. This waveplate was mounted on the rotating assembly and tested for its retardance. Figure 3.5 shows the 300th column cut of the fringes for two different orientation of the waveplate. The fringe shifts are calculated for different orientations of the optic axis of the waveplate by using the first frame as the reference frame. The same region of size 200 $\times$ 150 pixels is used to calculate the fringe shift for all the frames. A parametric search algorithm, which minimises the following function by varying θ_1 and Δ over a range, was used to find out the best fit with the observed fringe shift.

$$\sigma^2(\theta_1, \Delta) = \sum_{i=1}^{15} (y_i - y_i^{the})^2 \tag{3.7}$$

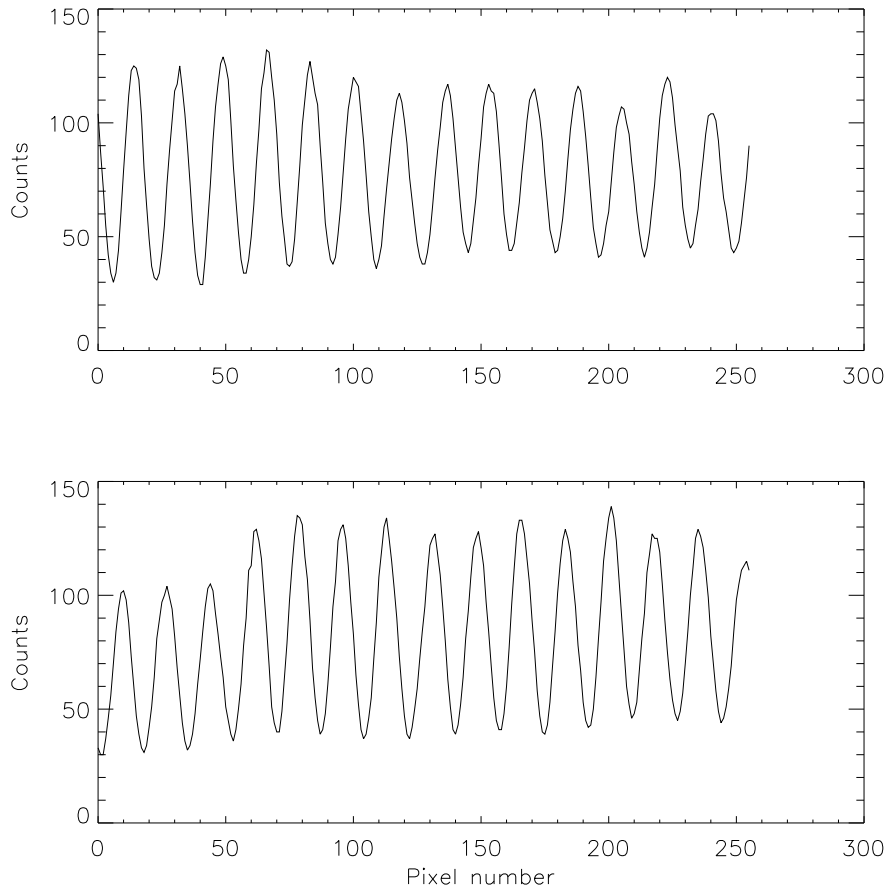

Figure 3.5: The $300th$ column cut of two different frames taken with two different orientation of the optic axis.

where y_i are the calculated fringe shifts from the phase matching algorithm and y_i^{the} are the theoretical fringe shifts calculated from Equation 3.8.

$$y_i^{the} = y_{min}^{n} - y_{min}^{0} \tag{3.8}$$

Figure 3.6 shows the calculated fringe shifts from the phase matching algorithm as asterisks and the fitted theoretical curve as solid line for a particular parameter θ_1 and Δ which minimises the function σ^2.

Commercial high-order quarter waveplate at λ=6302Åmade of quartz is also tested with this technique. Figure 3.7 shows the calculated fringe shift for different position of the optic axis as asterisks and the best fitted curve as solid line for the high-order

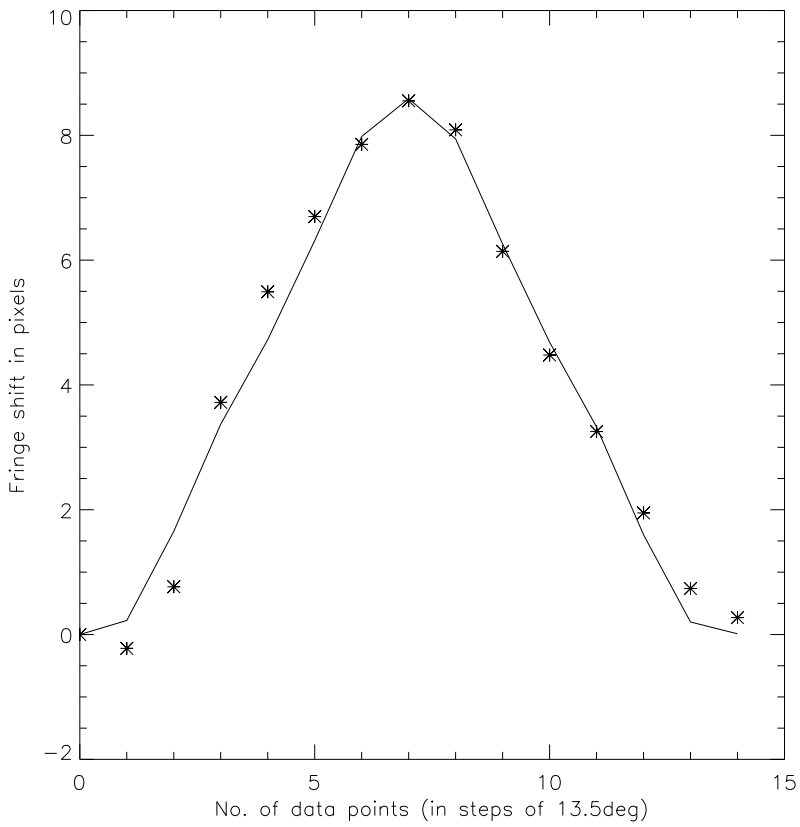

Figure 3.6: The calculated fringe shifts for different positions of the optic axis of the zero-order mica quarter waveplate using the phase matching algorithm and the best fitted model. The calculated data points are shown as asterisks and the best fitted curve is shown as solid line. The parameters for the best fit are $\theta_1 = 85.7 \pm 0.3°$ and $\Delta = 89.1 \pm 0.5°$.

quarter waveplate. It is clearly seen that the best fit in this case has much more deviation than the zero-order case. Table 3.2 lists the experimental results for the zero-order and higher order waveplates along with the accuracies.

The variation of the fringe width with wavelength is used to find out the accuracy in the fringe shift calculation and the accuracies achieved are listed in the second column of the Table 3.2. For a BC, the fringe width is given in terms of number of

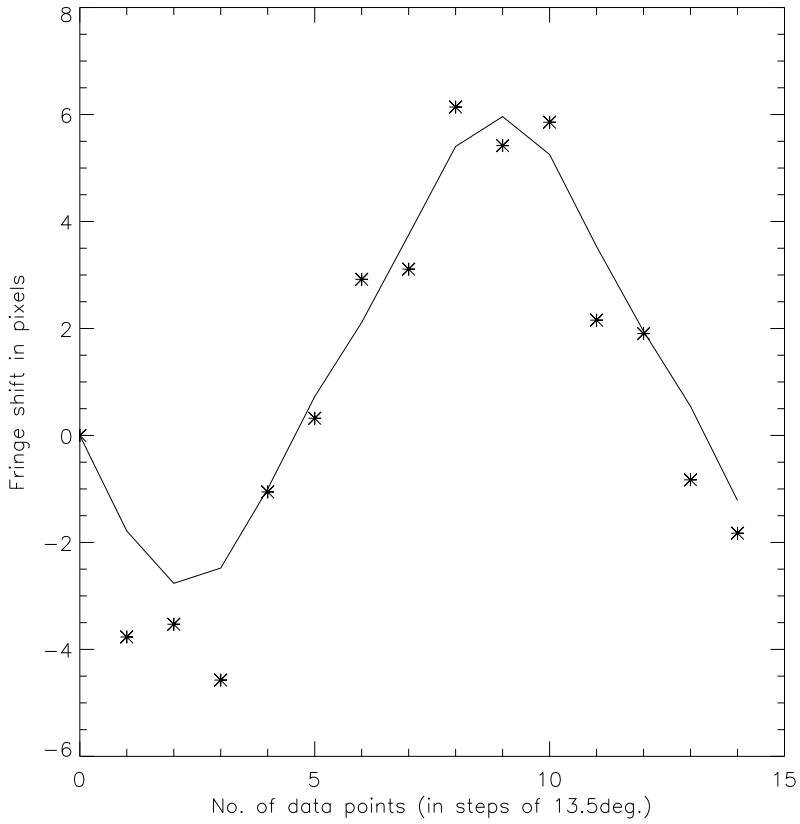

Figure 3.7: The calculated fringe shifts for different positions of the optic axis of the higher order quarter waveplate and the fitted curve. The parameters for the best fit are $\theta_1 = 59.3 \pm 0.3°$ and $\Delta = 87.8 \pm 0.9°$.

pixels (with 22μ as one pixel) as,

$$Fringe\ Width\ (FW) = \frac{\lambda}{4.(n_o - n_e).\tan(A)}.pixsiz \tag{3.9}$$

The theoretical variation of the fringe width with wavelength (as given in the above equation) is compared with the measured fringe width and the root mean square deviation averaged over wavelength is taken as the experimental accuracy of the fringe shift calculation. The variation of (n_e - n_o) with λ is taken from Hariharan (1996). Figure 3.8 shows the measured fringe width for different wavelengths of the input light beam. The solid line is the fitted line using the Equation 3.9

The accuracy in the retardance calculation from the parametric search are found

Table 3.2: Measured retardance of the waveplates

Waveplate	Accuracy in fringe shift calculation (in pixels)	Accuracy in Retardance calculation (in degrees)	Accuracy in optic axis orientation (in degrees)	Calculated Retardance (in degrees)	Orientation of the optic axis* (in degrees)
Zero-order	0.1	0.5	0.3	89.1	85.7
Higher order	0.1	0.9	0.3	87.8	59.3

* The orientation of the optic axis is calculated with respect to a reference position marked in the rotating system.

out and listed in the third column of the Table 3.2. The least square fitting used is a non-linear fit and hence there is no analytical formula for the calculation of errors in the fitting parameters (Bevington, 1969). In an approximate way the uncertainty in the fitting parameter can be defined as that change in the parameter value which gives a change in the value of the residuals χ^2 of unity. i.e.,

$$\chi^2(a+\epsilon) = \chi^2(a) + 1 \tag{3.10}$$

where 'a' is the fitting parameter, 'ϵ' is the uncertainty in 'a' and χ^2 is related to the σ^2 defined in Equation 3.7 by,

$$\chi^2 = \frac{\sigma^2}{\sigma^2_{ins}} \tag{3.11}$$

Equation 3.10 is valid for an experimental setup which has an uniform uncertainty

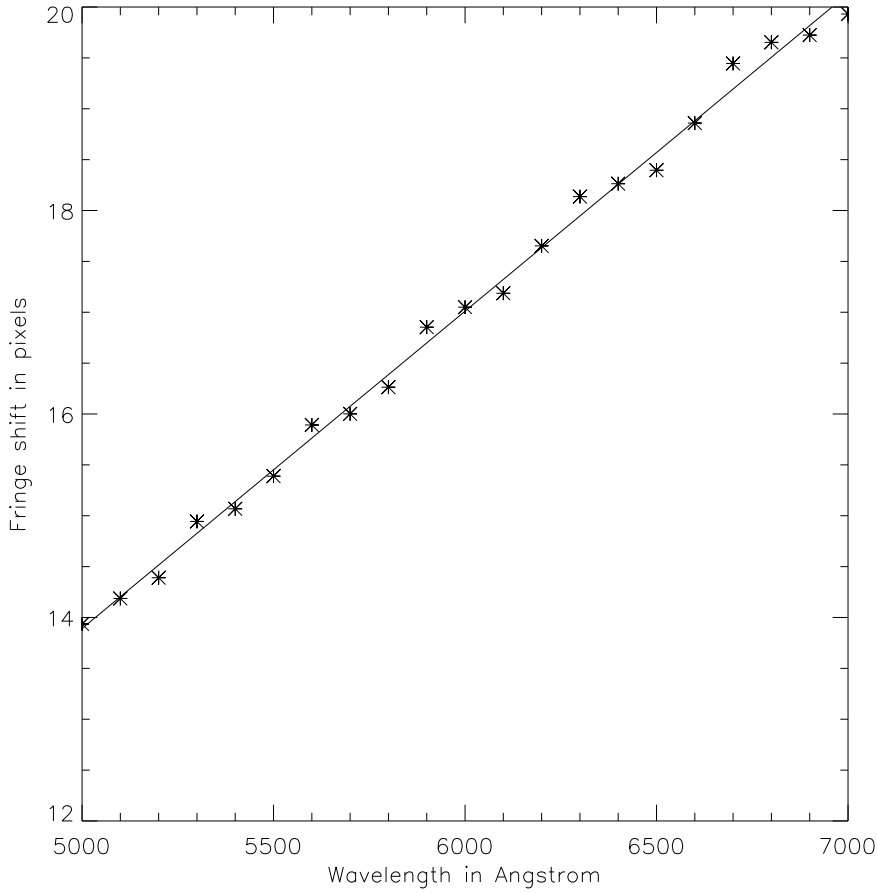

Figure 3.8: The measured fringe width for different wavelengths of the input light beam is shown as asterisks. The solid line is the theoretical model for the fringe width as given by Equation 3.9.

σ^2_{ins} for all the measured data points. Here, the uncertainty (of 0.1 pixel) in the fringe shift measurement is taken as the σ_{ins}

3.6.5 Testing of the QWP

A similar set up as described above is used to test the QWP used in the polarimeter of the KTT. A manual rotation of the waveplate is performed in order to get finer sampled data. The fringe shift is calculated for every 10° rotation of the QWP. Figure 3.9 shows a plot of the fringe shift for different rotation angle of the QWP.

The best fit shows that the retardance of the QWP is 94.7°±0.3° and the initial offset of the QWP axis is 82.3°±0.2°.

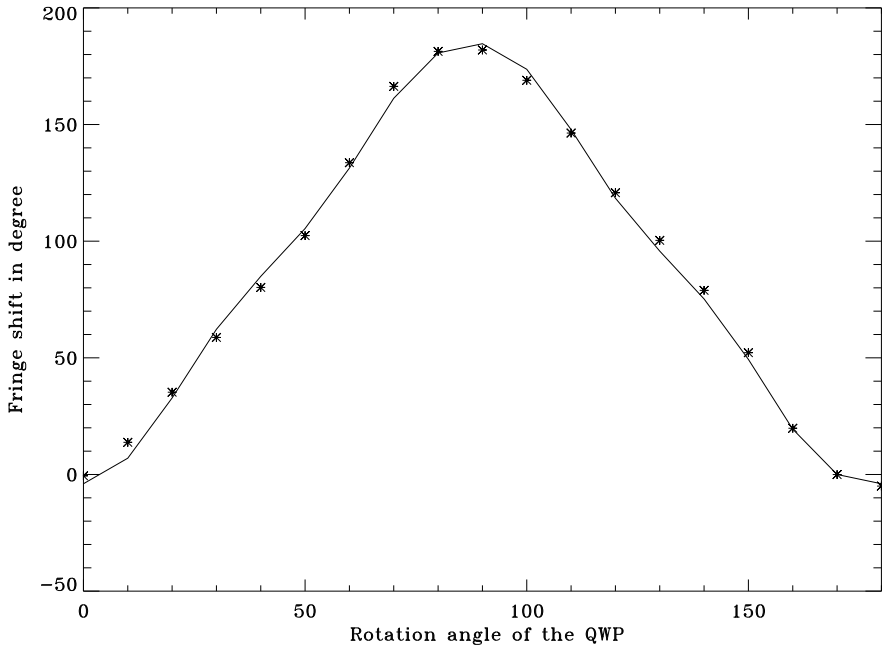

Figure 3.9: Measured fringe shift in degree for different rotation angle of the QWP are shown as data points. The solid line is the best-fit model.

3.6.6 Discussions and Improvements

In this section, a technique to calculate the retardance of any birefringent material using BC with CCD as a detector is discussed. Although the accuracy achievable in the retardance is 2° with a single measurement, a series of fringe shift measurements are taken by keeping the optic axis of the waveplate at different orientation and a theoretical model for the experimental setup is fitted to get an accuracy of 0.5° in the retardance for zero-order waveplate and 0.9° for high-order waveplates. The accuracy achieved for zero-order waveplate are more than for the high-order waveplate.

By taking each single column cut, the variation of the fringe shift over a region is also calculated and shown in Figure 3.10. This shows the one dimensional surface

variation of the retardance of the waveplate. The rms variation of the fringe shift variation in Figure 3.10 is 0.06 pixel over a region of 0.44 cm. This sigma is of the order of the uncertainty in the fringe shift calculation. Hence, the surface variation of the retardance of the waveplate is less than 0.5° for the zero-order waveplate which has been made in the laboratory using mica.

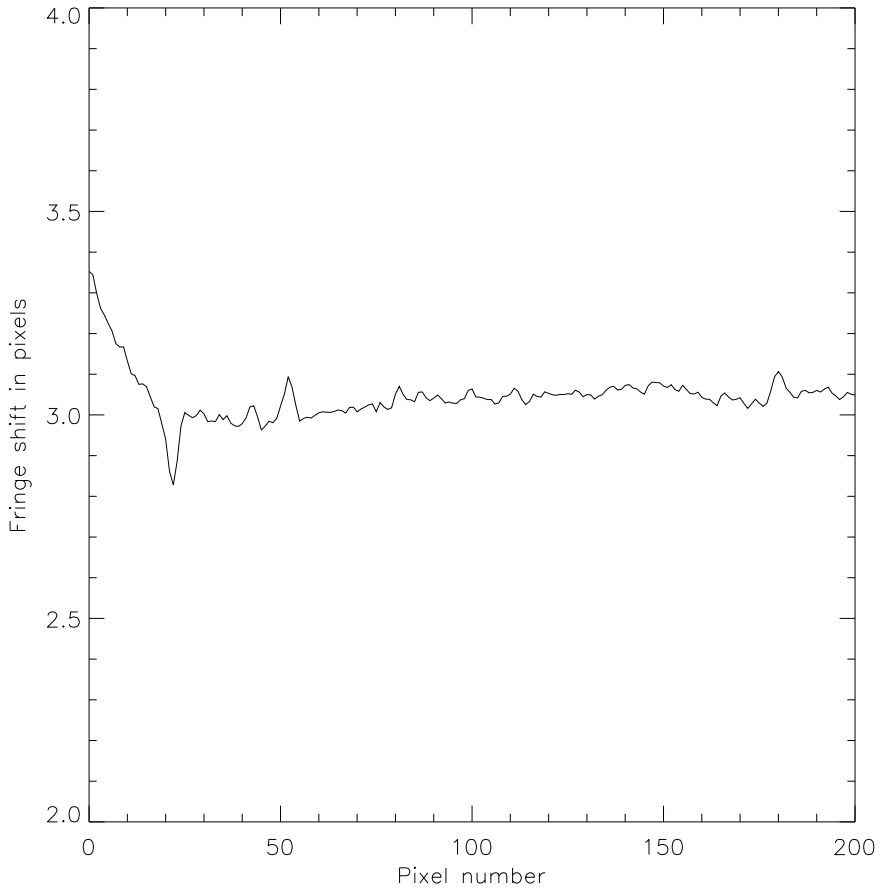

Figure 3.10: Variation of the fringe shift over a region of about 0.44 cm for the zero-order mica quarter waveplate. The root mean square deviation is 0.06 pixel which is almost equal to the experimental accuracy.

The inherent advantage of this technique is that it does not require any knowledge about the axis of the waveplate. Since it works on the basis of fringe shift calculation, the stability of the input source does not affect the retardance and the optic axis

direction calculation. The surface variation of the retardance of the waveplate can also be studied with the same setup. But it requires an extensive calculation before finding out the retardance and the optic axis direction.

The wedge angle 'A' used for this experiment is 5°. A BC with a wedge angle of 0.5° will give a fringe shift and fringe width of about one order more than the present case. This will definitely improve the accuracy in the retardance measurement. The same experiment can be repeated for several wavelengths and a model can be fitted to find out the retardance value with better accuracy. With the same setup and increasing the number of measurements by reducing the angle between each measurement (currently 13.5°), the least square fitting can be improved which will definitely reduce the uncertainty in the fitting parameters θ_1 and Δ. In conclusion, a retardance measurement of less than 0.1° seems possible with the above improvements.

3.7 Testing of Polarisation Optics

A laboratory test has been carried out in order to look for the mis-alignments of the polarisation optics of the polarimeter. The optical setup used is given in Figure 3.11. A monochromator is used to send $\lambda\lambda$6302Å light into a polarising Rochon prism. A 20 cm focal length convex lens is used to collimate the beam and sent through the polarimeter, CCD assembly. An aperture is used in front of the polarimeter in order to limit the size of the beam falling on the masked CCD arrangement. Stokes Q, U and V are measured by varying the transmission axis of the input polarising prism. Data are taken for every 5° rotation of the input polarising prism. The exposure time used is between 200 to 600 msec.

Figure 3.12 shows the measured Q/I, U/I and V/I as data points. Since the input is 100% linearly polarised light (polarising prism), the modulation in V/I will give the mis-alignment in the QWP and the error in the retardance. The mis-alignment in the GTP can be identified from the Q/I and U/I modulation. A simple model

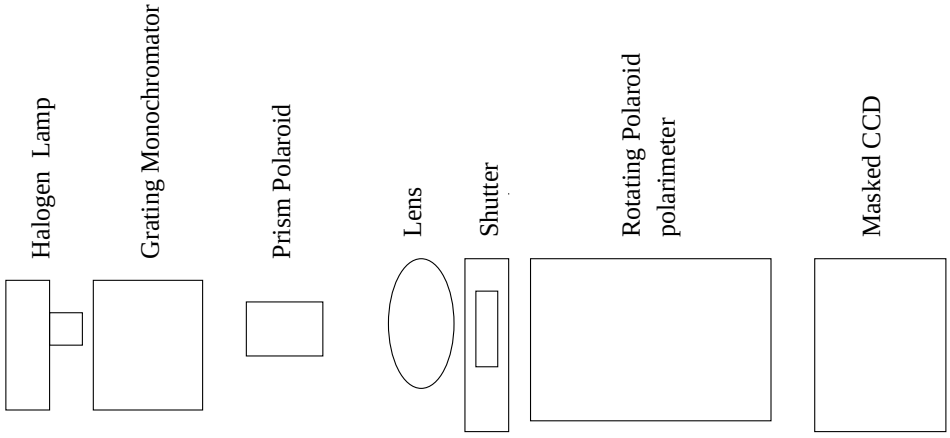

Figure 3.11: Block diagram of the experimental setup used to test the mis-alignment of the optics in the polarimeter. The optical components of the setup are marked in the figure.

is used for the optical set up shown in Figure 3.11 using the Mueller matrix of the optical elements. Figure 3.13 shows the model fit to the measured data points with the mis-alignments and error in the QWP retardance as free parameter. The best fit shown in Figure 3.13 will give the mis-alignments of the polarimetric analyser axis, the QWP axis and the error in the retardance. Table 3.3 compares the parameters for an ideal polarimeter and the derived values from the best fit. These parameters have to be used in order to remove the spurious polarisation signals produced by the polarimeter alone.

3.8 Combined performance with the Spectrograph and the KTT

The response of the grating to the input polarised light is measured by sending the sunlight through the polarimeter without introducing the QWP. Since the polarimeter is a rotating analyser, the output light will be polarised and the azimuth will be changing depending on the position of the analyser. The rotating analyser is rotated

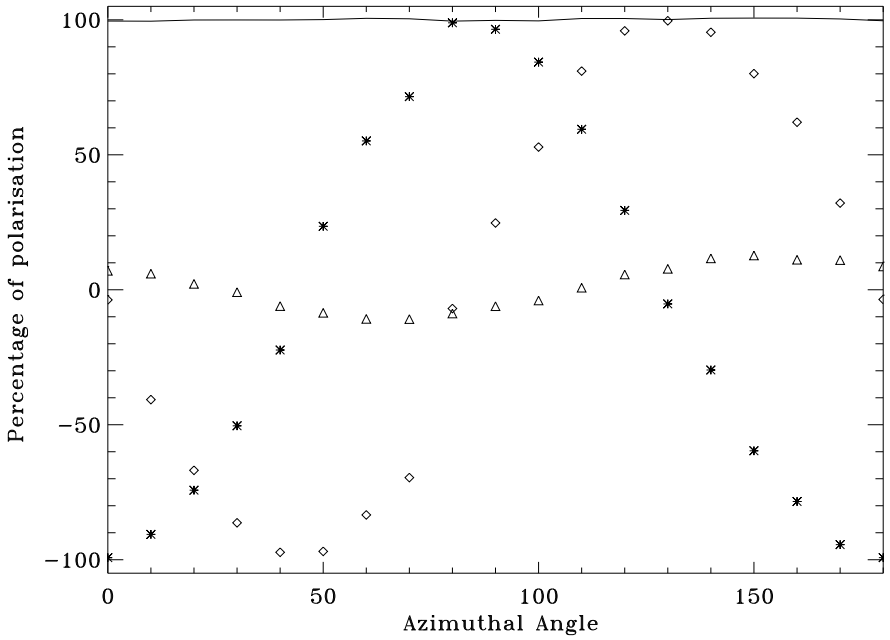

Figure 3.12: The measured percentage degree of polarisation for Q, U and V are plotted for different values of the azimuthal angle of the input prism polaroid. The data plotted with asterisk symbol is for Q and the diamond symbol is for U whereas the triangle symbol is for V. The solid line is the total polarised light and the variation in the total polarisation is less than 0.4%

for every 1.8° and the continuum intensity is measured for each position. A simple model for the grating response has been developed in order to estimate the response. The output intensity is related to the grating response coefficient as,

$$I(\theta) = G_{11} + G_{12}\cos(2\theta) + G_{13}\sin(2\theta) \tag{3.12}$$

where G_{11}, G_{12} and G_{13} are the response coefficient for the grating. Figure 3.14 shows the measured data and the best fit of this simple model. The derived response coefficients are $G_{11} = 1.0$, $G_{12} = 0.85$, and $G_{13} = 0.0$.

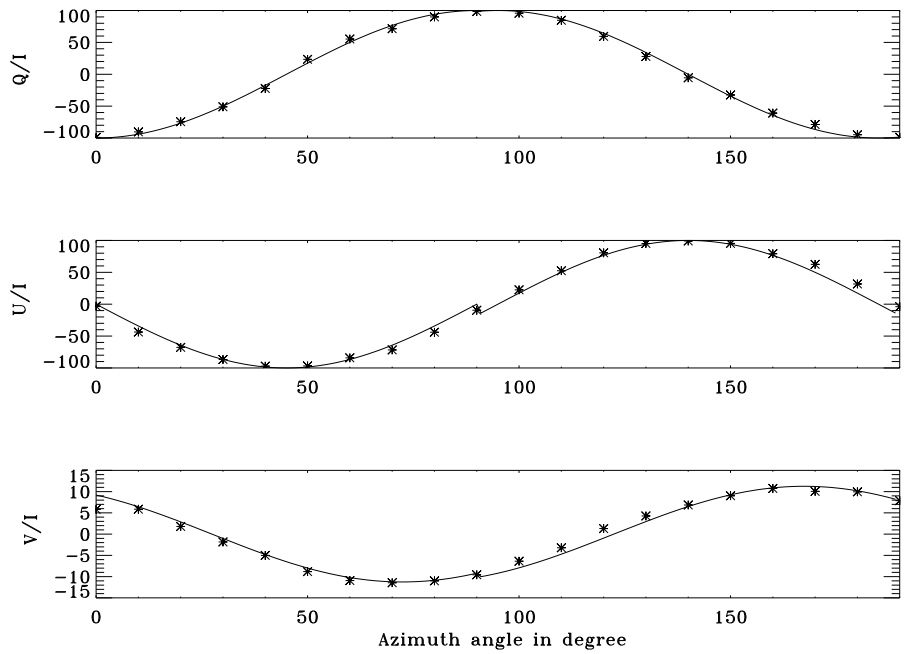

Figure 3.13: The measured data, shown as asterisk symbol, for different azimuthal angle of the input polaroid axis is fitted with the theoretical model (shown as the solid line). The best fit parameters are tabulated in Table 3.3. The kink in the fitted profile around 90° is because of a 5° sudden shift in the rotation of the input polaroid.

3.9 Conclusions

In this chapter the modulator and demodulator for the polarimeter developed for KTT was discussed. A CCD based polarisation interferometric technique was developed in order to characterise the QWP used for the polarimeter. An optical setup was used to find out the mis-alignments of the polarimetric optics. The combined performance of the polarimeter with the grating of the spectrograph at the KTT was described. The critical parameters, the retardance and the positional error in the waveplate, the positional error in the GTP and the compensating polaroid, to characterise the polarimeter was found out. These parameters will be used in the actual observation in order to eliminate the spurious polarisation signal produced by the polarimeter alone.

Table 3.3: Measurement of the mis-alignments of the optical axis of the polaroid and QWP and the retardance error of QWP.

Component	Parameters for an ideal polarimeter	Parameters measured
QWP - Axis	45° from the slit direction	43.0±0.3° from the slit direction
QWP - Retardance	90°	95.5±0.5°
Analyser - Axis	45° from the slit direction	45.0±0.3° from the slit direction
Compensating polaroid	45° from the slit direction	44.0±0.5° from the slit direction

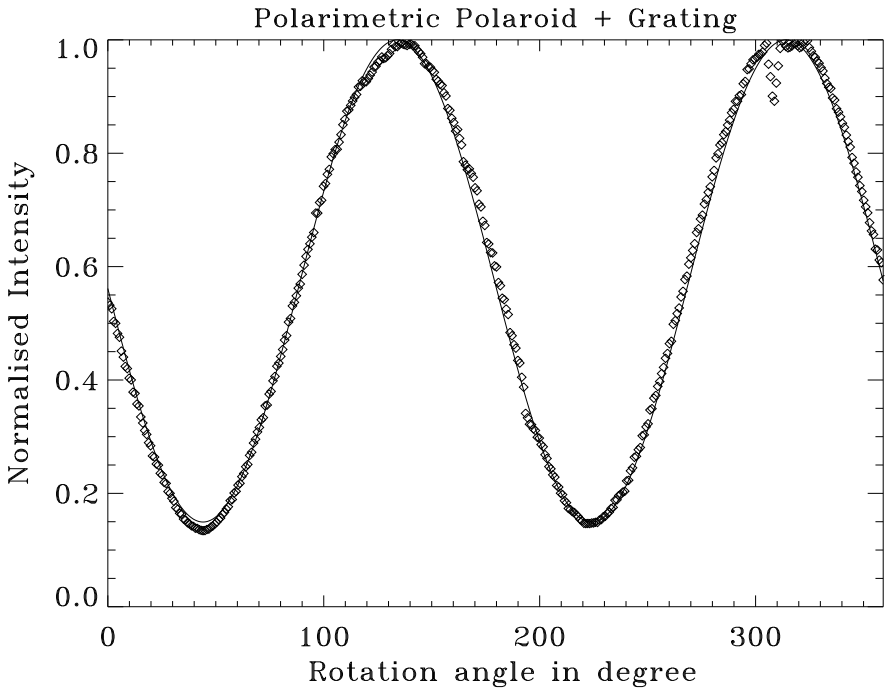

Figure 3.14: The grating response to the input linearly polarised light. The x-axis is the azimuth of the polarised light and the y-axis is the normalised intensity of the grating response. The scattered data points near azimuth angle 300° is because of passing clouds.

Chapter 4

Off-line Correction of Instrumental Polarisation

4.1 Summary

In this chapter, we present a model to calculate the Mueller matrix of the Kodaikanal tower telescope (KTT) in order to understand the polarisation properties of it. As already explained in Chapter 2, the model depends on the following three sets of parameters,

- The angle of incidence ('i') of the light on each of the three mirrors of the coelostat.
- The real ('η') and the imaginary ('κ') part of the refractive index of the aluminium coating on each mirror.
- The thickness ('t') of the oxide layer formed on the three aluminium coated mirrors assuming the value of the refractive index for the oxide layer as 1.77 (Lide, 1995)

The angle of incidence, 'i' can be calculated precisely from the geometry of the KTT installation using spherical trigonometry. The model for the geometry of the KTT installation developed by Balasubramaniam, Venkatakrishnan and Bhattacharyya (1985), has been modified to include the initial reference co-ordinates on the sky plane. The modified model is very similar to the one developed for the Arcetri Solar Tower (Capitani *et al.,* 1989). However, the model developed now for the KTT includes the oxide layer formed on the aluminium mirrors. The refractive indices of the mirror coatings and the oxide layer thicknesses are taken as the free parameters. To determine these free parameters, the model is fitted with the observed daily variation of the instrumental polarisation produced by the telescope and the polarimeter when it is illuminated by an unpolarised light.

Once these free parameters are estimated, the Mueller matrix of the KTT can be calculated and then be inverted from the observed Stokes profiles in order to get the unmodified profiles. The error in the estimated free parameters will introduce an error in the correction of the instrumental polarisation. These errors will generate a spurious polarisation signal in the corrected Stokes profiles. The maximum spurious polarisation signal in these corrected profiles are estimated to be about 0.5% in Q, 0.9% in U, and 0.2% in V.

4.2 Introduction

Any oblique reflecting surface will change the polarisation state of the input beam. Hence the study and the measurement of the telescope instrumental polarisation is essential, particularly for the case of oblique reflecting telescopes like KTT. As discussed in Chapter 2, the complete Mueller matrix of the telescope can be obtained by measuring the refractive indices of the mirror coatings with the oxide layer thicknesses if the geometry of the telescope installation is known. An ellipsometric method is implemented at the KTT in order to measure the refractive indices of the three

mirror coatings and the thicknesses of the oxide layer formed on it (see Chapter 2 of this thesis and Sankarasubramanian, K., Samson, J. P. A., and Venkatakrishnan, P., 1999 for details). The main result from the ellipsometric measurement is that the model for the reflecting mirrors of the coelostat should include the oxide layer formed on it in order to minimise the error in the inversion of the instrumental polarisation. It is practically difficult to do the ellipsometric measurement before or after each observations. Another method using the polarisation observation of unpolarised light is implemented in order to verify the ellipsometric measurement as well as the telescope model.

The principle of the method is simple. The continuum spectra at the disc center in the red wavelength region is practically unpolarised ($<< 0.01\%$, Fluri and Stenflo, 1999a; Fluri and Stenflo, 1999b). Hence the polarisation observed in the continuum is produced by the telescope and the associated instrument used for the polarisation measurement. If 'M' is the combined Mueller matrix of the KTT and the polarimeter, then the measured Stokes vector is given by,

$$\begin{aligned} [I_p, Q_p, U_p, V_p]^T &= M.[I, 0, 0, 0]^T \\ &= [M_{11}, M_{21}, M_{31}, M_{41}]^T I. \end{aligned} \tag{4.1}$$

where the superscript 'T' represents a transpose operation. It is obvious from the above equation that the observed continuum polarisation at the disk center in the red wavelength is the first column of the combined Mueller matrix of KTT and the Stokes polarimeter. It will be shown in this chapter that the first column of this combined Mueller matrix is a function of the refractive indices of the three mirror coatings, the oxide layer thicknesses and the angles of incidence of the unpolarised light on the three mirrors. On any day, the observed continuum polarisation will change with time although the variation of the refractive indices and the thicknesses of the oxide layer is practically zero. The reason for this variation is that the angles of incidence on the three mirrors are different for different observing time. By fitting the observed polar-

isation variation with time to that of the model, the free parameters, the refractive indices and the thicknesses of the oxide layer can be found out with the assumption that the model gives a very accurate value for the angles of incidence. Similar kind of measurements have already been developed for other telescopes, particularly for the Mc Math-Pierce Telescope (Bernosconi, 1997) and the Dunn Solar Telescope (Elmore *et al.,* 1992).

4.3 Model for the KTT

The imaging system at the KTT is a three mirror coelostat system and an achromatic refractor (Bappu, 1967). The sunlight from the first mirror is reflected on to a secondary mirror which in turn reflects the light vertically down to a third mirror. The third mirror reflects the light horizontally on to a 38 cm lens which images the sun on to the slit of a Littrow mount spectrograph. The first mirror revolves around the polar axis with a frequency which can be set for the particular day of observation in order to compensate for the earth's rotation. The second mirror faces the first and the third mirror. This mirror can be moved in two axis in order to focus a particular region on the sun on to the slit of the spectrograph. The two axis of the second mirror can be controlled using a hand set which has both coarser and finer movement control switch.

The first mirror in turn can be moved along the earth's N-S direction for different declinations of the sun in order to reflect the sunlight on to the second mirror since the center of the second mirror is fixed. When the sun is at certain declinations, the mount of the second mirror can cast a shadow on the first mirror when the sun is around noon. This disadvantage is typical of this mounting and can be avoided by displacing the first mirror towards west.

4.3.1 Geometry of the coelostat system

The three mirrors of the coelostat system is projected on to the celestial sphere in order to calculate the angles of incidence of sunlight on each mirror. Consider a right handed, orthogonal co-ordinate system $(\hat{e_1}, \hat{e_2}, \hat{e_3})$ to be associated with each light beam with the unit vector $\hat{e_3}$ pointing along the ray direction. The polarisation properties of the beam is specified by the Stokes vector $[I, Q, U, V]^T$. The direction of $\hat{e_1}$ specifies the positive-Q direction.

Figure 4.1(a) shows the geometrical considerations of the KTT. C_1, C_2 and C_3 are the centers of first (M1), second (M2) and third mirror (M3), projected on to the celestial sphere, respectively. C_1 is taken as the origin for the celestial sphere and C_2 is the point where the direction joining M1 with M2 meets the celestial sphere. S is the position of the sun on the celestial sphere. N_1 is the direction perpendicular to M1 and it lies on the celestial equator since M1 revolves around the polar axis. ϕ is the latitude of KTT.

The geometric configuration given in Figure 4.1(a) corresponds to M1 displaced towards east during morning which is the usual configuration for the solar observations at KTT. However, some of the observations carried out for this thesis is taken with M1 placed in the west. Nevertheless, the model developed in this chapter can be used for both configurations.

Let I_s be the uncorrupted Stokes vector of light emerging from the sun, mainly due to the physical processes happening in the region of observation. Let I_s be defined in the right-handed reference system $(\hat{e_1}, \hat{e_2}, \hat{e_3})$, where $\hat{e_3}$ points towards C_1 and $\hat{e_1}$ is tangent to the celestial meridian through the center of the sun and points towards the north celestial pole P. Hence, the positive-Q is measured along the celestial meridian. The conversion from the celestial meridian to the heliospheric co-ordinates can be done using the data given in the Astronomical Almanac, through a rotation matrix with an angle θ_0, the angle between the direction of celestial meridian from the sun and the north pole direction of the sun. The angle θ_0 varies with the declination of

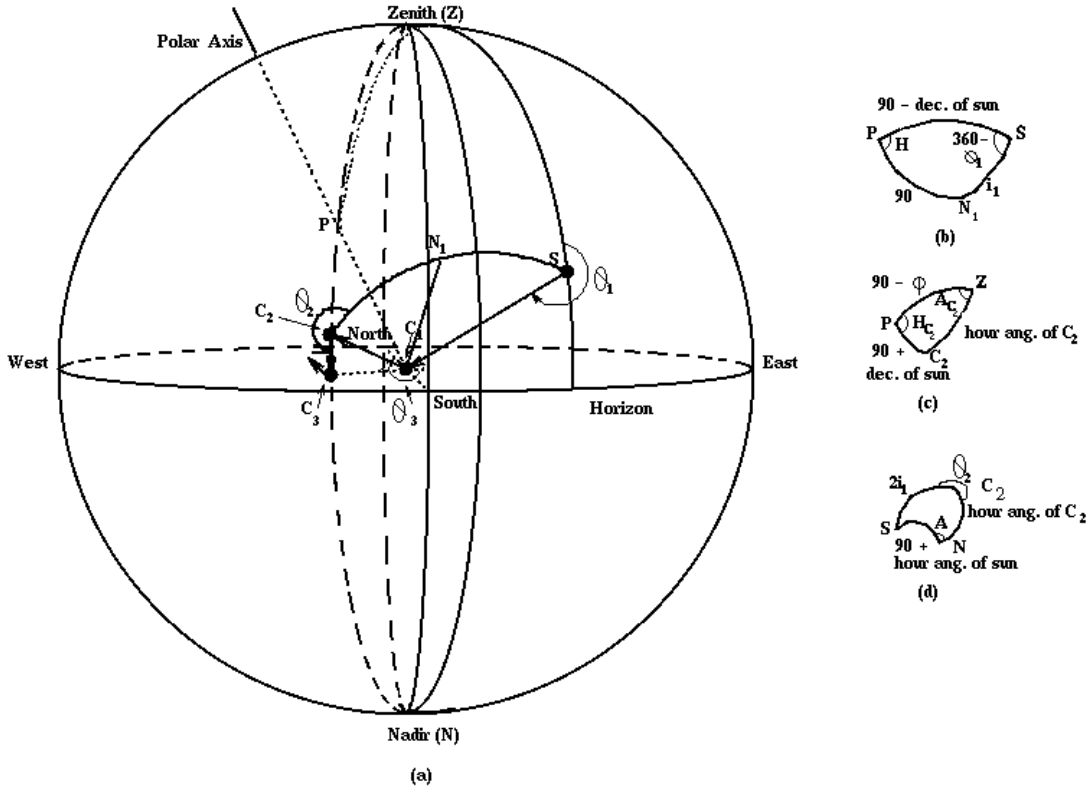

Figure 4.1: (a) The geometrical representation of KTT. The celestial sphere is centered on M1 (see text for details). (b) Spherical triangle PSN_1 is used for the calculation of the angles θ_1 & i_1. (c) Spherical triangle PZC_2 is used to calculate the hour angle of M2. (d) Spherical triangle SC_2N is used to calculate the angle θ_2.

the sun and can be calculated using the formulae given in the Astronomical Almanac. In order to evaluate how the polarisation changes in reflection on the first mirror, a preliminary rotation of the reference system $(\hat{e_1}, \hat{e_2}, \hat{e_3})$ has to be performed. The rotation is done to bring the unit vector $\hat{e_1}$ which corresponds to +Q direction, to the incidence plane SC_1C_2. This can be done through a rotation around the unit vector $\hat{e_3}$ of the angle θ_1 as shown in Figure 4.1(a). The modified Stokes vector $I_s^{'}$ after the

first mirror reflection is then given by,

$$I_s^{'} = M(i_1)R(\theta_1)I_s$$

where $M(i_1)$ and $R(\theta_1)$ are the reflection and rotation matrix defined by,

$$[M] = \tfrac{1}{2}\begin{pmatrix} 1+X^2 & 1-X^2 & 0 & 0 \\ 1-X^2 & 1+X^2 & 0 & 0 \\ 0 & 0 & 2X\cos(\tau) & 2X\sin(\tau) \\ 0 & 0 & -2X\sin(\tau) & 2X\cos(\tau) \end{pmatrix},$$

$$[R] = \begin{pmatrix} 1 & 0 & 0 & 0 \\ 0 & \cos(2\theta_1) & \sin(2\theta_1) & 0 \\ 0 & -\sin(2\theta_1) & \cos(2\theta_1) & 0 \\ 0 & 0 & 0 & 1 \end{pmatrix},$$

where,

$$\tan(\tau) = \frac{2b\sin(i_1)\tan(i_1)}{\sin^2 i_1 \tan^2 i_1 - (a^2+b^2)}, \tag{4.2}$$

$$X^2 = \frac{a^2+b^2-2a\sin(i_1)\tan(i_1)+\sin^2 i_1\tan^2 i_1}{a^2+b^2+2a\sin(i_1)\tan(i_1)+\sin^2 i_1\tan^2 i_1}, \tag{4.3}$$

and,

$$a^2 = \frac{1}{2}[\eta^2-\kappa^2-\sin^2 i_1+\sqrt{(\eta^2-\kappa^2-\sin^2 i_1)^2+4\eta^2\kappa^2}],$$
$$b^2 = \frac{1}{2}[-\eta^2+\kappa^2+\sin^2 i_1+\sqrt{(\eta^2-\kappa^2-\sin^2 i_1)^2+4\eta^2\kappa^2}].$$

Here η and κ are the real and imaginary part of the refractive index of aluminium coating. Similarly, the Stokes vector after reflection from the second and third mirror is obtained using a rotation matrix with rotation angle θ_2 & θ_3 and a reflection matrix with an angle of incidence i_2 & i_3 respectively. Finally, the combined Mueller matrix of the three mirror coelostat system can be written as,

$$I_s^t = MI_s = R(\theta_4)M(i_3)R(\theta_3)M(i_2)R(\theta_2)M(i_1)R(\theta_1)I_s. \tag{4.4}$$

Where I_s^t is the Stokes vector of the radiation falling on the input side of the polarimeter whose Mueller matrix is defined in Chapter 3. The polarisation effects due to the refractor present in the imaging system is not considered since it is a symmetric optics and will produce very little polarisation compared to the reflecting mirrors of the coelostat (atleast one to two order less, Chipman, 1995; Sanchez Almeida and Martinez Pillet, 1992). The rotation angles $\theta_1, \theta_2, \theta_3$ and the incidence angles i_1, i_2, i_3 can be calculated from the spherical trigonometry and is related to the position of the sun (declination $\delta_\odot$, hour angle $H_\odot$) and the geometric parameters of the coelostat. The combined Mueller matrix will have sixteen non-zero elements and all of them will depend on i_1, i_2, i_3 & η, κ. The inclusion of oxide layer will change the values of X^2 and τ (Equations 4.2 and 4.3) as explained in Chapter 2. This new X^2 and τ values, which includes the oxide layer are taken in this model instead of using Equations 4.2 and 4.3.

From the laws of reflection,

$$i.e.,\ C_2\hat{C_1}N_1 = \frac{1}{2}S\hat{C_1}C_2, \tag{4.5}$$

the following relation can be derived,

$$\delta_{C_2} = -\delta_\odot, \tag{4.6}$$

$$H_{N_1} = \frac{1}{2}(H_{C_2} + H_\odot). \tag{4.7}$$

Where H and δ denotes the hour angle and the declination respectively. The subscript C_2 and $\odot$ represents the mirror M2 and the sun (*i.e.,* H_{C_2} is the hour angle of M2 etc.).

From the spherical triangle PSN_1 (Figure 4.1(b)) and using the trigonometric sine and cosine relations the following equations can be derived,

$$\sin(\theta_1)\sin(i_1) = -\sin(H), \tag{4.8}$$

$$\sin(i_1)\cos(\theta_1) = -\sin(\delta_\odot)\cos(H), \tag{4.9}$$

$$\cos(i_1) = \cos(\delta_\odot)\cos(H), \tag{4.10}$$

where H is the difference between hour angle of N_1 and that of sun,

$$i.e.,\ H = H_{N_1} - H_{\odot}.$$

If H_{C_2} is the hour angle of M2 then,

$$H_{C_2} = H_{\odot} + 2(H_{N_1} - H_{\odot}).$$

From the above two equations, the relation for H will be,

$$H = \frac{1}{2}(H_{C_2} - H_{\odot}). \tag{4.11}$$

From Equations 4.8, 4.9 and 4.10, the following relation can be derived,

$$\sin(2\theta_1) = \frac{2\sin(\delta_{\odot})\sin(H)\cos(H)}{\sin^2(H) + \sin^2(\delta_{\odot})\cos^2(H)}, \tag{4.12}$$

$$\cos(2\theta_1) = \frac{\sin^2(\delta_{\odot})\cos^2(H) - \sin^2(H)}{\sin^2(H) + \sin^2(\delta_{\odot})\cos^2(H)}. \tag{4.13}$$

The set of Equations 4.8, 4.9, 4.10 and 4.12, 4.13 allows the calculation of Mueller matrix M1 ($M(i_1)$) and rotation matrix $R(\theta_1)$ for the first mirror. However, the value of H which is related to hour angle of the sun and that of M2, is needed. Looking at the triangle PZC_2 (Figure 4.2(c)), the hour angle of M2 can be obtained using trigonometric relations and is given by,

$$\sin(H_{C_2}) = \frac{\cos(h_{C_2})\sin(A_{C_2})}{\cos(\delta_{\odot})}, \tag{4.14}$$

$$\cos(H_{C_2}) = \frac{\sin(h_{C_2}) + \sin(\phi)\sin(\delta_{\odot})}{\cos(\phi)\cos(\delta_{\odot})}, \tag{4.15}$$

where h_{C_2} and A_{C_2} are the altitude and azimuth of the second mirror of KTT. The altitude and azimuth of M2 can be derived using Figure 4.2 and is given below.

$$\cos(h_{C_2}) = \frac{\sqrt{a^2+b^2}}{\sqrt{a^2+b^2+c^2}}, \tag{4.16}$$

$$\sin(h_{C_2}) = \frac{c}{\sqrt{a^2+b^2+c^2}}, \tag{4.17}$$

$$\cos(A_{C_2}) = \frac{b}{\sqrt{a^2+b^2}}, \tag{4.18}$$

$$\sin(A_{C_2}) = \frac{a}{\sqrt{a^2+b^2}}, \tag{4.19}$$

where 'a' and 'b' are the distances from the center of M1 to that of M2 measured along the east and south respectively. In figure 4.2, M1 is kept towards east of M2. The sign of 'a' is positive if M1 is in east and negative if it is in west. The height from the center of M1 to that of M2 is represented as 'c'. In practice, the value of 'c' and 'a' is fixed at once. The day to day variation of the declination of sun is reflected in the value of 'b'. For a given declination, the value of 'b' is unique so that the light from the first mirror is always reflected into the second mirror. The value of 'b' can be calculated by knowing the declination of sun and the latitude of the place and is given by (Balasubramaniam, Venkatakrishnan, and Bhattacharyya (1985)),

$$b = r_2 \tan(\beta).$$

Where,

$$\begin{aligned} \beta &= A + \sin^{-1}(\frac{\delta_\odot}{B}), \\ A &= \tan^{-1}(\frac{c}{r_2}\tan(\phi)), \\ B &= (\cos^2(\phi) + \sin^2(\phi)(\frac{c}{r_2})^2), \\ r_2 &= (a^2 + c^2)^{1/2} \end{aligned}$$

The angle of incidence at the second mirror can be obtained from the triangle C_1C_2V as,

$$i_2 = \frac{1}{2}(90^\circ - h_{C_2}) \tag{4.20}$$

The spherical triangle SC_2N (Figure 4.1(d)) will give the rotation angle θ_2,

$$\sin(\theta_2) = -\frac{\cos(h_\odot)\sin(A)}{\sin(2i_1)} \tag{4.21}$$

$$\cos(\theta_2) = \frac{\sin(h_{C_2})\cos(2i_1) - \sin(h_\odot)}{\cos(h_{C_2})\sin(2i_1)} \tag{4.22}$$

where $h_\odot$ and h_{C_2} denotes the altitude of the sun and the mirror, M2 respectively. 'A' is the difference between the azimuth of M2 and that of the sun. From Equations

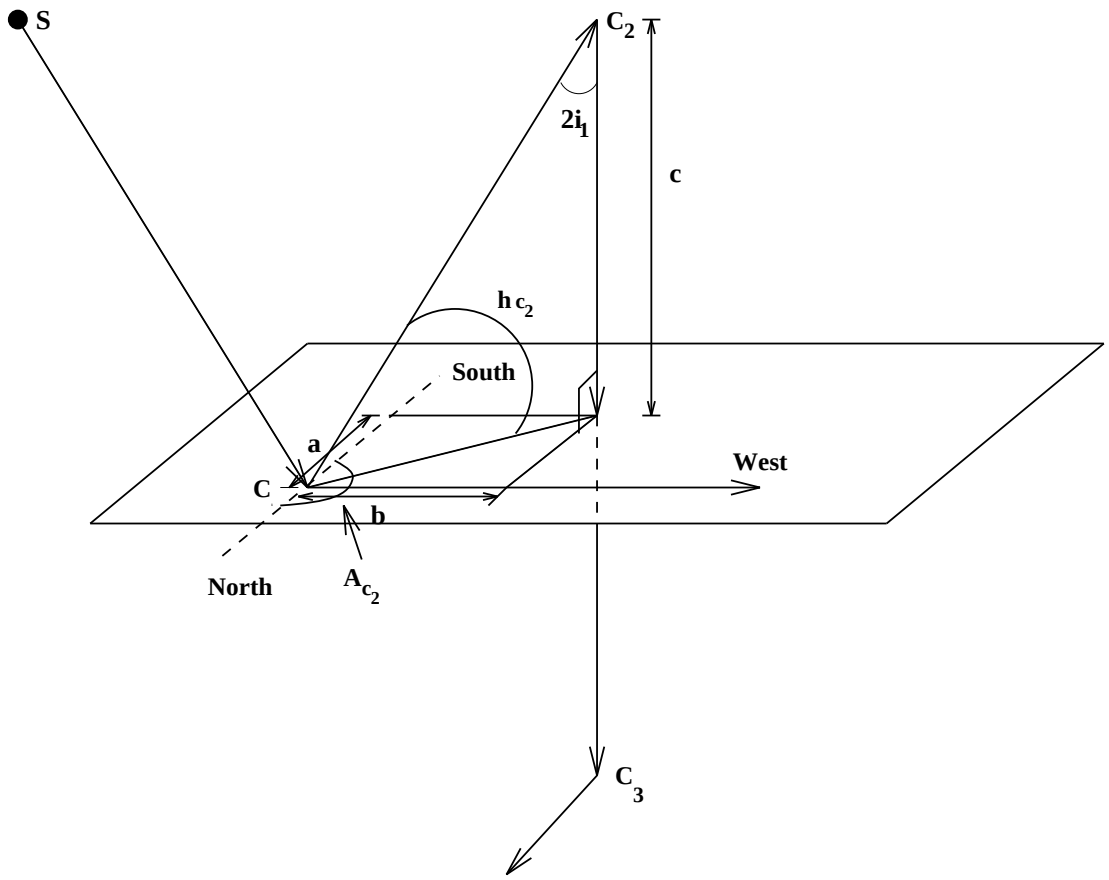

Figure 4.2: The geometrical representation of first two mirrors of the coelostat system (represented as C_1 and C_2). The azimuth and altitude of the second mirror can be calculated from this configuration as described in the text. The values of a, b, and c are measured for the KTT installation and used in the calculation of the instrumental polarisation.

4.20, 4.21 and 4.22, the reflection and the rotation Mueller matrix for M2 can be obtained.

For M3, the angle of incidence is fixed at 45° and the rotation angle θ_3 is given by,

$$\theta_3 = 360^\circ - A_{C_2} \tag{4.23}$$

These two angles are used to find the reflection and the rotation Mueller matrix of M3. The altitude and azimuth of sun can be obtained from its declination and

hour angle. These relations are given by (Green, 1984),

$$\cos(h_\odot)\sin(A_\odot) = \sin(H_\odot)\cos(\delta_\odot) \quad (4.24)$$

$$\cos(h_\odot)\cos(A_\odot) = \cos(\delta_\odot)\cos(H_\odot)\sin(\phi) - \sin(\delta_\odot)\cos(\phi) \quad (4.25)$$

$$\sin(h_\odot) = \cos(\delta_\odot)\cos(H_\odot)\cos(\phi) + \sin(\delta_\odot)\sin(\phi) \quad (4.26)$$

The rotation angle θ_4 is fixed at 45° since the +Q is measured at 45° from the slit direction.

4.3.2 Elements of the Mueller matrix

The complete Mueller matrix 'M' of the system can be obtained using Equation 4.4 by calculating the values of angles of incidence and rotation angle of the plane of reflections. In order to understand the variation of the elements of this combined Mueller matrix, 'M', the values of each element are calculated at different hour angle of the source. These variations are plotted in Figures 4.3 to 4.5. These values are calculated for the day, 16 April 1999. The first mirror was kept in west and hence the value of 'a' is negative. The values for a and c are measured for actual positions of the coelostat mounting and is given in the figure caption. In Figure 4.3, variations of the diagonal elements of the Mueller matrix is plotted. These diagonal elements represent the efficiency of the coelostat system to the input polarised light. Even a 100% input polarised light will be detected as 75% because of these reflections. The variation of these efficiency values over half day of observations is about 0.5%.

Figure 4.4 shows some of the off-diagonal elements which is responsible for the cross-talk from the intensity to the polarisation and *vice versa*, *i.e.,* these elements represent the polarisation and depolarisation produced by KTT. The critical parameters for us is the talk from I to Q, U and V, since the value of I will be atleast an order of magnitude more than that of Q, U and V for a typical measurement of sunspot magnetic field. The talk from I to the linear components Q and U has a typical value of few percent and the variation of these parameters within half day of observation

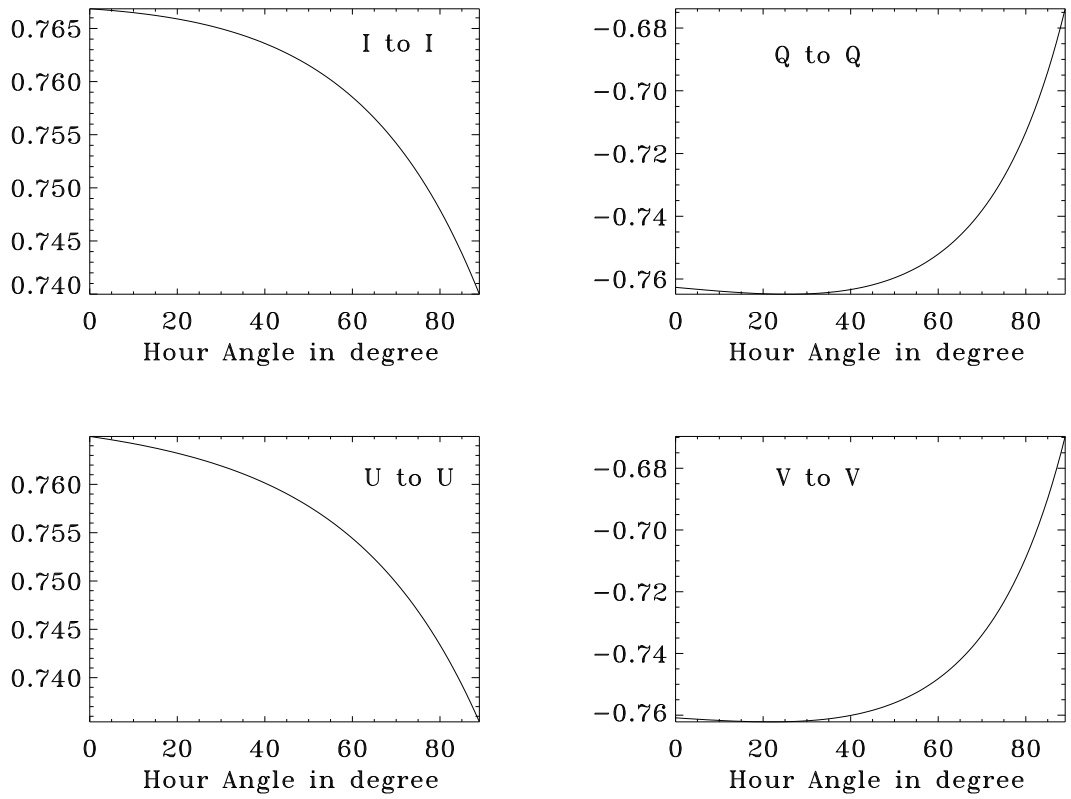

Figure 4.3: The diagonal elements of the Mueller matrix of KTT installation at different hour angle on 16 April 1999. These elements show the efficiency of the instrument to input polarised light and which changes very little with time for that particular day. The values of the positions of M1 are, a = -83 cm, c = 74 cm (see text for the details of a and c)

is also few percent. This is the main reason for calculating the complete Mueller matrix at the particular time of observation, otherwise the inversion of these matrices will have few percent residual error left. However, the talk from I to the circular component V is an order less than that of the linear component which makes the longitudinal magnetic field measurement more accurate than the transverse magnetic field. The main conclusion from Figure 4.4 is that even if the input is unpolarised the coelostat produces linear polarisation of few percent and circular polarisation of about fraction of a percent. If the instantaneous Mueller matrix is not known at the

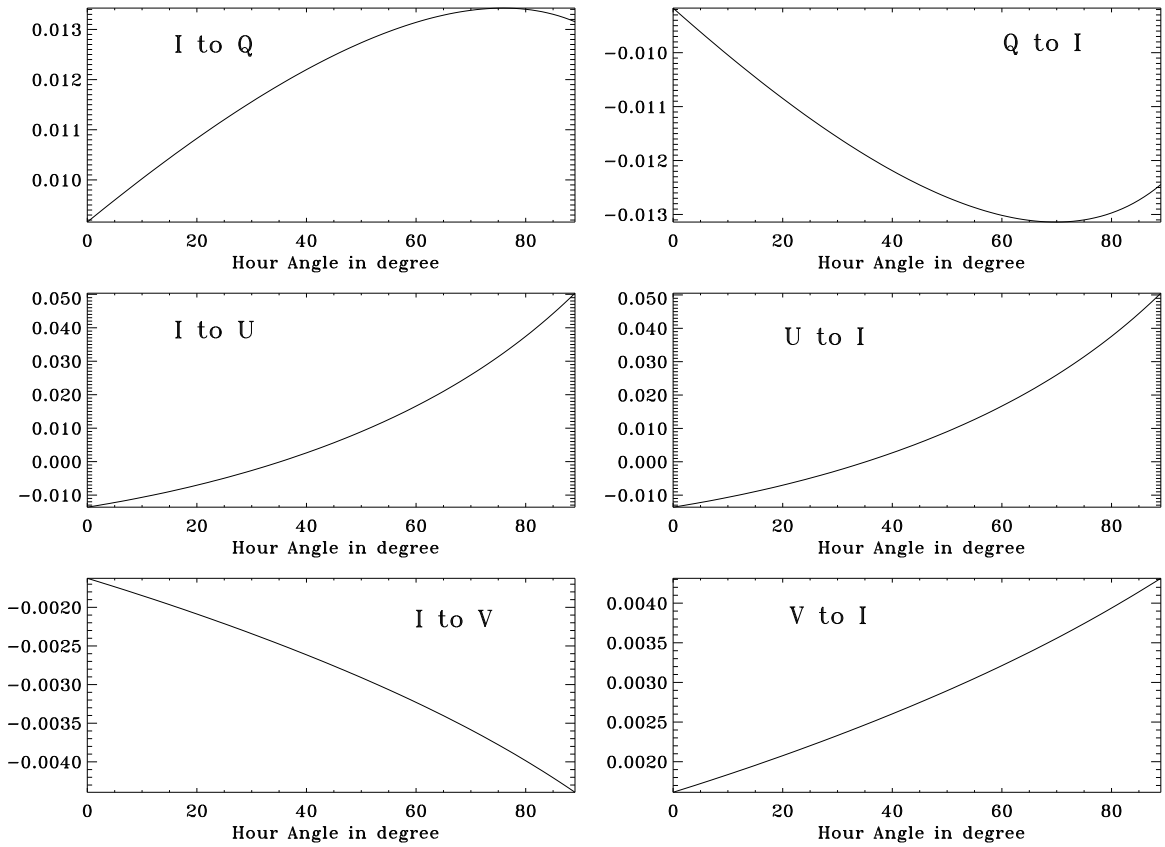

Figure 4.4: The cross-talk (off diagonal) elements of the Mueller matrix of KTT installation at different hour angle on the same day as in Figure 4.3. These elements give the talk from I to Q, U, V and *vice versa*

time of observation and if the inversion is carried out with a Mueller matrix calculated at different time, then the residual error in the inversion will be of few percent.

Figure 4.5 visualises the cross-talk between different states of polarisation. Physically this represents the change in the form of elliptically polarised input to an elliptically polarised output with different ellipticity and orientation. In these plots, the cross-talk varies from few percent to few tens. The major source of cross-talk is from circular to the linear and *vice versa*. These cross-talk too varies about a few percent within half day of observations.

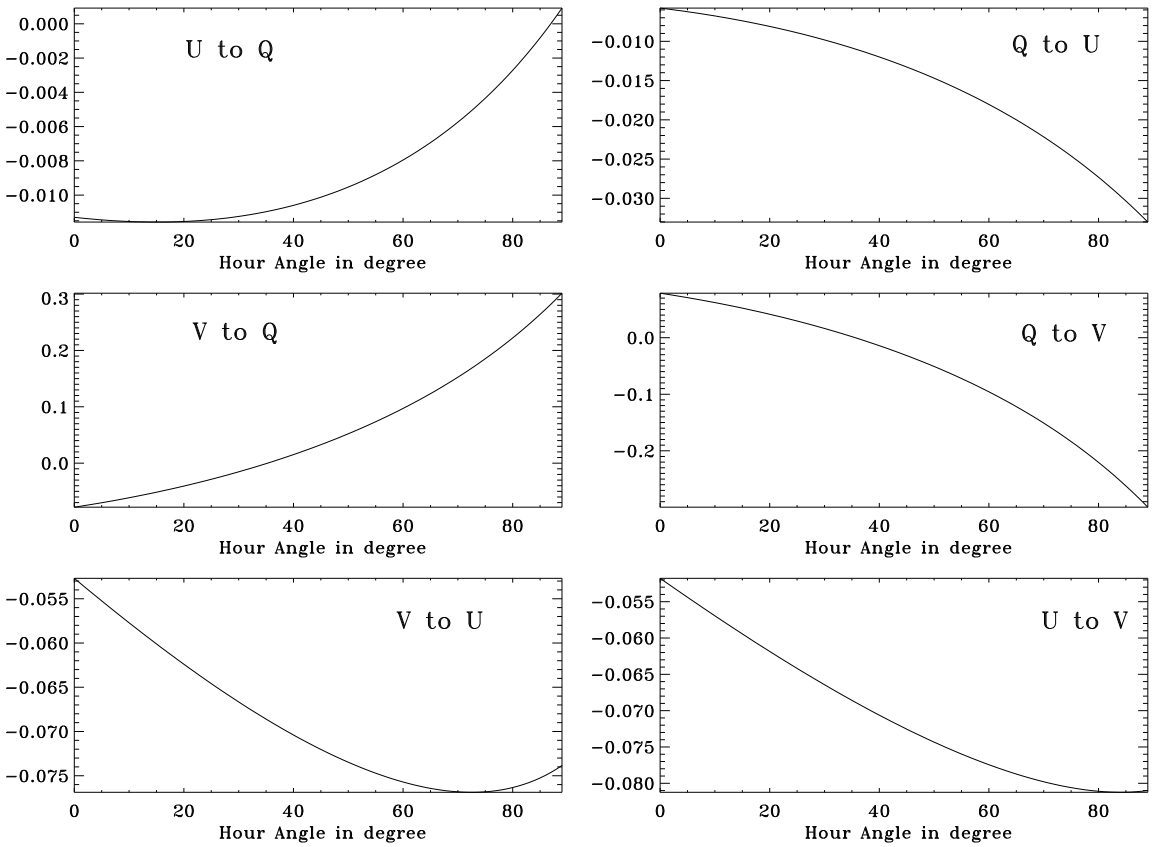

Figure 4.5: The cross-talk (off diagonal) elements of the Mueller matrix of KTT installation at different hour angle on the same day as in Figure 4.3. These elements give the talk between the different polarisation components.

4.4 Measurement & Elimination of Telescope Instrumental Polarisation

In order to test the model in actual observational geometry, the telescope instrumental polarisation is measured by illuminating the telescope with unpolarised light. It is well known that the continuum spectra at disk center of the sun in longer wavelength region is practically unpolarised (Fluri and Stenflo, 1999a). So, the observations are carried out at disk center of the sun around the wavelength 6302Å which is the spectral region of interest for the actual polarisation measurement of sunspot. These observations are carried out during the afternoon of 16 April 1999. About 22

polarisation observations are carried out at different hour angles of the sun.

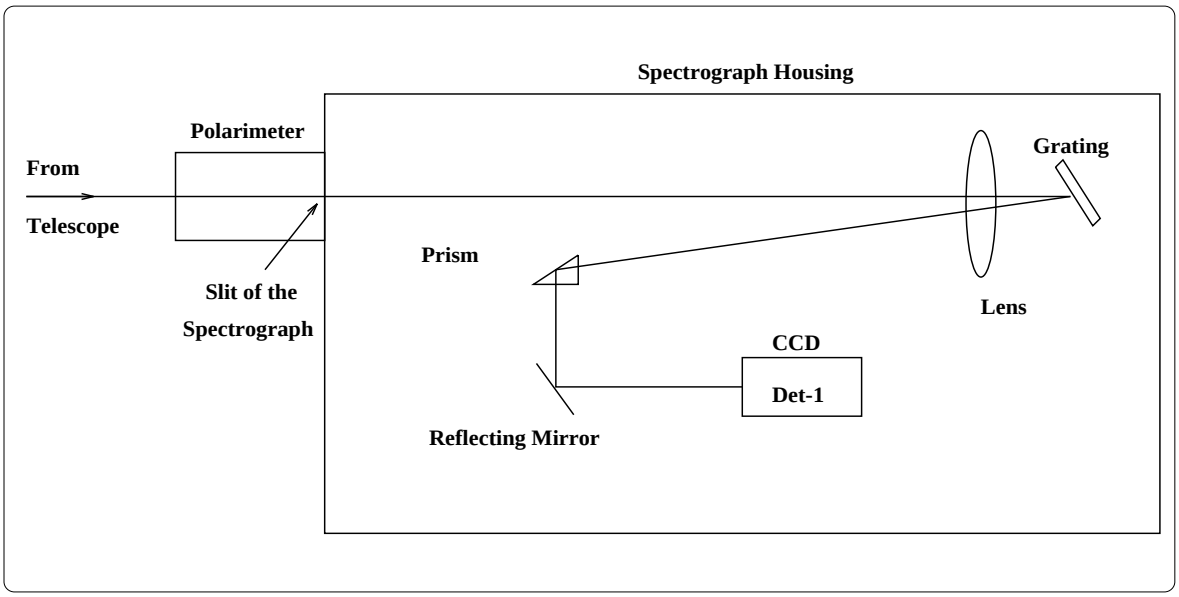

Figure 4.6: The schematic diagram of the optical setup used for the observations.

Figure 4.6 shows a schematic diagram of the observational setup used. The converging beam from the telescope is passed through the polarimeter described in Chapter 3 of this thesis. The image plane of the telescope is the slit plane of the spectrograph. A portion of the suns image is sent through the slit and dispersed using a grating. The spectrum is imaged on to the CCD chip. A portion of the disk center of the sun is used for the measurement of the instrumental polarisation. A region which does not show any activity is chosen so that the polarisation produced at the sun will be very minimum. Figure 4.7 shows the plot of the continuum polarisation variation with local hour angle. The error bars shown are the rms variation of these continuum polarisation values. These are calculated by taking a region of interest containing the continuum wavelength and spatial position. The data points are obtained by taking the mean values of the polarisation in this region. The Mueller matrix derived from the model explained above and the Mueller matrix of the Stokes polarimeter discussed in Chapter 3, is combined to get the overall Mueller matrix of the system. This when combined with the input unpolarised light gives the theoretically expected

continuum polarisation shown as solid line in Figure 4.7. The free parameters used to fit the data with the model, are the real and imaginary part of the refractive indices of the three mirrors of KTT and the thicknesses of the oxide layer formed on these three mirrors. The best fit for the observed continuum polarisation variation will give the optimised value for these free parameters. The free parameters derived from the best fit are, $\eta = 1.31$, $\kappa = 7.80$ and t = 0.0 for all the three mirrors. These observations are carried out just after the realuminisation of all the mirrors and hence we do not expect any formidable oxide layer formed on these mirrors. The value for the refractive index derived matched well with bulk aluminium value. However, the accuracies of these derived values are about few percent since the error bars in these data points are about a percent. These can be improved in the future by improving the polarimetric accuracy.

Since the fit is not exact, the rms deviation will produce a residual error in the calculation of the theoretical Mueller matrix. These residual errors can be found out from the inaccuracies in the fitted parameters. Matrix ΔM given below shows the calculated maximum residual error in the elements of Mueller matrix which when multiplied with uncorrupted Stokes parameters will give the spurious Stokes profiles produced because of these inaccuracies.

$$[\Delta M] = \pm\tfrac{1}{2} \begin{pmatrix} 0.0500 & 0.0040 & 0.0030 & 0.0005 \\ 0.0030 & 0.0015 & 0.0040 & 0.0100 \\ 0.0040 & 0.0500 & 0.0030 & 0.0050 \\ 0.0006 & 0.0050 & 0.0100 & 0.0050 \end{pmatrix},$$

By assuming three different cases with case(i) as Q = 0, U = 0 & V = 20%, case(ii) as Q = 10%, U = 0 & V = 0 and case(iii) as Q = 0, U = 10% & V = 0, the maximum residual errors in the inverted Stokes profiles are calculated. Table 4.1 shows a comparison between the maximum amplitude of spurious Stokes profiles produced without and with instrumental polarisation correction.

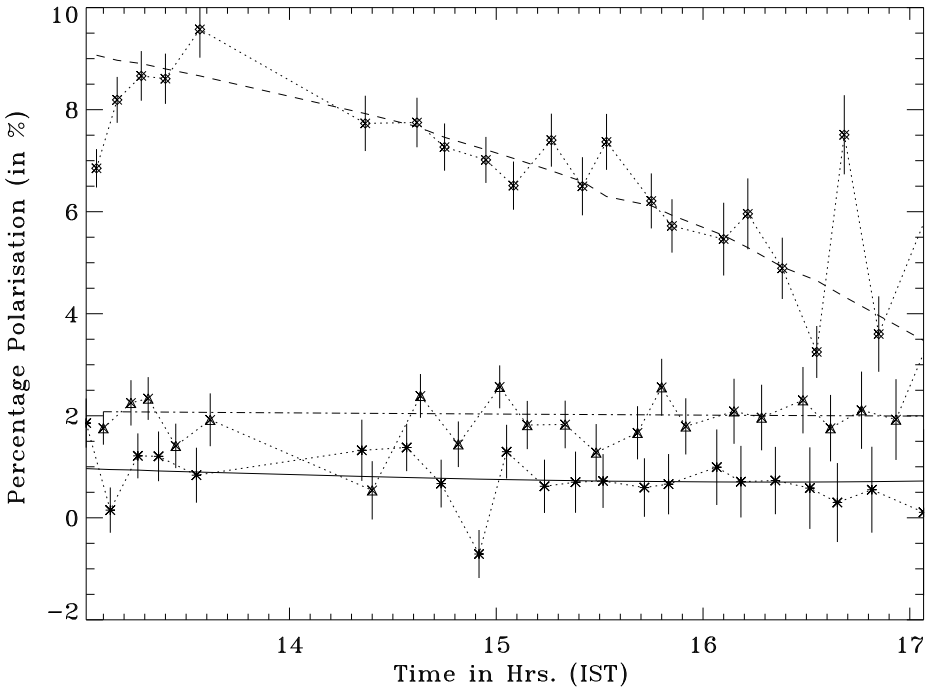

Figure 4.7: The measured polarisation at disk center in the continuum for different observing time given in Indian Standard Time (IST). The asterisk symbol is for Q/I, diamond is for U/I and triangle is for V/I. The solid line is the best-fit model. The refractive index calculated matches well with bulk aluminium value.

Figure 4.8 shows a typical Stokes profiles at a spatial position on the disk center of the sun after correcting for the instrumental polarisation. The rms noise level in Q/I, U/I and V/I Stokes profiles are 0.27%, 0.35% and 0.16% respectively. Figure 4.8 shows only the noise level and there is no Stokes profile signal present as expected since the observations were carried out at a position where visually no magnetic activity was found.

Table 4.1: Comparison of the maximum amplitude of spurious Stokes profiles

Polarisation Mode	Without Instrumental Polarisation Correction	With Instrumental Polarisation Correction
Q	5.4%	0.5%
U	3.6%	0.9%
V	2.8%	0.2%

4.5 Observations of an active region

The observations of an active region sunspot KKL 21263 (NOAA 8516) are carried out at the KTT with the Stokes polarimeter and a Littrow mount spectrograph described in Chapter 3 of this thesis. The observations are done in the morning of 16 April 1999 from 9^{hrs} to 12^{hrs} Indian Standard Time (*i.e.*, UT hours 3:30 to 6:30). Stokes profiles for the well known lines Fe I 6301.5 Å and Fe I 6302.5 Å are recorded. The optical setup used to record these profiles is similar to the one used to record the instrumental polarisation for the continuum wavelength (Figure 4.6). The slit width used is 100μ (0.55 arcsec). The dispersion of the spectrograph is 10.1mÅ per pixel in the second order and the spectral resolution is of 46mÅ which gives a spectral resolving power ($\lambda/\Delta\lambda$) of about 137000. The spatial region covered along the slit direction is about 19 arcsec.

The sunspot is mapped by stepping the image in steps of 5.5 arcsec using the finer movement control of the second mirror. This resolution for the scanning is not good enough to do a mapping of the active region for its full magnetic field configuration. Due to the unavailability of a tracking system, a slit jaw picture and a proper calibration of the image motion, it is not possible to go for a stepping better than 1 arcsec. Currently, a step of 2.75 arcsec (0.5 mm in the image plane) is achieved

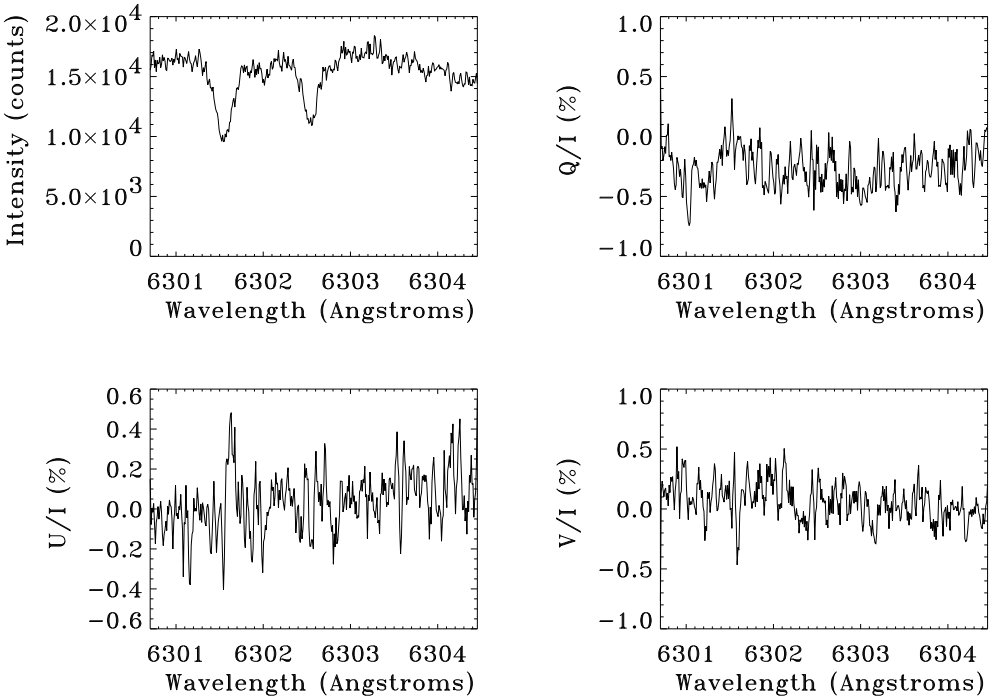

Figure 4.8: A typical Stokes spectral profiles at a spatial position on the disk center of the sun. The rms noise level in the Q/I, U/I and V/I Stokes polarisation profiles are 0.27%, 0.35% and 0.16% respectively

using a scale fixed in the image plane with a least count of 0.5 mm. This scanning is done manually. However, step size of better than 1 arcsec is needed to get the full high resolution (about an arcsec) mapping of active regions. This should be possible in the near future with a slit jaw picture and a spot tracker. The tracking errors for the observations carried out for this thesis is found to be within 1-2 arcsec. However, since the measurements are done using fast chopping, the spurious polarisation signal produced because of this tracking errors will be minimum.

The first mirror was kept in the west during these measurements. Dark, bias and flat-field frames are taken before and after the observations of the sunspot in order to calibrate the CCD for its DC-offset and the pixel to pixel response variations.

4.5.1 Data reduction

The recorded full Stokes profiles of the sunspot KKL 21263 (NOAA 8516) located at N18°E55° are corrected for the dark and bias. The flat field frame is recorded at disk center of the sun without changing any optical configuration. About five flat field frames are taken to make a master flat. The five flat field frames are added together and the master flat is obtained by dividing each row of this added frames with the row averaged spectra in order to remove the spectral lines present in it. The average of the five frames removes most of the spectral line shifts produced by the five minute oscillation present. Finally, the resultant frame is normalised to get a master flat which was then divided from the observed spectra. Similar procedure is done for all the six observations for a single slit position (*i.e.*, $I \pm Q, I \pm U$ & $I \pm V$). All the spectro-polarimetric measurements of a region are done with the same pixel and hence the flat field errors will be eliminated in the parameters Q/I, U/I and V/I.

Figure 4.9 shows a composite intensity picture obtained by choosing a continuum region and combining all the slit & spatial positions. It can be seen that the 5.5 arcsec (a resolution of 11 arcsec) stepping cannot produce a good intensity map of the region. However, in order to get a feel for the region of observation, spectro-polarimetric data obtained with Mees Solar Observatory (MSO) is compared with our observations (Thanks to Prof. Richard Canfield and Prof. Barry LaBonte for the data). The MSO data is obtained on 16 April 1999 during UT hours 16:42 to 18:54 which is 13 hours after our observation. Figure 4.10 shows the intensity map of the region which was observed at MSO. At KTT, before each spectro-polarimetric observation a sketch of the full region with the initial slit position is obtained. This sketch and the intensity image from the MSO is matched to calculate and correct for the rotation between these two images. After the rotation correction is done, the initial and the other slit positions are drawn on the intensity image from the MSO in order to understand the region of observation. In Figure 4.11, the vertical line marked as '1' is the initial slit position of the scanning. The direction of the scan is given as increasing order of the

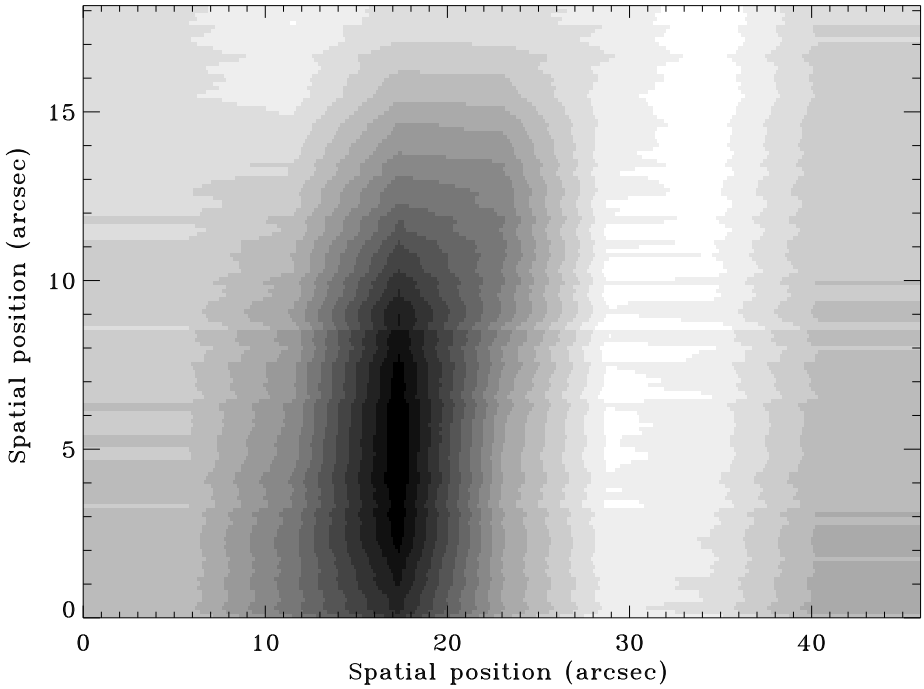

Figure 4.9: Composite intensity image of the sunspot KKL 21263 (NOAA 8516). The image is obtained by combining all the slit and the spatial positions of the region of observations. The scan step used is 5.5 arcsec. The step size along the x-direction is 5.5 arcsec and the y-direction is limited by seeing

slit position (*i.e.*, from 2 to 10). Each slit position is separated by 1 mm in the image plane (5.5 arcsec). The width of the rectangular box marked corresponds to the slit width used for the observation (0.55 arcsec).

The dark, bias and flat field corrected frames are in turn corrected for the instrumental polarisation. The Mueller matrix of KTT is calculated for the time of observation of the Stokes profiles with the refractive index values calculated from the last section. The inverse of this Mueller matrix is multiplied with the observed Stokes profiles in order to get the unmodified profiles. The accuracies in this inversion are 0.5% in Q, 0.9% in U and 0.2% in V. Figure 4.12 shows a typical observed Stokes profiles of a region in the sunspot observed after correcting for the instrumental polarisation.

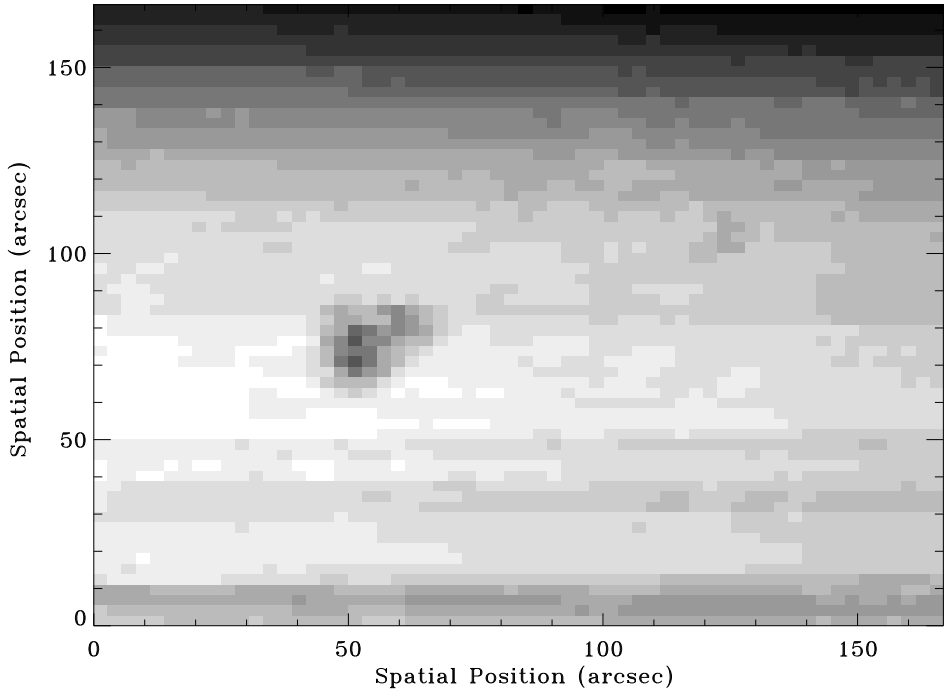

Figure 4.10: Intensity image of the active region sunspot NOAA 8516 (AR 8516) taken with the Stokes polarimeter of the Mees Solar Observatory. This data is obtained from the MSO (Prof. Barry LaBonte and Prof. Richard Canfield) for comparison with our Spectro polarimetric data. The step size along x-direction is 2.828 arcsec and along y-direction is 2.828 arcsec.

4.6 Conclusions

In this chapter, the model for the KTT installation has been developed by modifying the model given by Balasubramaniam, Venkatakrishnan, and Bhattacharyya (1985) to include the initial rotation plane from the solar co-ordinates to celestial co-ordinate. The model developed with the above said modification is very similar to the model developed for the Arcetri solar tower telescope (Capitani *et al.,* 1989). The daily variation of the instrumental polarisation was measured and fitted with the model developed. The free parameters, the real, imaginary part of the refractive indices of the three mirrors of KTT and the thicknesses of the oxide layer on these three mirrors,

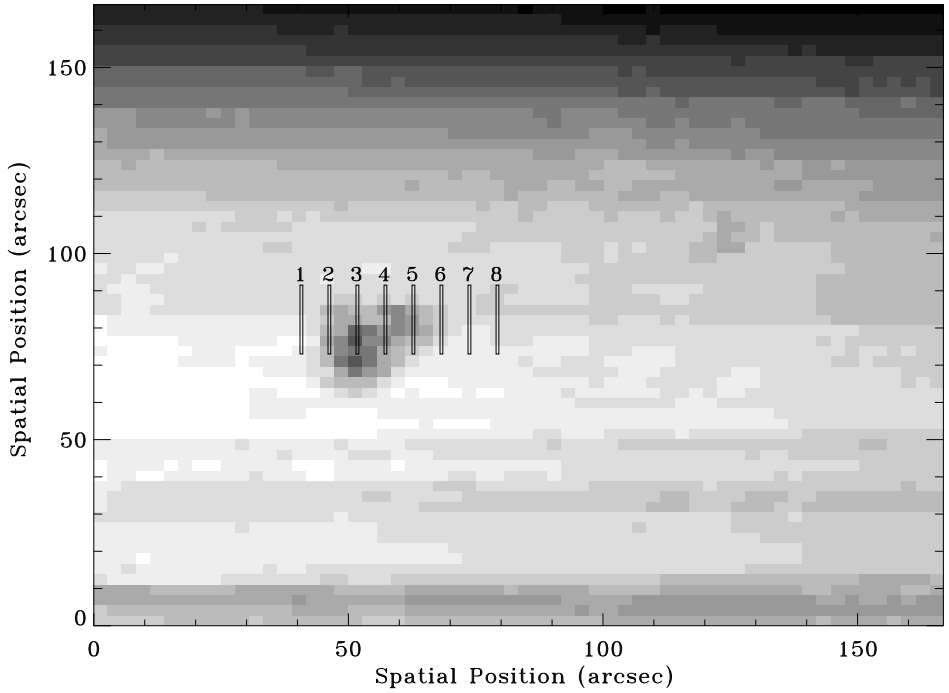

Figure 4.11: Intensity image of the active region sunspot NOAA 8516 (AR 8516) taken with the Stokes polarimeter of the Mees Solar Observatory. The slit positions which are used to take the Stokes profile at the KTT is given. The initial slit position is marked as '1' and the slit is stepped for every 5.5 arcsec and is marked in the figure as increasing number (from 2 to 8).

are found out from the best fit. These three best fit parameters are then used to calculate the Mueller matrix of the coelostat of KTT at any observing time on that day. The inverse of the Mueller matrix is then multiplied with the observed Stokes profiles of an active region (NOAA 8516) in order to get the unmodified Stokes profiles. The uncertainty in the free parameters found out from the fit is used to calculate the spurious polarisation signal produced after the inversion for the instrumental polarisation. It was found that the uncertainty is 0.5% in Q, 0.9% in U and 0.2% in V.

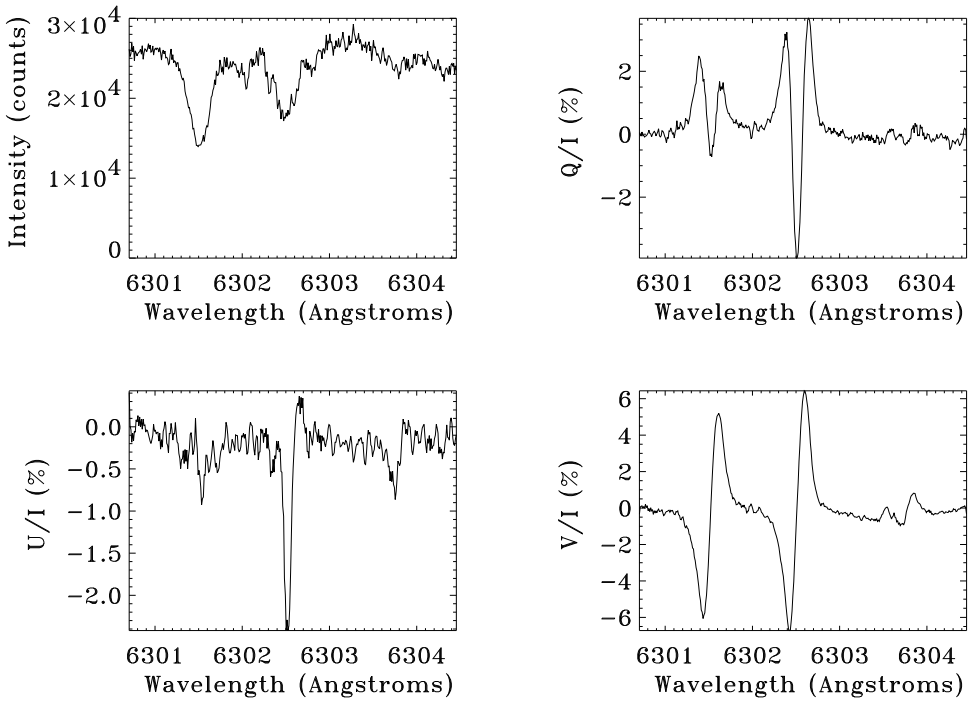

Figure 4.12: A typical Stokes spectral profiles at a spatial position on the sunspot KKL 21263 (NOAA 8516) after correcting for the instrumental polarisation. The accuracies of this inversion are 0.5% in Q, 0.9% in U and 0.2% in V.

Chapter 5

Observation of Sunspot Vector Magnetic Fields

5.1 Summary

The inversion results using the ASP code modified to take the KTT Stokes profile as the input are discussed. The inversion of a bi-polar active region NOAA 8516 was carried out with this code. The total field strength results from this inversion code is compared with the total field strength derived using the Mess Solar Observatory (MSO) Stokes polarimeter and it was found that both agree quite well except for an off-set of about 200 Gauss. The disturbed V-profiles observed near the magnetic neutral line of this bi-polar active region was analysed with a two magnetic component model and was found that flows similar to siphon flow may exist in this region. The vector field map of an active region NOAA 8951 were made and shown.

5.2 Introduction

With the removal of instrumental polarisation of the Kodaikanal Tower Telescope (KTT), it is now possible to obtain vector magnetic field information of any active region on any particular day. As shown in Chapter 4, the residual polarisation left after the removal of the instrumental polarisation is about 0.5%, 0.9% and 0.2% in Q/I, U/I and V/I, respectively. The corrected profiles need to be inverted with an atmospheric model in order to get the physical parameters present in the region of observation. The observational configuration is mentioned in the previous chapter (Section 4.5). The elimination of the instrumental polarisation for these observed Stokes profiles is also mentioned in the same section. In this chapter, we will describe the inversion code which was used to invert the corrected Stokes profiles to obtain the physical parameters like the magnetic field strength, field inclination etc. of the observed region. The code used for inverting the ASP data (Skumanich and Lites, 1987; Lites *et al.,* 1992) is modified in such a way that it can take the Stokes profile observations from KTT and invert it to get the physical parameters in the observed region. The field strength obtained from this inversion is compared with the observations obtained at Mees Solar Observatory (MSO) of the same region in order to look for the consistency in the data. The disturbed peculiar profiles which cannot be inverted using the ASP code is fitted using a two magnetic component model. The results obtained from this fit is also discussed. The vector field map of a sunspot is given.

5.3 Inversion of Stokes Profiles

The calculation of the physical parameters particularly the vector magnetic field from the Stokes profile observations require the solution of the Radiative Transfer Equations (RTE) (del Toro Iniesta and Ruiz Cobo, 1996a). The solar atmosphere is repre-

sented through a set of model parameters assumed to describe completely the physical state of the system. These parameters are not directly measurable but do determine the values of the observables, in this case the Stokes profiles, $[I_\lambda, Q_\lambda, U_\lambda, V_\lambda]^T$. Two ways are possible to determine these model parameters, one is called as *forward problem* and the other is *inverse problem.*

The *forward problem* consists in predicting the values of the unknown Stokes pseudo vector (del Toro Iniesta and Ruiz Cobo, 1996b) by solving the RTE which are linear differential equations under the Milne-Eddington (ME) approximations. For producing the Stokes vector, arbitrary values of the model parameters are chosen. The arbitrariness in the value of the model parameters is not really arbitrary in the sense that the approximate values are obtained from the observed Stokes vector. For example, the field strength can be found out from the splitting if the line is completely split or from the magnitude of the circular polarisation. However, to get a consistent solution, the *forward problem* requires enormous computation time once the number of parameters required to specify the state of the atmosphere becomes large.

The *inverse problem* does infer the unknown model parameters from the observed Stokes profiles. In a wider sense, any inference made of a given solar parameter might be called as an inversion. For example, the classical estimation of line-of-sight velocity from the position of the line core minimum would be an inversion. In this particular example, the model atmosphere would simply consists of a constant material velocity with height. No other solar physical quantity is assumed to alter the observed line core position. When a more detailed description is sought, careful account for the many non-linear dependence of the observed spectra on the various atmospheric parameters is needed (Ruiz Cobo & del Toro Iniesta, 1994; Bellot Rubio, Ruiz Cobo and Collados, 2000). If the dependence of the Stokes vector on the various atmospheric parameters like thermodynamic, dynamic, magnetic parameters is linear, then an analytic inversion of the problem would be taken for granted. It is the non-linearities which require the use of involved numerical techniques. We used only the analytic in-

version (Skumanich and Lites, 1987; Ruiz Cobo, 1992) for the observations described in this thesis. Refer to del Toro Iniesta and Ruiz Cobo (1996b) for the numerical inversion techniques to include the non-linearities in the physical parameters. With the advent of numerous minimisation techniques, it is now possible to use the inversion code efficiently for a large amount of data with a large number of unknown free parameters.

5.4 Methodology

The inversion methodology used here is the same as that of the one used at High Altitude Observatory (HAO) for the Advanced Stokes Polarimeter (ASP) data. This methodology is described by Skumanich & Lites (1987), Lites & Skumanich (1990), Skumanich, Grossmann-Doerth, and Lites (1992) and Skumanich, Lites, and Martinez Pillet (1994) and references therein. The methodology involves the solution of the RTE's in a model atmosphere. Using classical approach, Jeffries, Lites, and Skumanich (1989) solved the transfer equations for the spectral line radiation in a dielectric medium permeated by a magnetic field and their solution is given by,

$$\frac{d\mathbf{I}}{dz} = -\mathbf{K_t}\mathbf{I} + \mathbf{J}. \tag{5.1}$$

Where, $\mathbf{I} = [I, Q, U, V]^T$ and $\mathbf{J} = \mathbf{K}_t[S, 0, 0, 0]^T$. $\mathbf{K}_t$ is the 4×4 absorption matrix which characterise the effects of magnetic field and other physical parameters on the atom,

$$[\mathbf{K_t}] = \begin{pmatrix} \kappa_I + \kappa_c & \kappa_Q & \kappa_U & \kappa_V \\ \kappa_Q & \kappa_I + \kappa_c & \kappa'_V & -\kappa'_U \\ \kappa_U & -\kappa'_V & \kappa_I + \kappa_c & \kappa'_Q \\ \kappa_V & \kappa'_U & -\kappa'_Q & \kappa_I + \kappa_c \end{pmatrix},$$

with,

$$\begin{aligned}
\kappa_I &= \frac{1}{2}[(\frac{\kappa_r+\kappa_l}{2})(1+\cos^2(\gamma))+\kappa_p\sin^2(\gamma)] \\
\kappa_Q &= \frac{1}{2}(\kappa_p-\frac{\kappa_r+\kappa_l}{2})\sin^2(\gamma)\cos(2\chi) \\
\kappa_U &= \frac{1}{2}(\kappa_p-\frac{\kappa_r+\kappa_l}{2})\sin^2(\gamma)\sin(2\chi) \\
\kappa_V &= \frac{\kappa_r-\kappa_l}{2}\cos(\gamma) \\
\kappa'_Q &= \frac{1}{2}(\kappa'_p-\frac{\kappa'_r+\kappa'_l}{2})\sin^2(\gamma)\cos(2\chi) \\
\kappa'_U &= \frac{1}{2}(\kappa'_p-\frac{\kappa'_r+\kappa'_l}{2})\sin^2(\gamma)\sin(2\chi) \\
\kappa'_V &= \frac{\kappa'_r-\kappa'_l}{2}\cos(\gamma)
\end{aligned}$$

The $\kappa_I,\ \kappa_Q,\ \kappa_U$ and κ_V are called as absorption coefficients whereas $\kappa'_Q,\ \kappa'_U,\ \kappa'_V$ are called magneto-optical coefficients. The absorption arises because of the resonant absorption when an electric field incident on a classical dielectric. The magneto-optical effect arises because of the differential absorption of the dielectric to the two orthogonal electric field vibrations (one along the vibration axis of the dielectric and the other perpendicular to it). This produces a phase-change and hence a birefringence. γ is the angle made by the magnetic field with the line-of-sight and χ is the azimuthal angle of the magnetic field vector. The physical parameters of the medium, like the temperature, velocity etc., are represented via the absorption and the magneto-optic coefficients.

In the classical approach, the atom represented as a dielectric is resolved into three normal polarisation modes in the presence of a magnetic field. The absorption coefficients for these three modes are given here as κ_p, κ_r and κ_l. They are in turn related to the basic physical properties of the dielectric medium and to the applied magnetic field strength,

$$\begin{aligned}
\kappa'(v) &= \frac{\pi Ne^2}{mc}\frac{1}{\sqrt{\pi}\Delta\nu_D}2F(a,v), \\
\kappa(v) &= \frac{\pi Ne^2}{mc}\frac{1}{\sqrt{\pi}\Delta\nu_D}H(a,v).
\end{aligned}$$

$\Delta\nu_D$ is the Doppler width (representing the thermal properties of the atmosphere in Local Thermodynamic Equilibrium (LTE)) and $a = \Gamma/4\pi\Delta\nu_D$, the damping factor (representation of micro and macro turbulence). In classical analogy, 'a' is the damping factor for the damped classical oscillator or the dielectric. H(a,v) is the Voigt profile and F(a,v) can be represented using the Voigt profile and they are given as,

$$\begin{aligned} H(a,v) &= \frac{1}{\pi}\int \frac{(v-y)e^{-y^2}dy}{(v-y)^2+a^2} \\ 2F(a,v) &= \frac{a}{\pi}\int \frac{e^{-y^2}dy}{(v-y)^2+a^2}. \end{aligned}$$

The dimensionless variable 'v' is equal to $(\nu_0 - \nu)/\Delta\nu_D$ for the unshifted plane-polarised component (κ_p, κ'_p) while for the circular polarised pair $(\kappa_r, \kappa_l, \kappa'_r, \kappa'_l)$, it is given as,

$$v = \frac{(\nu_0 \mp \nu_L - \nu)}{\Delta\nu_D}$$

ν_L is the Larmor frequency whose value is decided by the field strength and atomic parameters.

In this methodology, the thermal, magnetic and dynamic state along the observed line-of-sight (LOS) is represented by the lowest order variation or representation possible. Thus all atmospheric parameters are considered to be constant along the LOS except for the line source function, S which is represented as a linear function of continuum optical path along the LOS,

$$i.e.,\ S = B'_0 + B'_1\tau_c, \tag{5.2}$$

with $B'_1 = \beta\mu$ for plane parallel atmosphere (β represents the vertical gradient). Such an approximation was studied by Holt (1972) in the field free situation and shown to yield physically meaningful results. In the case of Fe I lines used by us and ASP, Bruls, Lites, and Murphy (1991) has shown that this low order approximation is a good description of realistic solar conditions.

These approximations lead to a Milne-Eddington (ME) atmosphere and hence the polarised radiative transfer equation for the emerged Stokes vector is studied for the

ME atmosphere. The emergent Stokes vector in the ME atmosphere can be written as (Skumanich, Lites, and Seagraves, 1997),

$$I_\lambda = B_0' u + B_1' (\hat{1} + \eta_0 \hat{\phi_\lambda})^{-1} u. \tag{5.3}$$

Where I_λ is the emergent Stokes vector ($[I_\lambda, Q_\lambda, U_\lambda, V_\lambda]^T$) and u is the unpolarised Stokes vector representing the unpolarised light ($[1,0,0,0]^T$), $\eta_0 = \kappa_{00}/\kappa_c$ where κ_{00}H(a,0), κ_c are the line center & continuum opacity respectively with H(a,$\Delta\lambda$), Voigt function. $\hat{\kappa_\lambda} = \kappa_{00}\hat{\phi_\lambda}(B, \psi, \phi, \Delta\lambda_D, a, \lambda_0^m)$ is the absorption matrix. The above equation depends non-linearly on the magnetic field strength B, inclination angle ψ to the LOS and the azimuthal angle ϕ in the observers frame. Also, it depends non-linearly on the Doppler width $\Delta\lambda_D$, damping factor a($=\Gamma/4\pi\Delta\lambda_D$) and line center position λ_0^m (LOS measure). Thus, nine atmospheric parameters,

$$viz.,\ p = (B, \psi, \phi, \eta_0, \Delta\lambda_D, a, \lambda_0^m, B_0', B_1')$$

determines the emergent vector.

In fitting this model to the data an inconsistency between the source function coefficient B_1' appearing in the polarisation parameters, $Q_\lambda, U_\lambda, V_\lambda$ and that in the intensity parameter, I_λ has been included. This inconsistency is due to varieties of causes. It may be because of the scattered light or the lack of spatial resolution where a non-magnetic region is included in a pixel resolution or to the effects such as canopy condition (Skumanich, Grossmann-Doerth, and Lites, 1992). To reduce the number of unknowns, the fill factor is incorporated into the source function parameter without any loss of generality.

The HAO code differs from the AHH routine in incorporating the magneto-optical effect, taking the gradient of the source function B_1' as a free parameter and including the damping parameter 'a'. This allows the intensity profile to decouple from the polarisation profiles and hence an option of fitting any weighted combination of the four Stokes profiles. When the polarisation profiles are fitted by themselves (zero weight for I_λ), B_1' is determined solely from the magnetic regions in the field of view

that contribute to the polarisation. When I-profile is included in the fit, an optional additional parameter, 'f', representing scattered light and fill factor is included.

It is essential to have a good initial guess for any least squares regression analysis. For line center, the equivalent width bi-sector is used as a first approximation. The central depth of the I-profile provides an estimate of B_1', and for $\Delta\lambda_D$, a and η_0, a starting value of 25mÅ, 0.2 and 3 is used respectively. The fractional contribution of the stray light profile, 'f' is initiated with a value zero. If the magnetic field is strong enough to produce a splitting in the I-profile, the separation of these split features provides an initial estimate of the magnetic field strength. If no splitting is observed an initial value of 500 G is adopted.

The inversion code tested for the ASP data, is modified to take the input Stokes spectra from KTT rather than the ASP data. The main disadvantage of this inversion code is that it cannot reproduce any asymmetries which are observed in the Stokes profiles. Also, peculiar profiles observed in the sunspot, particularly in the penumbral region cannot be reproduced. To reproduce such profiles, the gradients in the physical parameters need to be included in the atmospheric model and also the atmosphere should include three or more components rather than the two component model (one magnetic and the other non-magnetic).

5.5 Inversion Results

The ASP inversion code was run with the Stokes profile data for the KTT polarimeter. The results of the ASP inversion is the output of nine physical parameters at each point on the spatial position along the slit as well as at different slit positions used. The nine physical parameters derived are, (i) The magnetic field strength, B, (ii) Magnetic field inclination from the line of sight (LOS), ψ, (iii) Azimuthal angle of the magnetic field vector, χ, (iv) LOS velocity represented as the line core position, λ_o^m, (v) Line depth, η_0, (vi) Doppler width, $\Delta\lambda_D$, (vii) Damping factor, a, (viii)

Constant background source function, B_0, (ix) The slope of the source function, B_1. The tenth parameter, scattered light 'f' is taken as another parameter if the inversion includes the total intensity. The ASP code also derives the errors in each of the fitted parameters.

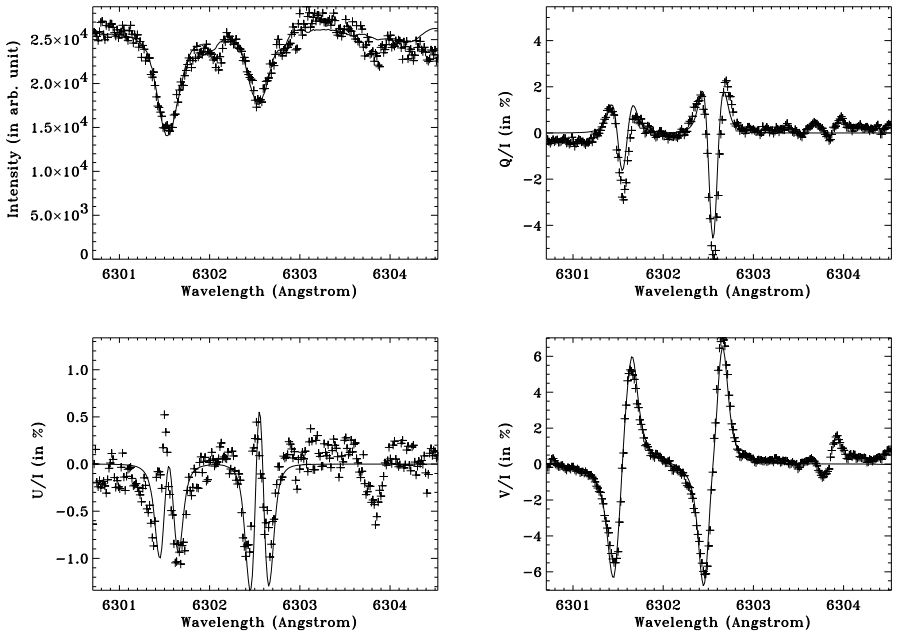

Figure 5.1: The four Stokes profiles of a spatial position which showed significant signals in all the profiles in the active region NOAA 8516. The data points are marked as '+' and the solid line is the best fit.

Figure 5.1 shows a typical fit of the Stokes profiles with the ME atmospheric model. The Stokes profiles were taken from a point in a region where all the Stokes profiles showed considerable signal for the active region NOAA 8516. The fit is reasonably good. The excess scatter in the U-fit originates due to the low signal to noise level compared to Q and V. This is because of the extra polaroid inserted during U-measurement. While fitting, instead of using the whole wavelength region of observations, a band of data points around the line $\lambda\lambda$6301.5Å and $\lambda\lambda$6302.5Å are used to fit in order to reduce the noise level in the fit. Table 5.1 lists the atomic parameters of these lines (Sigwarth *et al.,* 1999). Table 5.2 lists the observational

parameters for the active region NOAA 8516. This line is used extensively for the magnetic field measurement since the atomic parameters are very similar for these two lines except for the difference in the Lande 'g' factor which characterises the sensitivity of the line to the magnetic field. The line 6302.5Å has a larger Lande factor compared to the line 6301.5Å.

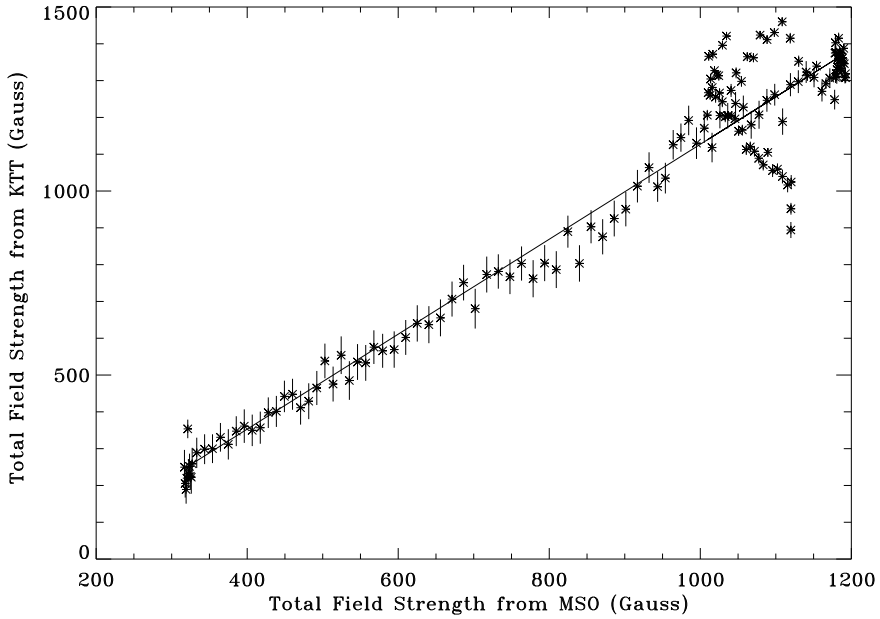

Figure 5.2: A plot between the total field strength obtained with the MSO and with the KTT. The results agree reasonably well except for an offset of about 200 Gauss.

The total field strength calculated using the ASP inversion for the active region NOAA 8516 is compared with the results from the Mees Solar Observatory (MSO). The slit positions used for the observation is marked in the Figure 4.11. Figure 5.2 shows the plot between the total field strength obtained using the MSO stokes polarimeter and the KTT Stokes polarimeter. It can be seen that both the results are agreeing quiet well with a small off-set value of about 200 G. Figure 5.3 shows a typical vector field results for the slit position '4' (See Figure 4.11) from this inversion code. This figure shows that the total field strength, LOS inclination in the observers co-ordinate and the azimuthal angle of the field. These three quantities

Table 5.1: The atomic parameters for the line $\lambda\lambda$6301.5Å and $\lambda\lambda$6302.5Å.

Species	Wavelength in Å	Lande factor	Excitation Potential Low	High	Mult. No.
Fe I	6301.5091	1.5	3.64	5.60	816
Atm.O_2	6302.0005				
Fe I	6302.5017	2.5	3.67	5.63	816
Atm.O_2	6302.7629				

specify the vector field of the magnetic region. The errors in the derived parameter are shown as the error bars with the length of the error bar equal to three times the error derived from the fit (*i.e.,* 3σ). The ambiguity of 180° present in the azimuth measurement is removed manually by looking at the spurious jumps present. This ambiguity arises because the transverse Zeeman effect is insensitive to the 180° changes in the azimuthal orientation of the magnetic field vector.

5.6 Peculiar Profiles around Magnetic Neutral Line

The Stokes profile observations done for the active region NOAA 8516 showed peculiar V-profiles. Figure 4.11 shows the slit positions used to observe the region with the polarimeter at KTT. Figure 5.4 shows the same region but the gray scale image is the line of sight field map taken using the MSO Stokes polarimeter.

The sunspot NOAA 8516 is a bipolar region as seen in the MSO line of sight magnetic field map (Gray image in Figure 5.4). The negative and positive polarity is mapped as dark and bright respectively. It can be seen from Figure 5.4 that the slit position marked '5' crosses the neutral line region. Magnetic neutral line is a region where the field is fully transverse. However, if there are flows present in those regions, the cancelation of the V profiles from adjacent regions is not exact and can

Table 5.2: Observational parameters of the spectrograph, the Stokes polarimeter and the active region NOAA 8516.

Spectral Range covered:	6300.70 to 6304.44Å.
Spectral Resolution :	137 000 at 6302Å.
Dispersion:	10.1mÅ per pixel.
Spatial Scale:	0.121 arcsec per pixel.
Slit Width:	0.55 arcsec.
Step Width:	5.5 arcsec.
Integration Time:	1 sec to 5 sec.
	(100 msec chopping)
First Mirror Position:	West.
Field of View :	44.0×34.0 arcsec^2
Date of Observation:	16 April 1999.
Time in UT hours:	03:30Hrs.
Active region :	NOAA 8516.
Position on the sun:	S18°E52°.

produce peculiar V-profiles. This can be used as a sensitive diagnostic of the line-of-sight velocity difference between the opposite polarity regions (Skumanich and Lites, 1991). Figure 5.5 shows the line-of-sight magnetic field strength (longitudinal field strength) along the slit position number '5'. The line-of-sight field was calculated using the results from the ASP code modified to take the KTT Stokes profiles as input. The result of the total field strength and the line-of-sight angle derived with the ASP code is used to calculate the line-of-sight field strength using the relation,

$$B_{lon} = B_{tot}.cos(\psi) \tag{5.4}$$

where B_{lon} is the longitudinal field strength and B_{tot} is the total field strength. ψ is the line-of-sight inclination of the magnetic field vector in the observers co-ordinate.

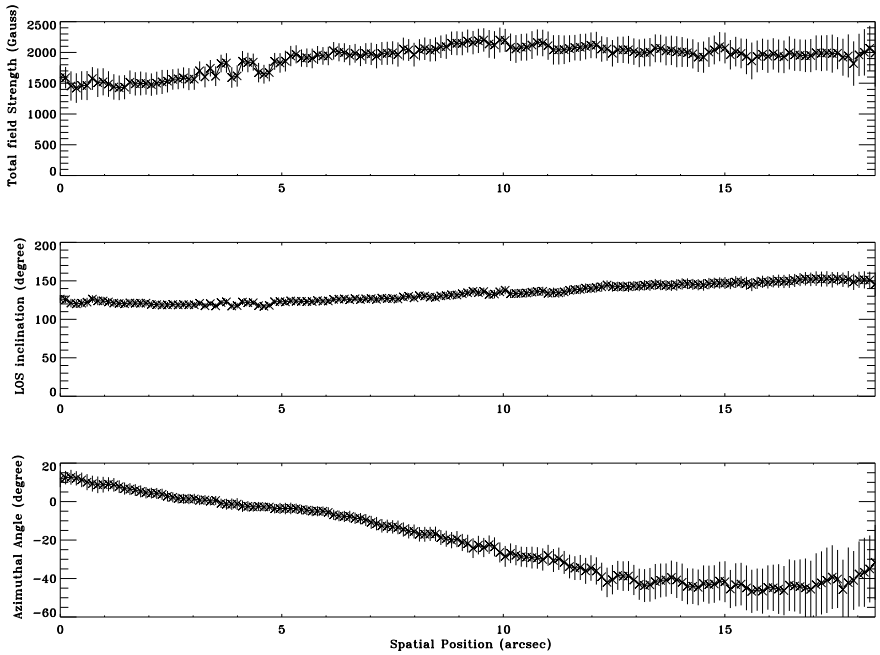

Figure 5.3: Vector field calculated using the ASP code along the slit position marked as '4' in the Figure 4.11. The error bars for the derived parameters are plotted. The length of the error bar is equal to three times the error value derived from the inversion code.

It can be seen from this figure that two opposite polarity regions exist within the field of view and Figure 5.6 shows the total field strength along the same slit position.

By comparing these two figures (Figure 5.5 and 5.6), it can be seen that the positive polarity has slightly more field strength than the negative polarity near the neutral line. Along the neutral line, the magnetic flux of positive and negative polarity cancels each other if there are no other dynamics involved like the velocity etc. An examination of the Stokes profile around the neutral line indicated that the V-profiles were disturbed and showed multiple reversal. A simple two magnetic component model is generated by taking the profile from the positive and negative polarity (pixel position 11 for the positive polarity and pixel position 103 for the negative polarity). The neutral line lies around the pixel position 76. From the positive and negative polarity profile, a composite profile was made using two free parameters, one is the

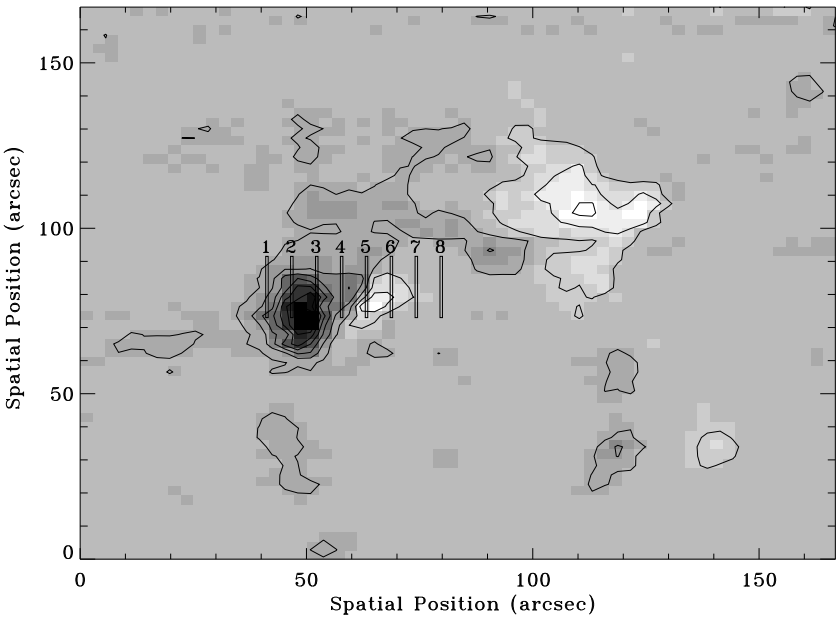

Figure 5.4: The observed slit position over plotted on the line-of-sight magnetic field observed using the MSO Stokes Polarimeter. This active region NOAA 8516 is bipolar as seen in the figure and the slit position number '5' passes through the neutral line region.

fill factor, 'f' and the other is the relative velocity, '$\Delta\lambda_v$'. The composite profile is represented as,

$$CP(\lambda) = f.P_1(\lambda) + (1 - f).P_2(\lambda - \Delta\lambda_v).$$

Where, CP(λ) represents the composite profile. P_1 and P_2 refers to the positive and negative polarity profile respectively and 'f' is the fill factor which represents the weightage of these two profiles in the composite profile. By varying 'f' and $\Delta\lambda_v$, the observed profile near the neutral line (pixel number 76) is fitted. Figure 5.7 shows a typical profile near the neutral line and the best fit using the composite profile. About eight profiles around the neutral line is fitted with the above composite profile equation. Table 5.2 lists the results of these fittings.

A fill fraction of 0.8 means the weight for the positive polarity (profile 1) is 80%

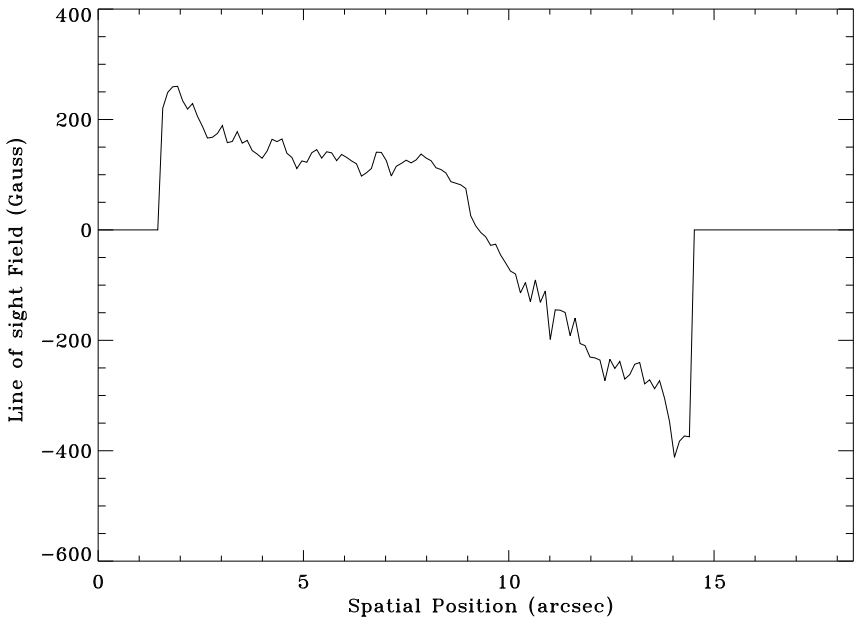

Figure 5.5: The line-of-sight magnetic field strength calculated using the ASP inversion code along the slit position '5'. The polarity reversal is clearly seen in this picture.

in the composite profile and for the negative polarity (profile 2), it is 20%. It can be seen from Table 5.2 that the results for the velocity is mostly negative around the neutral line. This means that the profile 2 is shifted towards blue compared to the profile 1. Hence, the flow in the negative polarity is towards the observer (upflow) compared to the flow in the positive polarity. It has been observed that there are flows in the outer edges of sunspots (Evershed, 1909). These flows starts in the penumbral region. The end points of these flows are shown to be in the photosphere around the active region or the sunspot (Westendorp Plaza *et al.,* 1997a). The possibility of this Evershed flow as siphon flow is also been studied (Montesinos and Thomas, 1997). Siphon flow occurs along a magnetic flux tube. The flow will occur only when there is a field difference between the two foot points of the magnetic flux tube. The flow goes from the foot point which has lower field strength to the higher field strength

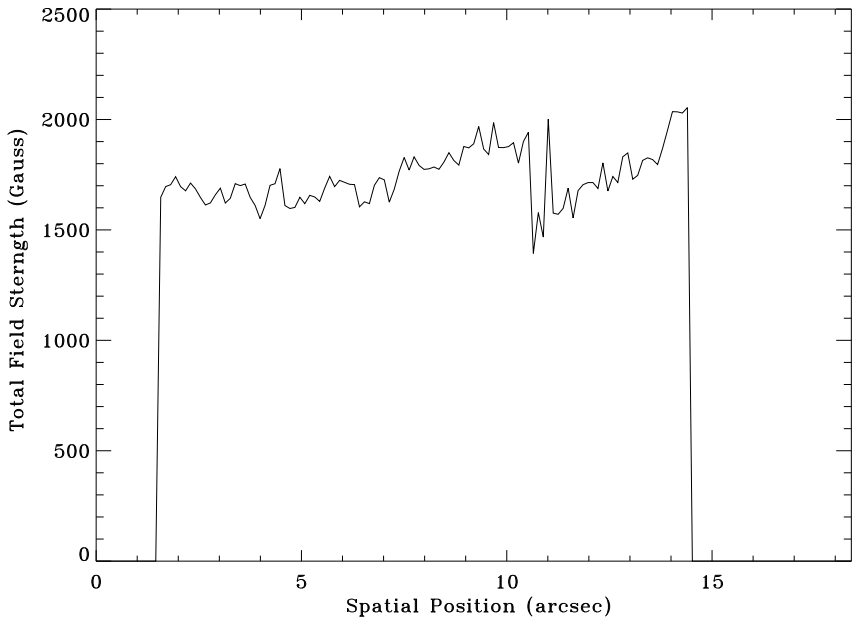

Figure 5.6: Total field strength calculated using the ASP code modified to take the KTT Stokes profiles along the slit position marked as '5'. By comparing with the Figure 5.5, it can be said that the total field strength in the negative polarity (field lines going away from the observer) is less than in the positive polarity (field lines pointing towards the observer).

foot point. The pressure balance equation for a bi-polar region can be written as,

$$P^{+}_{gas} + \frac{B^2_{+}}{8\pi} = P^{-}_{gas} + \frac{B^2_{-}}{8\pi},$$

where, P^{+}_{gas} and B_{+} represents the gas pressure and the total magnetic field strength respectively. The '+' sign refers to the positive polarity. Similarly, P^{-}_{gas} and B_{-} refers to the gas pressure and total field strength for the negative polarity. It can be seen that the gas pressure will be higher in the low field strength foot point compared to the high field strength foot point and hence a flow from the low field strength foot point to the high field strength foot point, is expected. However, the observed Evershed effect is from the penumbral region to the photosphere and observationally the photosphere around a sunspot has less field strength compared to the penumbral region and hence

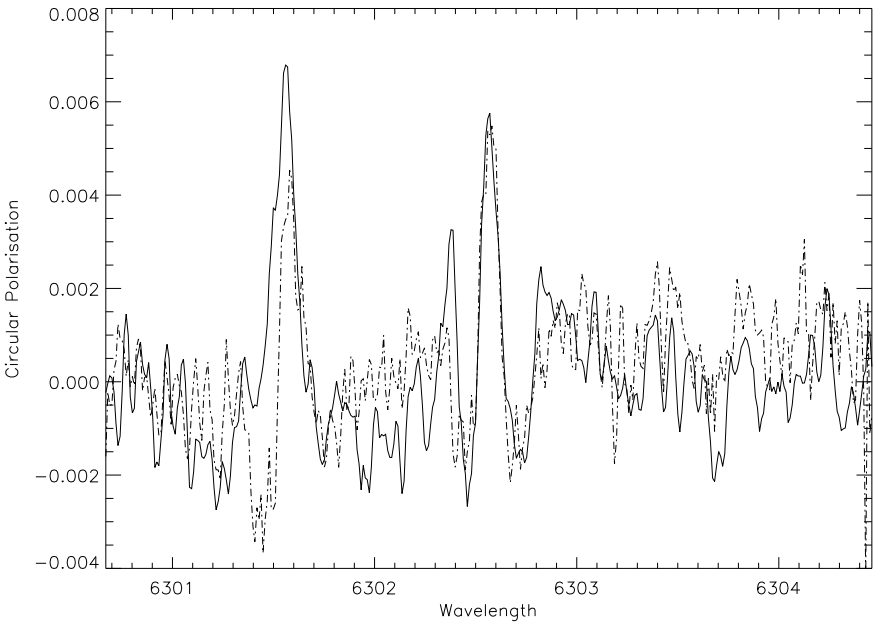

Figure 5.7: A typical observed disturbed V-profile around the neutral line shown as solid line and the best fit using the composite profile shown as dashed line.

the flow was expected from the photosphere to the penumbral region, if the flow is a siphon flow. However, this difference can be attributed to the difference in the atmospheric height for the photosphere and the penumbral region. In the penumbra the observed profile originates from the deeper layer compared to the photosphere and hence the reduction in the field strength in the photosphere (Montesinos and Thomas, 1997). In the case of a bi-polar region, the observed height on the atmosphere will be approximately same if the field strength of these two regions are similar.

From the Table 5.2, the flow seems to be from the negative polarity to the positive polarity and from Figure 5.5 and 5.6, it can be seen that the field strength in the negative polarity is less than the field strength in the positive polarity around the neutral line by about 300 Gauss. Hence, the derived flows well matches with the predicted siphon flow (flow from the lower field strength to the higher field strength). However, to map the flow over the observed region, a high resolution Stokes polarimetry is needed. The flow speed derived about the neutral line is 1 to 1.5 km/sec.

Table 5.3: Results from the fit of the composite profile for V-profiles taken from eight positions around the neutral line

Pixel number	fill fraction	Velocity (km/sec)
66	0.8	1.44
70	0.7	-0.48
72	0.6	-0.48
74	0.6	-1.44
76	0.5	-1.44
78	0.4	-0.48
80	0.3	-0.48
84	0.2	-0.48

5.7 Vector Field Map of NOAA 8951

The sunspot KKL 21551 (NOAA 8951) is observed on 13 April 2000 using the polarimeter and the CCD detector (Det-2) described in Chapter 3 of this thesis. The observational configuration is shown in Figure 5.8. The observational parameters are listed in Table 5.3. The instrumental polarisation is removed from the observed Stokes profiles using the continuum polarisation observation as it was done for the active region NOAA 8516 and explained in the last chapter. The corrected Stokes profiles are then inverted for the physical parameters in the observed region using the inversion code explained in section 5.4 of this chapter. Figure 5.9 shows the observed and fitted Stokes profiles at a point of the observed active region. Figure 5.10 shows the total field strength, LOS inclination and the azimuthal angle of the magnetic field derived using the code for a slit position which passes through the umbral portion of the active region NOAA 8951. The error bars marked in these figures are the errors

derived from the fit using the ASP code. The length of the error bar is equal to five times the error value derived by the inversion code. The dashed line in the top figure of the Figure 5.10 is the arbitrarily scaled intensity plot to show the minimum intensity region or the umbral position. The step width for the slit position used for these observations is 2.75 arcsec. Even though the step width is not sufficient for a high resolution vector field map, the map was produced using these observations. The vector fields for the regions between the slit positions are derived by interpolation using the 'congrid' routine in IDL (Interactive Data Language). Figure 5.11 shows the map produced after the interpolation. The 180° ambiguity in the azimuth was corrected manually by looking at the sudden jumps in the azimuthal map. The gray scale image shows the longitudinal field strength. More the intensity represents more longitudinal field strength. The transverse field strength is depicted as the magnitude of the arrow shown and the direction of the arrow is determined from the azimuthal angle of the field. The length of the arrow is proportional the transverse field strength. The rectangular box marked on the Figure 5.11 is the slit positions used for the observation and the width corresponds to the slit width used. The intensity map of the region is depicted as contours. The numbers marked are the direction in which the slit was stepped to complete the mapping of the active region.

5.8 Conclusions

The ASP code used to invert the Stokes profiles from the Advanced Stokes Polarimeter data was modified to take the Stokes profiles input from the KTT polarimeter. The results from these inversion for the active region NOAA 8516 was discussed. The inversion code used cannot reproduce the asymmetries or peculiar profiles observed since the code uses the approximation that all the atmospheric parameters are constant in the line forming region and the source function is linear with optical depth. With the polarimetric accuracy at the KTT this approximation is good enough to pro-

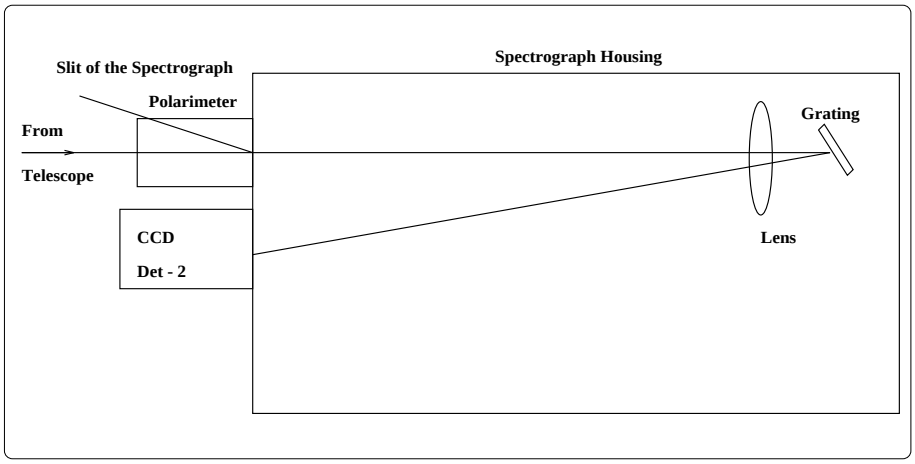

Figure 5.8: The schematic view of the observational setup used for the vector field measurement of the active region NOAA 8951.

duce a vector field map of active regions and get an average magnetic field strength in these regions. However, with this accuracy we found that the V-measurement shows very peculiar profiles near a magnetic neutral line. We used a two magnetic component model rather than one magnetic and one non-magnetic component and fitted these peculiar profiles. These fittings gives us the LOS velocity present in those regions. The velocity flow in the bi-polar region of NOAA 8516 has been observed near the neutral line and it shows flows similar to siphon flow. The velocity of the flow calculated is around 1 - 1.5km/sec.

Even though the step size of the slit used was 2.75 arcsec, atleast three times poorer than what is needed for a high resolution vector field map, we produced a map for active region NOAA 8951 by using these inversion results. We used a linear interpolation to fill the vector field data between the slit positions. The map produced was reasonably good and can be used for a morphological studies with a resolution of about 5 arcsec. To conclude, the polarimeter and the inversion code works fine. The vector field mapping of sunspot is possible with the existing instrument as shown by the vector field map of a single spot near the disc center.

Table 5.4: Observational parameters of the spectrograph, the Stokes polarimeter and the active region NOAA 8951.

Spectral Range covered:	6296.50 to 6306.85Å.
Spectral Resolution :	138 210 at 6302Å.
Dispersion:	20.25mÅ per pixel.
Spatial Scale:	0.121 arcsec per pixel.
Slit Width:	0.55 arcsec.
Step Width:	2.75 arcsec.
Integration Time:	200 to 500 msec.
First Mirror Position:	East.
Date of Observation:	13 April 2000.
Time in UT Hours:	02:30 Hrs.
Field of View :	52.25×68.0 arcsec^2
Active region :	NOAA 8951.
Position on the sun:	N17°E8°.

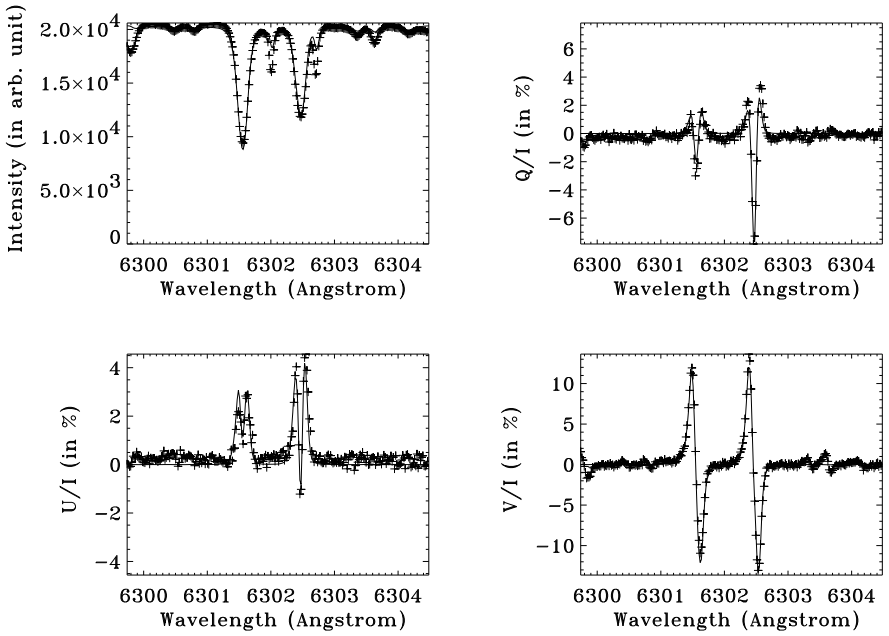

Figure 5.9: The observed and fitted Stokes profile at a point in the active region NOAA 8951.

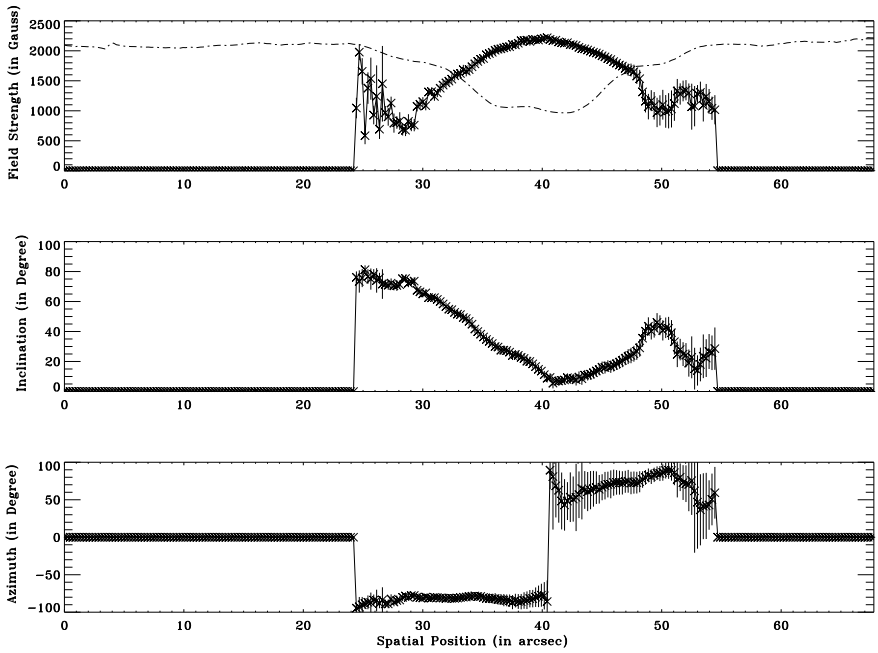

Figure 5.10: Plot of the parameters which specifies the vector magnetic field at a slit position which passes through the umbra of the sunspot. The top figure shows the field strength variation (as solid line), the dashed line is the plot of the intensity to show the position of the umbra or the minimum intensity region. The middle plot is the line of sight inclination and the bottom one is for the azimuthal angle. The error bars are the errors derived from the fit and the length is five times the error derived.

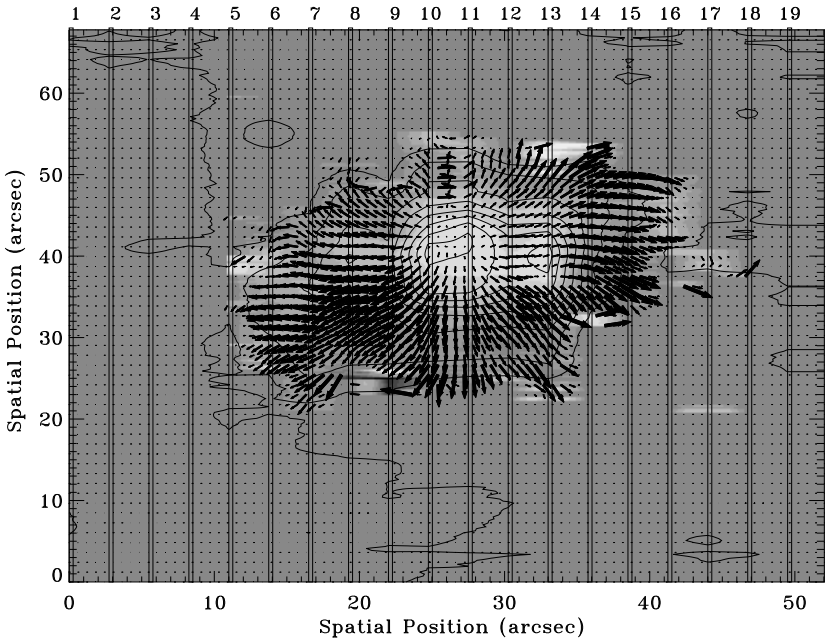

Figure 5.11: Vector field map of the observed region for the active region NOAA 8951. The vertical rectangular box shown in the figure corresponds to the slit and the width corresponds to the slit width used. The grey scale represents the longitudinal field strength and the arrows represent the transverse field strength. The contour map is the intensity contour of the observed region. The data points in between the slit positions were obtained using interpolation.

Chapter 6

Summary & Conclusions and Future Improvements

6.1 Summary & Conclusions

Solar polarimetry is the study of the polarisation state of the light received from the sun. It is well known that the consistent study of magnetic fields on the sun is achieved through polarimetry. The size of the magnetic structures on the sun varies from small scale bright points to large scale sunspots. Many physical processes in the solar atmosphere are related to the magnetic field present. Hence, the study of the magnetic field is considered to be important to understand the physics of these processes which are happening on the sun. There are two possible mechanisms adopted until now to study the magnetic fields present on the sun,

- Zeeman Effect, to study the strong magnetic fields with field strengths of about one kilogauss.
- Hanle effect, to study the weak diffuse magnetic fields with field strength of few

tenths of Gauss.

We adopted Zeeman effect to study the magnetic fields present in the active regions. Zeeman effect is the splitting of the line profiles when the atom emitting the light is subjected to a magnetic field. The amount of splitting is proportional to the magnetic field strength. The direct way of finding the splitting is possible only in the infrared wavelength because of the fact that the magnetic field splitting is larger than the Doppler broadening at this wavelength. However, the different Zeeman components of the line becomes polarised and the state of the polarisation depends on the strength of the magnetic field and its orientation with respect to the line of sight. A consistent study of the magnetic field is possible purely because of this polarised Zeeman broadened nature of the line. The study of the polarisation state of the line from the magnetic region gives us the strength as well as the orientation of the magnetic field vector.

To study the magnetic fields of sunspots, a vector magnetic field measurement is necessary. There are two approaches which can be followed,

- Stokes spectro-polarimeter, which obtains the complete spectral line of an one dimensional region and the other dimension is obtained by scanning the slit of the spectrograph across the image. The disadvantage with this type of measurement is the longer time required to get one complete vector magnetograph. However, the accuracy in the vector magnetic field measurement is very good.

- Vector magnetograph, which obtains the Stokes vector for two dimensional region at one particular wavelength. Even though this system can obtain a vector magnetogram very fast, the accuracy in the calculation of the magnetic field is limited.

Since we are interested in the sunspot magnetic field measurement and because of the availability of very high spectral resolution spectrograph at Kodaikanal tower tunnel telescope, we adopted the Stokes spectro-polarimetric approach.

6.1.1 Instrumental Polarisation

The main disadvantage with the Kodaikanal tower tunnel telescope (KTT) is the oblique reflecting optics which changes the polarisation state of the input beam. The input and the output Stokes vector through any optics is related by a 4×4 real square matrix called the Mueller matrix. The Mueller matrix of a single mirror reflection is a function of X^2 and τ, where X^2 is the ratio of the modulus square of the amplitude reflection co-efficient of two orthogonally polarised beam one parallel to the plane of incidence and the other perpendicular to it and τ is the phase difference between the two.

These X^2 and τ are in turn is a function of the angle of incidence 'i' and the complex refractive index (η,κ) of the mirror coating where η and κ are the real and imaginary part of the complex refractive index. The angles of incidence for solar observation can be calculated through spherical trigonometry. Hence, the problem reduces to the measurement of the complex refractive index of the mirror coating. Since the Kodaikanal tower tunnel telescope is a three mirror system, the complex refractive index of each mirror coating and the associated Mueller matrix has to be found out to calculate the complete Mueller matrix of the combined system.

An optical setup using a Babinet Compensator (BC) as an ellipsometer for the measurement of the refractive index of each mirror has been developed. The simulation of the experimental setup was done to understand the importance of errors in some critical parameters. The brief results of this simulation, for 1% accuracy in the determination of η and κ, are,

- The κ determination is more accurate with τ measurements.
- The η determination is better with X^2 measurements.
- The error in the angle of incidence measurement should be less than $\pm 0.1^\circ$.
- The angle of incidence should be in the range 70° - 90° because of the large

changes of the X^2 and τ in those region for a small change in the angle of incidence.

- Minimum of 8-bit digitisation levels are needed for data acquisition.
- Wedge angle of BC should be less than 5°.

With these inputs, an optical system for the ellipsometer was developed and the refractive index of the three mirrors of the coelostat system were measured. A theoretical model for the bulk material was compared with the observed measurements and we found that a simple bulk aluminium model is inconsistent with the experimental results. This inconsistency can be removed by considering an extra aluminium oxide layer above the bulk aluminium. This extra oxide layer has to be included in the model for the accurate calculation of the instrumental polarisation. Ignoring this oxide layer can introduce an error in the instrumental polarisation model and hence in the magnetic field measurements. These complex refractive index measurements with the model which includes the oxide layer were used to calculate the combined Mueller matrix of the Kodaikanal tower telescope.

A self-calibration method also been studied to deduce the instrumental polarisation from the observed data. This study showed the possibility of obtaining the instrumental polarisation parameter, which here is the refractive index of the reflecting mirrors and the oxide layer thicknesses, from the observed continuum polarisation. By fitting the daily variation of the continuum polarisation to a model of the Kodaikanal tower telescope, the instrumental polarisation parameters were derived. These values were then used to calculate the Mueller matrix at any instant of time during the observations.

6.1.2 Stokes Polarimeter

A Stokes polarimeter was developed for the measurement of the vector magnetic field of sunspot. The polarimeter developed consist of a rotating polarising prism and an

insertable Quarter Waveplate (QWP). The advantage of a rotating polarising prism over the rotating Half Waveplate (HWP) is the complete removal of the polarimeter's cross-talk from circular polarisation V into the linear polarisation Q and U. However, the disadvantage of a rotating polarising prism is that the output analysed beams polarisation azimuth will be rotating with the rotation of the analyser. Hence it will produce spurious polarisation signals if the post polarimetric instruments are sensitive to polarisation. In our case, the response of the diffraction grating of the spectrograph was different for different azimuths of the analysed beam which introduces a large spurious polarisation signal. It can be shown that the response of the grating can be made equal for the orthogonal polarisation states by introducing an additional QWP after the analyser, to change the output analysed beam into circularly polarised beam. Also, a polariser can be introduced instead of the QWP just for Q measurement to make the grating response same for both I+Q and I-Q measurement. We used the later approach to minimise the response changes for the orthogonal polarisation measurements.

The polarimeter was tested in the laboratory and in the field. In the laboratory each component of the polarimeter was tested for its accuracy and the combined system also been tested. A CCD based polarisation interferometric technique is developed using BC to find the retardance accuracy of the QWP. In the field, a 100% linearly polarised sunlight is sent through the polarimeter and the spectrograph to test the complete system accuracy.

6.1.3 Off-line correction of the Instrumental polarisation

The self-calibration method was used to correct for the instrumental polarisation. The continuum polarisation was observed in the disk center of the sun and the Mueller matrix of the combined optical system of the KTT was derived from these observations. The daily variation of the continuum polarisation was used to derive the coating pa-

rameters, the refractive index of the coating and the thicknesses of the oxide layer formed on it. These derived parameters were then used to find the complete Mueller matrix of the KTT for the time of observations of active regions. The inaccuracies in the measurement of the continuum polarisation will introduce a spurious polarisation signal. The maximum spurious polarisation which could be produced because of this experimental inaccuracies were calculated. The error in the Mueller matrix for the inversion because of these experimental inaccuracies is given by,

$$[\Delta M] = \pm\tfrac{1}{2} \begin{pmatrix} 0.0500 & 0.0040 & 0.0030 & 0.0005 \\ 0.0030 & 0.0015 & 0.0040 & 0.0100 \\ 0.0040 & 0.0500 & 0.0030 & 0.0050 \\ 0.0006 & 0.0050 & 0.0100 & 0.0050 \end{pmatrix},$$

This matrix when multiplied with the input Stokes vector will give the amount of spurious polarisation signals produced in I, Q, U and V. By assuming three different cases with case(i) as Q = 0, U = 0 & V = 20%, case(ii) as Q = 10%, U = 0 & V = 0 and case(iii) as Q = 0, U = 10% & V = 0, the maximum residual errors in the inverted Stokes profiles are calculated. It was found that the maximum amplitude of spurious polarisation signal produced after the correction of the instrumental polarisation is, 0.5% in Q, 0.9% in U and 0.2% in V.

6.1.4 Vector Field Measurement of Sunspots

The polarimeter is used to observe the vector magnetic fields of some sunspots. The Stokes profiles of the Zeeman sensitive Fe I lines 6301.5Å and 6302.5Å were observed. The Mueller matrix of the instrument and the telescope was inverted from the observed profile to get the 'clean' Stokes profiles. An inversion code using the HAO methodology was used to invert the observed Stokes profiles to get the magnetic field parameters. The inversion code derives nine atmospheric parameters and they

are, (i) The magnetic field strength, B, (ii) Magnetic field inclination from the line of sight (LOS), ψ, (iii) Azimuthal angle of the magnetic field vector, χ, (iv) LOS velocity represented as the line core position, λ_o^m, (v) Line depth, η_0, (vi) Doppler width, $\Delta\lambda_D$, (vii) Damping factor, a, (viii) Constant background source function, B_0, (ix) The slope of the source function, B_1. The tenth parameter, scattered light 'f' is taken as another free parameter if the inversion includes the total intensity. The ASP code also derives the errors in each of the fitted parameters. The vector field measurement of the sunspot NOAA 8516 was discussed.

The disturbed profile in the magnetic neutral line can be a way of diagonising the velocities present in those region. The inversion code which we used cannot handle such situations. A two magnetic component model was used to extract the velocity information from these disturbed profiles of the bi-polar active region NOAA 8516. Also, the analysis of the flow near the neutral line suggest that there is a flow from the low field strength polarity to the higher field strength opposite polarity. This flow looks very similar to the siphon flow suggested for the Evershed effect. The magnitude of the flow was found out to be between 1 to 1.5km/sec.

A vector field map of the active region NOAA 8951 was made. It was found from the map that the polarimeter and the inversion code works satisfactorily. Even though the accuracy in the polarisation measurement is not better than 1%, the measurements of higher field strengths are less prone to error. The field values derived for the sunspot agrees well with the field values derived by Mees Solar Observatory which gives us confidence in the whole system.

6.2 Future Improvements

Even though the system as of now can be used for studies of sunspot magnetic field with field strength greater than 700 Gauss, we list some of the improvements which will definitely boost the performance of the whole system.

6.2.1 Guider

The main difficulty with the existing system is that the unavailability of an automatic guiding system. At present the slow telescope drift is compensated by manually adjusting the second mirror using a hand-set with coarser and finer control switch. We found that the telescope drift can be minimised by fine tuning the frequency of the revolution of the first mirror. This makes the image to be stable to within 5 arcsec for about 15 minutes. At present a full Stokes profile at a slit position needs about 3 minutes and hence a telescope drift of about an arcsec is unavoidable. Also, the mapping of an active region was achieved by moving the image on the slit of the spectrograph. This again was done manually and we could go up to a step size of 0.5 mm which corresponds to 2.75 arcsec. The mapping with this coarse step size does not give us a real good vector field map for the study of the azimuthal changes and also the finer structures in the penumbral regions. Hence, an automatic guider which receives the error signal from a limb motion measurement need to be developed to improve the performance. This also will enable us to improve the step size and get a good vector field map.

6.2.2 Slit-jaw Picture

Even though the mapping of an active region could be possible with a good guider and finer step size, it is always advantageous to have a slit-jaw picture. This will enable us to look for any systematic effects because of image motion. Any systematic mis-alignments of the two orthogonal polarisation measurements (for example I$\pm$Q) can also be studied. This slit-jaw picture can also be used to study the horizontal flows in and around the active regions. With a Fabry-Perot filter, this slit-jaw can be used to derive the LOS velocity simultaneously around the region of observations by looking at a line whose Lande factor is zero (insensitive to magnetic field). For example the line $\lambda\lambda$5434Å can be used for this purpose.

6.2.3 Polarimeter

The polarimeter used here is a single beam polarimeter. An order of accuracy can be easily improved by using a double beam system. For example, with a calcite beam displacer and using waveplates this can be implemented without much difficulty (Semel, 1980; Bianda, Solanki, and Stenflo, 1998a). A polarisation accuracy of 0.1% or less is possible with this improvement. Also, with the improvement of the polarimetric accuracy, the calculation of the instrumental polarisation becomes accurate once the continuum polarisation is measured accurately and hence the reduction in the spurious polarisation signal produced because of the inaccurate calibration of the instrumental polarisation. These improvements can be used to study some of the characteristics of Hanle effect on the sun (Bianda, Stenflo, and Solanki, 1998b; Bianda, Stenflo, and Solanki, 1999). The asymmetries in the Stokes profiles which are present everywhere on the sun can be studied in much detail (Solanki, 1997; Sanchez Almeida, 1999). These studies are not possible with the current accuracy of the polarimeter.

6.3 Anomalous Zeeman effect

Apart from the normal Zeeman effect, anomalous Zeeman effect can happen on certain spectral lines. Figure 6.1 and 6.2 shows a case of anomalous Zeeman effect. The spectral line observed were Ti I and Sc I with rest wavelength at $\lambda\lambda$6303.769Å and $\lambda\lambda$6305.74Å.

The normal Zeeman effect is the case when only the upper level, involved in the atomic transition gets split into three whereas the lower level does not split. In other words, using quantum mechanics this corresponds to a transition from $\mathbf{J}_l = \mathbf{0} \rightarrow \mathbf{J}_u = \mathbf{1}$. In the case of anomalous Zeeman effect, the transition can be from any $\mathbf{J}$ levels in which case both the lower and higher level can split into many number of components. Nevertheless, the group of transitions that generates

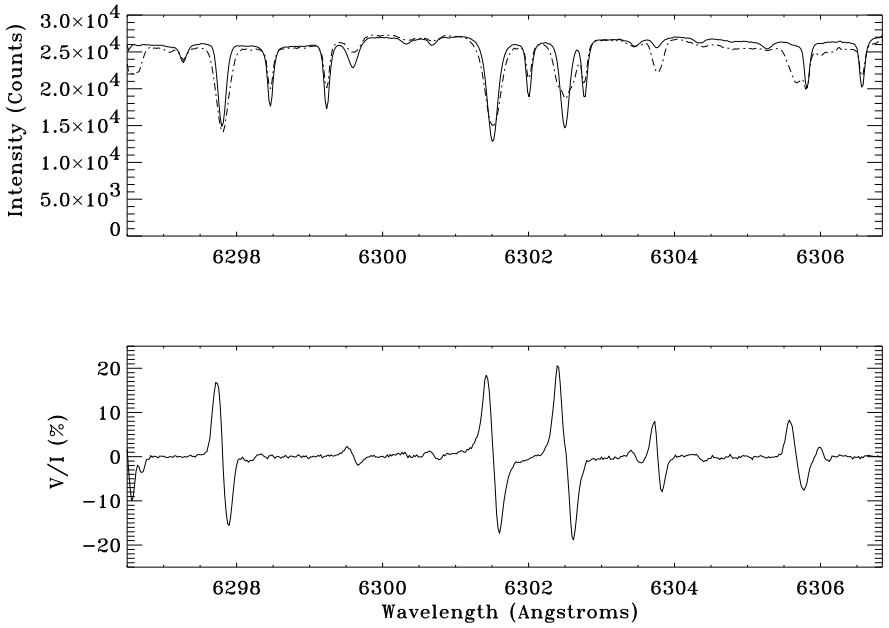

Figure 6.1: The spectral line profiles observed in the umbral region of the sunspot NOAA 8951. The top figure shows the intensity profile of a particular point in the umbral region of the sunspot. The solid line is the intensity spectrum obtained in the photosphere and the dashed line is the intensity spectrum obtained in the umbra of the sunspot. The bottom figure shows the V-profile of the same region. See the text for the details.

the π components in an anomalous splitting pattern has the same angular and polarisation properties as that of a classical π component and the same applies to the σ components. However, in the case of anomalous splitting, the profile function or the absorption coefficient defined as $\kappa(v)$ has to be weighed for the various individual transitions with the corresponding transitions strengths S_q (where 'q' represents the π or σ components) and sum over all the contributions. *i.e.,*

$$\phi_q = \sum_{M_u} S_q(M_l, M_u) H_q(a, v_q). \tag{6.1}$$

Where, $H_q(a,v_q)$ is the voigt profile function defined in Chapter 5 (section 5.4). The $\kappa(v)$ is related to the voigt profile. The subscript 'q' varies between 0 and ± 1 with q = 0 represents the π component and q = ± 1 represents the two σ components.

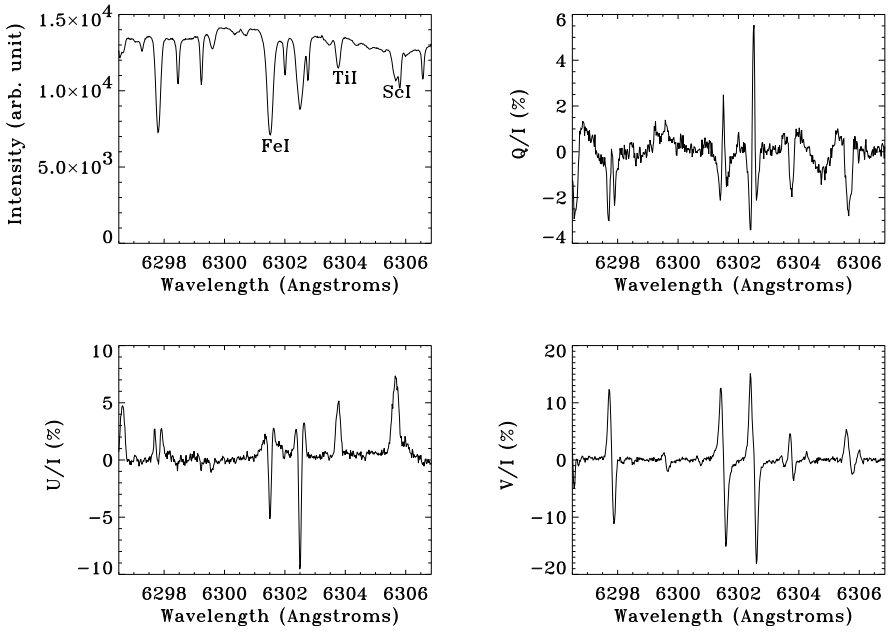

Figure 6.2: The four Stokes profiles of a spatial position which showed significant signals in all the profiles of the Ti I and Sc I observed in the active region NOAA 8951.

Table 6.1 lists the transition strengths for the allowed transitions.

The detailed calculations of π and σ component profiles should use the Equation 6.1 to superpose the weighted contributions from all the allowed transitions between the Zeeman sublevels. In many cases, it is useful to approximate the anomalous splitting pattern with that of a normal Zeeman triplet. The wavelength positions of the σ components are the same as the positions of the centers of gravity of the q = $\pm$1 components in the anomalous splitting pattern. The Lande factor that would have this splitting is g_{eff}, representing the effective Lande factor of the anomalous splitting pattern. From this definition, it can be derived that,

$$g_{eff} = \frac{1}{2}(g_u + g_l) + \frac{1}{4}(g_u - g_l)[J_u(J_u + 1) - J_l(J_l + 1)]. \quad (6.2)$$

Where g_u and g_l are the Lande factor of the upper and lower level of the transitions. The observed Ti I and Sc I shows the anomalous splitting and the atomic parameters for this transition is tabulated in Table 6.2.

Table 6.1: Unnormalised expressions for the transition strengths, S_q.

J_u - J_l	q = 0	q = -1	q = 1
0	$2M_u^2$	$(J_u + M_u)(J_u - M_u + 1)$	$(J_u - M_u)(J_u + M_u + 1)$
+1	$2(J_u^2 - M_u^2)$	$(J_u + M_u)(J_u - M_u - 1)$	$(J_u - M_u)(J_u - M_u - 1)$
-1	$2[(J_u+1)^2-M_u^2]$	$(J_u - M_u + 1)(J_u - M_u + 2)$	$(J_u + M_u + 1)(J_u + M_u + 2)$

Table 6.2: Atomic Parameters for the Ti I and Sc I spectral lines observed.

Wavelength	g_u	g_l	g_{eff}	$\mathbf{J}_u$	$\mathbf{J}_u$
6303.769 (Ti I)	0.75	1.08	0.915	3	3
6305.74 (Sc I)	1.20	1.20	1.20	$\frac{5}{2}$	$\frac{3}{2}$

Figure 6.1 and 6.2 shows the observed Stokes profiles at two different points on the sunspot present in the active region NOAA 8951. Figure 6.1 shows the intensity and the V-profile observed in the umbral region of the spot. The top figure in Figure 6.1 shows the intensity spectrum from the photosphere (solid line) and from the umbral region (dashed line) of the sunspot. The intensity spectrum from the umbral region is scaled arbitrarily to plot both in the same figure. It can be seen from this top figure that the Ti I and Sc I present at the wavelength positions $\lambda\lambda$6303.769Å and $\lambda\lambda$6305.74Å has more line depth in the umbral region than in the photosphere. These lines are low excitation lines and forms only in the cooler region of the sunspot and hence more prominently seen in the umbral spectrum than in the photospheric spectrum. This property will have the advantage that the field strengths derived from this will not be affected by the scattered light from the photosphere. Hence, the field strengths and other parameters derived from these lines will have minimum influence from the photospheric light. In the V-profile these two lines shows a prominent signal which can be used to derive the field strength.

Figure 6.2 shows the Stokes profiles of the same spectral region in a penumbral point of the sunspot. It can be seen from this figure that the Q and U profile are completely different from the Q and U-profile of a normal Zeeman triplet as seen in the two Fe I lines ($\lambda\lambda$6301.5Å and $\lambda\lambda$6302.5Å). This urges for a proper analysis of the data including the transitions strength of all the split components rather than taking it as a normal Zeeman effect. An inversion code needs to be written for such anomalous Zeeman effect. The formation height of the Ti I line is about 70 km above the formation height of the Fe I lines (Lites *et al.,* 1998). So, this will enable us to study the height variation of the magnetic field strength and other physical parameters.

Appendix:A

Algorithm for the Polarimetric Mueller matrix

This appendix discusses the algorithm used for charaterising the Mueller matrix or the response matrix of the polarimeter developed for this thesis. The polarimeter operates in three modes for the measurement of I±Q, I±U, and I±V. The input Stokes vector for all these three modes are taken as $[I, Q, U, V]^T$ where superscript 'T' refers to the transpose operation. The algorithm is derived for these three modes separately. An algorithm is also derived to remove the systematic errors produced by the polarimeter because of the misalignments of the optical components.

A.1 Mode - I

This mode of operation is used to measure the I±Q. The Glan-Thompson prism (GTP) used as the analyser in the polarimeter is rotated and stops at the reference position sensed by the IR-sensor (refer to Chapter 3 for the details of the polarimeter). This position is set at 45° with respect to the slit direction. The optical components involved in this measurement are the GTP and the grating. For ideal measurements of I±Q, the transmission axis of the GTP will be placed at 45° and -45° with respect to the slit direction. Assuming an idealistic nature of the GTP, the Mueller matrix of the GTP can be written as,

$$[M_P] = \frac{1}{2} \begin{pmatrix} 1 & c_{21} & s_{21} & 0 \\ c_{21} & c_{21}^2 & c_{21}s_{21} & 0 \\ s_{21} & c_{21}s_{21} & s_{21}^2 & 0 \\ 0 & 0 & 0 & 0 \end{pmatrix},$$

where, c_{21} and s_{21} are the cosine and sine of twice the angle θ made by the transmission axis of the GTP and the slit direction. Ideally this θ will be 45° and -45° for the two orthogonal polarisation measurement (*i.e.,* I±Q). Let us assume a generalised Mueller matrix for the grating as,

$$[M_G] = \begin{pmatrix} G_{11} & G_{12} & G_{13} & G_{14} \\ G_{21} & G_{22} & G_{23} & G_{24} \\ G_{31} & G_{32} & G_{33} & G_{34} \\ G_{41} & G_{42} & G_{43} & G_{44} \end{pmatrix}.$$

The grating response to the input polarisation has been measured for the grating used for the polarimetric observations (see Chapter 3 for the details). From these measurements, it was found that the grating acts as a partial polariser with G_{13} & G_{14} equals to zero. The response of the grating is maximum along the grating groove direction compared to the perpendicular direction. Taking the reference axis as the grating groove direction, the misalignments of the grating groove direction and the slit direction need to be corrected. If θ_2 is the misalignment angle, then the Mueller matrix for the rotation is given by,

$$[M_R] = \begin{pmatrix} 1 & 0 & 0 & 0 \\ 0 & c_{22} & s_{22} & 0 \\ 0 & -s_{22} & c_{22} & 0 \\ 0 & 0 & 0 & 0 \end{pmatrix}.$$

Where, c_{22} and s_{22} are the cosine and sine of twice the angle θ_2, respectively. Ideally this angle should be 0°. Multiplying these three Mueller matrices in order, *i.e.,* Grating matrix (M_G), rotation matrix (M_R), and GTP matrix (M_P) (in other words, $M_G M_R M_P$), the output intensity can be written as,

$$I'_{out} = [I + Qc_{21} + Us_{21}][G_{11} + G_{12}\cos(2(\theta_1 - \theta_2)) + G_{13}\sin(2(\theta_1 - \theta_2))]. \quad \text{(A.1)}$$

Where θ_1 and θ_2 are the angles made by the transmission axis of the GTP and the groove direction of the grating with the slit direction respectively. The two orthogonal measurements were done with θ_1 at 45° and -45° for the measurement of I±Q. However, in the real situation, there will be a relative error in positioning of the GTP. Assuming $\delta\theta_1$ as the error in the positioning of the GTP, the values for the θ_1 for these two measurements will be, $45° + \delta\theta_1$ and -45°. Similarly, assuming an error of $\delta\theta_2$ for the positional accuracy of the grating with respect to the slit direction, then θ_2 will be equal to $\delta\theta_2$. By substituting these values into the Equation A.1, the two output intensity of the two orthogonal position of the GTP can be calculated. By subtracting and adding these two output intensity, the observed Q/I can be calculated and is given by,

$$\frac{Q'_{obs}}{I'_{obs}} = -\frac{A + B}{1 + A.B}. \quad \text{(A.2)}$$

Where,

$$\begin{aligned} A &= \frac{Q}{I}\cos(2\delta\theta_1) + \frac{U}{I}\sin(2\delta\theta_1), \\ B &= \frac{G_{12}}{G_{11}}\sin(2(\delta\theta_1 - \delta\theta_2)). \end{aligned}$$

Note that while deriving the above equations, the value of G_{13} and G_{14} are taken as zero. Equation A.2 gives the observed linear polarisation Q in terms of the input Stokes vector with the errors in the alignment of the polarimetric optics. It can be seen that the circular polarisation does not come into this measurement and hence there will not be any circular to linear cross-talk because of the polarimeter.

A.2 Mode - II

The mode - II measurement is for the other linear polarisation component known as 'U' (*i.e.,* I±U). The GTP is fixed at a position -45° from the reference position marked by the IR sensor (*i.e.,* along the slit direction). The angle θ_1 now for this measurement will be 0° and 90° for the two orthogonal polarisation measurement (*i.e.,* I±U). Since, the response of the grating along the groove direction and perpendicular to it is different, a polaroid called as compensating polaroid, is inserted behind the polarimeter (close to the slit). The transmission axis of this compensating polaroid is set at 45° so that this does not introduce any response difference between the two orthogonal positions with the GTP. Let us assume that θ_2 be the angle of the transmission axis of the polaroid with respect to the slit direction (ideally this angle should be 45°). Now, the combined Mueller matrix for this measurement can be obtained by multiplying the individual Mueller matrices in the following order, the Grating matrix (M_G), the rotation matrix to match the axis with the groove direction (M_R), the compensating polaroid matrix (M_P, similar to the GTP matrix except for the angle difference), and the GTP matrix (M_P) (*i.e.,* $M_G M_R M_P M_P^{GTP}$). Assuming $\delta\theta_1$ and $\delta\theta_2$ to be the errors in positioning the GTP at 0° and the compensating polaroid at 45°, then the calculation of the output intensity at two orthogonal positions of the GTP will give the value of the observed U. The calculated value of U is given by,

$$\frac{U'_{obs}}{I'_{obs}} = \frac{A+B}{1+A.B}. \tag{A.3}$$

Where,

$$\begin{aligned} A &= \frac{Q}{I}\sin(2\delta\theta_1) - \frac{U}{I}\cos(2\delta\theta_1), \\ B &= \sin(2(\delta\theta_1 - \delta\theta_2)). \end{aligned}$$

Note that the grating response does not come into the final equation as the output for this configuration is a linearly polarised with constant polarisation direction because of the fixed compensating polaroid. However, because of this extra polaroid, the

exposure time has been increased by five times in order to get similar signal-to-noise ratio compared to the first one. Equation A.3 gives the output linear polarisation U in terms of the input Stokes vector. In this case also, the circular to linear cross-talk because of the polarimeter is zero.

A.3 Mode - III

The mode - III measurement is for the circular polarisation, V. In this case, a quarter-wave plate (QWP) is inserted in front of the polarimeter (close to the source) to convert the circular polarisation input to a linear polarisation and measure the linear polarisation as measured for Q or U. In our case, it was measured like Q. The compensating polaroid is removed for this measurement. The Mueller matrix of a linear retarder with its fast axis at θ_1 is given by,

$$[M_{LR}] = \begin{pmatrix} 1 & 0 & 0 & 0 \\ 0 & c_{21}^2 + s_{21}^2\beta & c_{21}s_{21}(1-\beta) & -s_{21}\mu \\ 0 & c_{21}s_{21}(1-\beta) & s_{21}^2 + c_{21}^2\beta & c_{21}\mu \\ 0 & s_{21}\mu & -c_{21}\mu & \beta \end{pmatrix}.$$

Where, c_{21} and s_{21} are the cosine and sine of twice the angle made by the fast axis of the linear retarder with the slit direction respectively. β and μ are the cosine and sine of the retardance of the linear retarder. For ideal configuration, θ_1 should be zero or 90° and the retardance of the QWP should be 90°. The combined Mueller matrix for this configuration can be obtained by multiplying the individual Mueller matrices in the following order, grating response matrix (M_G), rotation matrix for the grating (M_R), matrix for the GTP (M_P), and the matrix for the QWP (M_{LR}) (*i.e.,* $M_G M_R M_P M_{LR}$). From the calculation of the output intensity from this combined Mueller matrix for the two orthogonal polarisation position, the value for the observed

V can be calculated and is given by,

$$\frac{V'_{obs}}{I'_{obs}} = -\frac{A+B}{1+A.B}. \tag{A.4}$$

Where,

$$\begin{aligned} A &= Q_p \cos(2\delta\theta_1) - U_p \sin(2\delta\theta_1), \\ B &= \sin(2(\delta\theta_1 - \delta\theta_2)). \end{aligned}$$

$\delta\theta_1$ and $\delta\theta_2$ are the misalignment of the QWP fast axis and the GTP axis. Q_p and U_p are related to the input Stokes vector and defined as,

$$\begin{aligned} Q_p &= [c_{21}^2 - s_{21}^2 \sin(\delta\Delta)]Q + [c_{21}s_{21}(1+\sin(\delta\Delta))]U - s_{21}\cos(\delta\Delta)V, \\ U_p &= [c_{21}s_{21}(1+\sin(\delta\Delta))]Q + [s_{21}^2 - c_{21}^2 \sin(\delta\Delta)]U + c_{21}\cos(\delta\Delta)V. \end{aligned}$$

$\delta\Delta$ is the error in the retardance and c_{21}, s_{21} are the cosine and sine of twice the angle made by the GTP with the slit direction. Equation A.4 gives the output observed circular polarisation in terms of the input Stokes vector with the optical alignment errors in the polarimeter. The Equations A.2, A.3, and A.4 are used to get the polarimeter response to an input Stokes vector. However, in order to eliminate the spurious polarisation produced because of the mis-alignments, the corrected Stokes profiles need to be calculated from the observed Stokes profiles. In order to generalise the above three modes, let us assume the following,

- $\delta\theta_1$ as the error in the positioning of the QWP.
- $\delta\theta_2$ as the error in the initial position of the GTP.
- $\delta\theta_3$ as the error in the positioning of the compensating polaroid.
- $\delta\theta_4$ as the error in the positioning of the grating groove.
- $\delta\Delta$ as the error in the retardance of the QWP.

With the above assumptions, the generalised equations for the three different modes of operation can be derived as,

$$\frac{Q'_{obs}}{I'_{obs}} = -\frac{A_1 + A_2}{1 + A_1 A_2}, \tag{A.5}$$

where,

$$\begin{aligned} A_1 &= \frac{Q}{I}\cos(2\delta\theta_2) + \frac{U}{I}\sin(2\delta\theta_2), \\ A_2 &= \frac{G_{12}}{G_{11}}\sin(2(\delta\theta_2 - \delta\theta_4)). \end{aligned}$$

For the U-measurement,

$$\frac{U'_{obs}}{I'_{obs}} = \frac{B_1 + B_2}{1 + B_1 B_2}, \tag{A.6}$$

where,

$$\begin{aligned} B_1 &= \frac{Q}{I}\sin(2\delta\theta_2) - \frac{U}{I}\cos(2\delta\theta_2), \\ B_2 &= \sin(2(\delta\theta_2 - \delta\theta_3)). \end{aligned}$$

For the V-measurement,

$$\frac{V'_{obs}}{I'_{obs}} = -\frac{C_1 + C_2}{1 + C_1 C_2}, \tag{A.7}$$

where,

$$\begin{aligned} C_1 &= Q_p\cos(2\delta\theta_2) - U_p\sin(2\delta\theta_2), \\ C_2 &= \frac{G_{12}}{G_{11}}\sin(2(\delta\theta_2 - \delta\theta_4)). \end{aligned}$$

with

$$\begin{aligned} Q_p = (\sin^2(2\delta\theta_1) - \cos^2(2\delta\theta_1)\sin(\delta\Delta))\frac{Q}{I} \\ - \cos(2\delta\theta_1)\sin(2\delta\theta_1)(1 + \sin(\delta\Delta))\frac{U}{I} \\ - \cos(2\delta\theta_1)\cos(\delta\Delta)\frac{V}{I}, \\ U_p = -\cos(2\delta\theta_1)\sin(2\delta\theta_1)(1 + \sin(\delta\Delta))\frac{Q}{I} \\ + \cos^2(2\delta\theta_1) - \sin^2(2\delta\theta_1)\sin(\delta\Delta)\frac{U}{I} \\ - \sin(2\delta\theta_1)\cos(\delta\Delta)\frac{V}{I}. \end{aligned}$$

For the idealistic case of $\delta\theta_1 = \delta\theta_2 = \delta\theta_3 = \delta\theta_4 = \delta\Delta = 0$, Equations A.5, A.6, and A.7 reduces to,

$$\begin{aligned}
\frac{Q'_{obs}}{I_{obs}} &= -\frac{Q}{I}, \\
\frac{U'_{obs}}{I_{obs}} &= -\frac{U}{I}, \\
\frac{V'_{obs}}{I_{obs}} &= \frac{V}{I}.
\end{aligned}$$

Equations A.5, A.6, and A.7 are used to calculate the output Stokes vector for an input Stokes vector with the polarimeter as the instrument. However, in the actual situation the observed Stokes vector are available and the input Stokes vector has to be inferred from this observed Stokes vector. These can be found out by solving the above three equations (*i.e.,* Equations A.5, A.6, and A.7). The solution is written as,

$$\frac{Q}{I} = A'_1 + A'_2, \tag{A.8}$$

where,

$$\begin{aligned}
A'_1 &= -\frac{(\frac{Q'_{obs}}{I'_{obs}} + A)\cos(2\delta\theta_2)}{A\frac{Q'_{obs}}{(I'_{obs}+1)}}, \\
A'_2 &= -\frac{(\frac{U'_{obs}}{I'_{obs}} - B)\sin(2\delta\theta_2)}{B\frac{U'_{obs}}{(I'_{obs}-1)}}.
\end{aligned}$$

For input U,

$$\frac{U}{I} = B'_1 + B'_2, \tag{A.9}$$

where,

$$\begin{aligned}
B'_1 &= -\frac{(\frac{Q'_{obs}}{I'_{obs}} + A)\sin(2\delta\theta_2)}{A\frac{Q'_{obs}}{(I'_{obs}+1)}}, \\
B'_2 &= \frac{(\frac{U'_{obs}}{I'_{obs}} - B)\cos(2\delta\theta_2)}{B\frac{U'_{obs}}{(I'_{obs}-1)}}.
\end{aligned}$$

For input V,

$$\frac{V}{I} = C'_1 + C'_2 + C'_3, \tag{A.10}$$

where,

$$
\begin{aligned}
C_1' &= \frac{(\frac{V'_{obs}}{I'_{obs}} + C)}{C\frac{V'_{obs}}{(I'_{obs}+1)}}, \\
C_2' &= \frac{Q}{I}(D+E), \\
C_3' &= \frac{U}{I}(F+G).
\end{aligned}
$$

The values of A, B, C, D, E, F, and G are given as,

$$
\begin{aligned}
A &= (\frac{G_{12}}{G_{11}})\sin(2(\delta\theta_2 - \delta\theta_4)), \\
B &= \sin(2(\delta\theta_2 - \delta\theta_3)), \\
C &= (\frac{G_{12}}{G_{11}})\sin(2(\delta\theta_2 - \delta\theta_4)), \\
D &= \cos(2\delta\theta_2)(\sin^2(2\delta\theta_1) - \cos^2(2\delta\theta_1)\sin(\delta\Delta)), \\
E &= -\sin(2\delta\theta_2)\cos(2\delta\theta_1)\sin(2\delta\theta_1)(1+\sin(\delta\Delta), \\
F &= \cos(2\delta\theta_2)\cos(2\delta\theta_1)\sin(2\delta\theta_1)(1+\sin(\delta\Delta), \\
G &= -\sin(2\delta\theta_2)[\cos^2(2\delta\theta_2) - \sin^2(2\delta\theta_2)\sin(\delta\Delta)].
\end{aligned}
$$

Equations A.8, A.9, and A.10 gives the corrected Stokes profile from the observed Stokes profiles. This algorithm is needed and used to remove the polarimetric responses from the observed data.

Bibliography

[1] Abeles, F.: 1971, *Physics of Thin Films*, **6**, 151.

[2] Adam, M. G.: 1963, *Mon. Not. Roy. Astr. Soc.*, **126**, 135.

[3] Ananth, A. V., Venkatakrishnan, P., Narayanan, R. S., and Bhattacharyya, J. C.: 1994, *Solar Phys.*, **151**, 231.

[4] Auer, L. H., Heasley, J. N., and House, L. L.: 1977, *Solar Phys.*, **55**, 47.

[5] Avery, D. G.: 1952, *Proc. Phys. Soc.*, **B65**, 425.

[6] Azzam, R. M. A., and Bashara, N. M.: 1977, *Ellipsometry and Polarised Light*, North-Holland Publishing Company, New York.

[7] Babcock, H. W.: 1953, *Astrophys. J.*, **118**, 387.

[8] Balasubramaniam, K. S., Venkatakrishnan, P., and Bhattacharyya, J. C.: 1985, *Solar Phys.*, **99**, 333.

[9] Balasubramaniam, K. S.: 1988, *Stokes Polarimetry and the Measurement of Vector Magnetic Fields in Solar Active Regions*, Ph. D. Thesis, Dept. of Physics, Indian Institute of Science, Bangalore, India.

[10] Balasubramaniam, K. S., and West, E. A.: 1991, *Astrophys. J.*, **382**, 699.

[11] Bappu, M. K. V.: 1967, *Solar Phys.*, **1**, 151.

[12] Beckers, J. M.: 1969, *Solar Phys.*, **9**, 372.

[13] Beckers, J. M., and Schroter, E. H.: 1969, *Solar Phys.*, **10**, 384.

[14] Bellot Rubio, L. R., Ruiz Cobo, B., and Collados, M.: 2000, *Astrophys. J*, **535**, 475.

[15] Bernosconi, P.: 1997, *Stokes Vector-Polarimetry: Observation and Analysis of Solar Magnetic Fields*, Ph. D. Thesis, Swiss Federal Institute of Technology, Zurich.

[16] Bevington, P. R.: 1969, *Data Reduction and Error Analysis for the Physical Sciences*, McGraw-Hill Book Company, New York.

[17] Bhattacharyya, J. C.: 1965, *Studies of solar magnetic and velocity fields*, Ph. D thesis, Dept. of Science, University of Calcutta, India.

[18] Bianda, M., Solanki, S. K., and Stenflo, J. O..: 1998a, *Astron. Astrophys.*, **331**, 760.

[19] Bianda, M., Stenflo, J. O., and Solanki, S. K.: 1998b, *Astron. Astrophys.*, **337**, 565.

[20] Bianda, M., Stenflo, J. O., and Solanki, S. K.: 1999, *Astron. Astrophys.*, **350**, 1060.

[21] Bigelow: 1889, *The Solar Corona*, Smithsonian Institution.

[22] Born, M., and Wolf, E.: 1984, *Principles of Optics*, Pergoman Press, Sixth Edition.

[23] Bosch, S., and Monzonis, F.: 1995, *J. Opt. Soc. Amer. A*, **12**, 1375.

[24] Bruls, J. H. M., Lites, B. W., and Murphy, G. A.: 1991, *in: Solar Polarimetry*, November, L. J. (ed.), **11**, 444.

[25] Burge, D. K., and Bennett, H. E.: 1964, *J. Opt. Soc. Amer.*, **54**, 1428.

[26] Capitani, C., Cavallini, F., Ceppatelli, G., Landi Degl′ Innocenti, E., Landi Degl′ Innocenti, M., Landolfi, M., and Righini, A.: 1989, *Solar Phys.*, **120**, 173.

[27] Chidester, S. D., Harvey, J. W., and Hubbard, R. P.: 1991, *Applied Optics*, **30**, 12.

[28] Chipman, R.: 1995, *Optical Engineering*, **34**, 1636.

[29] Chou, C., Huang, Y. C., and Chang, M.: 1997, *J. Opt. Soc. Amer. A*, **14**, 1367.

[30] Clarke, D. and Grainger, J. F.: 1971, *Polarized Light and Optical Measurement*, Pergamon Press, Oxford.

[31] Condon, E. U., and Shortley, G. H.: 1935, *Theory of Atomic Spectra*, Cambridge Univ. Press, Cambridge.

[32] del Toro Iniesta, J. C., and Ruiz Cobo, B.: 1996a, *Solar Phys.*, **164**, 169.

[33] del Toro Iniesta, J. C., and Ruiz Cobo, B.: 1996b, *in: Forum Themis*, Mein M., and Shala-Brechot, S. (eds.), Observatoire de Paris-Meudon.

[34] Demidov, M. L.: 1991, *Solar Phys.*, **135**, 193.

[35] Elmore, D. F., Lites, B. W., Tomczyk, S., Skumanich, A., Dunn, R. B., Schuenke, J. A., Streander, K. V., Leach, T. W., Chambellan, C. W., Hull, H. K., and Lacey, L. B.: 1992, *Proceedings SPIE*, **1746**, 22.

[36] Evershed, J.: 1909, *Mon. Not. R. Astr. Soc.*, **69**, 454.

[37] Fluri, D. M. and Stenflo, J. O.: 1999a, *in: Proceedings of an International Workshop on Solar Polarization*, Nagendra, K. N., and Stenflo, J. O. (eds.,) p. 171.

[38] Fluri, D. M. and Stenflo, J. O.: 1999b, *Astron. Astrophys.*, **341**, 902.

[39] Gerrard, A. and Burch, J. M.: 1975, *Introduction to Matrix methods in Optics*, John Wiley and Sons, New York.

[40] Green, R. M.: 1984, *Spherical Astronomy*, Cambridge Univ. Press. Cambridge.

[41] Grigorjev, V. M., and Katz, J. M.: 1972, *Solar Phys.*, **22**, 119.

[42] Hagyard, M. J., Cumings, N. P., West, E. A., and Smith, J. E.: 1982, *Solar Phys.*, **80**, 33.

[43] Hagyard, M. J., Cumings, N. P., and West, E. A.: 1983, *in: Proceedings of a workshop on solar physics and interplanetary traveling phenomena*, Sp. Sc. Lab. Preprint 84-116.

[44] Hale, G. E.: 1908, *Astrophys J.*, **28**, 315.

[45] Hariharan, P., and Sen, D.: 1960, *J. Sci. Instrum.*, **37**, 278.

[46] Hariharan, P.: 1996, *Optical Engineering*, **35**, 3335.

[47] Hass, G., Heaney, J. B., and Hunter, W. R.: 1982, *Physics of Thin Films*, **12**, 1.

[48] Heavens, O. S.: 1991, *Optical Properties of Thin Solid Films*, Dover Publications, New York.

[49] Hjortsberg, A.: 1980, *Thin Solid Films*, **69**, L15.

[50] Holt, J. N.: 1972, *A single absorption line inversion method and the application to a solar spectrogram*, Ph. D. Thesis, Dept. of Phys., Univ. of Queensland, Australia.

[51] Jefferies, J., Lites, B. W., and Skumanich, A.: 1989, *Astrophys. J.*, **343**, 920.

[52] Jerrard, H. G.: 1948, *J. Opt. Soc. Amer.*, **38**, 35.

[53] Kawakami, H.: 1983, *Publ. Astron. Soc. Japan*, **35**, 459.

[54] Keller, C. U., Solanki, S. K., Steiner, O., and Stenflo, J. O.: 1990, *Astron. Astrophys.*, **233**, 583.

[55] Keppens, R., and Martinez Pillet, V.: 1996, *Astron. Astrophys.*, **316**, 229.

[56] Landi Degl′ Innocenti, E., and Landi Degl′ Innocenti, M.: 1972, *Solar Phys.*, **27**, 319.

[57] Landolfi, M., Landi Degl′ Innocenti, E., and Arena, P.: 1984, *Solar Phys.*, **93**, 269.

[58] Leighton, R. B.: 1959, *Astrophys. J.*, **130**, 366.

[59] Leka, K. D., Mickey, D. L., and LaBonte, B. J.: 1999, *in: Proceedings of an International Workshop on Solar Polarization*, Nagendra, K. N., and Stenflo, J. O. (eds.), p. 305.

[60] Lide, D. R.: 1995, *Hand Book of Chemistry and Physics*, CRC Press, New York.

[61] Lin, C. H., Chou, C., and Chang, K. S.: 1990, *Applied Optics*, **29**, 5159.

[62] Lites, B. W.: 1987, *Applied Optics*, **26**, 3838.

[63] Lites, B. W., Skumanich, A., Rees, D. E., and Murphy, G. A.: 1988, *Astrophys. J.*, **330**, 493.

[64] Lites, B. W., and Skumanich, A.: 1990, *Astrophys. J.*, **348**, 747.

[65] Lites, B. W., Scharmer, G. B., and Skumanich, A.: 1990, *Astrophys. J.*, **355**, 329.

[66] Lites, B. W., Dunn, R. B., Elmore, D. F., Tomczyk, S., Skumanich, A., and Streander, K. V.: 1992, *American Astronomical Society Meeting*, **180**, 1201.

[67] Lites, B. W., Martinez Pillet. V., and Skumanich, A.: 1994, *Solar Phys.*, **155**, 1.

[68] Lites, B. W., Low, B. C., Martinez Pillet, V., Seagraves, P., Skumanich, A., Frank, Z. A., Shine, R. A., and Tsuneta, S.: 1995, *Astrophys. J.*, **446**, 877.

[69] Lites, B. W.: 1997, *Reports on Astronomy*, IAU Transactions A., Vol XXIII.

[70] Lites, B. W., Thomas, J. H., Bogdan, T. J., and Cally, P. S.: 1998, *Astron. Astrophys.*, **497**, 464.

[71] Livingston, W., and Harvey, J: 1971, Kitt Peak National Observatory Contribution No. 558.

[72] Makita, M., and Nishi, K.: 1970, *Ann. Tokyo Astron. Obs.*, **253**, 2857.

[73] Makita, M.: 1979, *Publ. Astron. Soc. Japan.*, **31**, 575.

[74] Makita, M., Hamana, S., and Nishi, K.: 1985, *Measurements of Solar Vector Magnetic Fields*, Hagyard, M. J. (ed.), NASA CP-2374, p. 173.

[75] Martinez Pillet, V., Lites, B. W., and Skumanich, A.: 1997, *Astrophys. J.*, **474**, 810.

[76] Mathew, S. K.: 1998, *A Study of Solar Magnetic and Velocity Fields*, Ph. D. Thesis, Dept. of Physics, Gujarat Univ., India.

[77] Mickey, D. L., Canfield, R. C., Labonte, B. J., and Leka, K. D., Waterson, M. F., Weber, H. M.: 1996, *Solar Phys.*, **168**, 229.

[78] Montesinos, B., and Thomas, J. H.: 1997, *Nature*, **390**, 485.

[79] Mueller, H.: 1948, *J. Opt. Soc. Amer.*, **38**, 661.

[80] Muller, R.: 1985, *Solar Phys.*, **100**, 237.

[81] Moe, O. K.: 1967, *in: Structure and Development of Solar Active Regions* Deinzer, W., Knolker, M., and Voigt, H. H.(eds.), Vandenhoeck and Ruprecht: Gottingen, p. 25.

[82] Moe, O. K.: 1968, *Solar Phys.*, **4**, 267.

[83] Nakadate, S.: 1990, *Applied Optics*, **29**, 242.

[84] Nilsson, P. O.: 1968, *Applied Optics*, **7**, 435.

[85] November, L. J.: 1991, *in: Solar Polarimetry*, November, L. J. (ed.), **11**, 149.

[86] Parker, E. N.: 1955, *Astrophys. J*, **121**, 491.

[87] Parker, E. N.: 1984, *Astrophys. J*, **280**, 423.

[88] Povel, H.: 1995, *Optical Engineering*, **34**, 1870.

[89] Rachovsky, D. N.: 1962, *Izv. Krymsk. Astrofiz. Obs.*, **27**, 148.

[90] Rees, D. E.: 1969, *Solar Phys.*, **10**, 268.

[91] Riedling, K.: 1987, *Ellipsometry for Industrial Applications*, Springer-Verlag, New York.

[92] Rimmele, T. R., Radick, R. R.: 1998, *Proceedings SPIE*, **3353**, 72.

[93] Ruedi, I., Solanki, S. K., and Livingston, W.: 1995, *Astron. Astrophys.*, **293**, 252.

[94] Ruiz Cobo, B., and del Toro Iniesta, J. C.: 1992, *Astrophys. J.*, **398**, 375.

[95] Ruiz Cobo, B., and del Toro Iniesta, J. C.: 1994, *Astron. Astrophys.*, **283**, 129.

[96] Rust, D. M., and O'brynne, J. W.: 1991, *in: Solar Polarimetry*, **11**, 74.

[97] Sanchez Almeida, J., and Martinez Pillet, V.: 1992, *Astron. Astrophys.*, **260**, 543.

[98] Sanchez Almeida, J., and Lites, B. W.: 1992, *Astrophys. J.*, **398**, 359.

[99] Sanchez Almeida, J.: 1999, *in: Proceedings of an International Workshop on Solar Polarizations*, Nagendra, K. N., and Stenflo, J. O. (eds.), p. 251.

[100] Sankarasubramanian, K. and Venkatakrishnan, P.: 1996, *Solar Phys.*, **167**, 1.

[101] Sankarasubramanian, K., Samson, J. P. A., and Venkatakrishnan, P.: 1999, *in: Proceedings of an International Workshop on Solar Polarization*, Nagendra, K. N., and Stenflo, J. O. (eds.), p. 313.

[102] Schuster: 1892, *Rep. B. A. A. S*, 634.

[103] Sears, F. H.: 1913, *Astrophys. J.*, **38**, 99.

[104] Semel, M.: 1980, *Astron. Astrophys.*, **91**, 369.

[105] Severny, A. B.: 1964a, *Publ. Crim. Astrophys. Obs.*, **31**, 126.

[106] Severny, A. B.: 1964b, *Publ. Crim. Astrophys. Obs.*, **31**, 209.

[107] Severny, A. B.: 1965, *IAU Symposium 22*, Ed. R. Lust and D. Reidel.

[108] Shurcliff, W. A.: 1962, *Polarized Light*, Harvard Univ. Press, Cambridge.

[109] Shyu, L. H., Chen, C. L., and Su, D. C.: 1993, *Applied Optics*, **32**, 4228.

[110] Sigwarth, M., Balasubramaniam, K. S., Knolker, M., and Schmidt, W.: 1999, *Astron. Astrophys.*, **349**, 941.

[111] Skumanich, A., and Lites, B. W.: 1987, *Astrophys. J.*, **322**, 473.

[112] Skumanich, A., and Lites, B. W.: 1991, *in: Solar Polarimetry*, November, L. J. (ed.), **11**, 307.

[113] Skumanich, A., Grossmann-Doerth, U., and Lites, B. W.: 1992, *in: Methods de Determination des Champs Magnetiques Solarires et Stellaires*, Faurobert-Scholl, M., Frisch, H., and Mein, N. (eds.), Obs. de Paris, Meudon, p 57.

[114] Skumanich, A., Lites, B. W., and Martinez Pillet, V.: 1994, *in: Solar Surface Magnetism*, Rutten, R. J., and Schrijver, C. J. (eds.), NATO ASI ser. C. **433**, Kluwer Academic Pub., Dordrecht, p. 99.

[115] Skumanich, A., Lites, B. W., and Seagraves, P.: 1997, *in: Forum Themis: Science with Themis*, Mein, N., and Sahal-Brechat, S., (eds.), paris, Meudon.

[116] Solanki, S. K., Ruedi, I., and Livingston, W.: 1992a, *Astron. Astrophys.*, **263**, 312.

[117] Solanki, S. K., Ruedi, I., and Livingston, W.: 1992b, *Astron. Astrophys.*, **263**, 339.

[118] Solanki S. K.: 1993, *Space. Sci. Rev.*, **63**, 1.

[119] Solanki, S. K., Walther, U., and Livingston, W.: 1993, *Astron. Astrophys.*, **277**, 639.

[120] Solanki, S. K., Montavon, C. A. P., and Livingston, W.: 1994, *Astron. Astrophys.*, **283**, 221.

[121] Solanki, S. K. and Bruls, J. H. M. J.: 1994, *Astron. Astrophys.*, **286**, 269.

[122] Solanki, S. K.: 1997, *in: 1st Advances in Solar Physics Euroconference. Advances in Physics of Sunspots*, Schmieder, B., del Toro Iniesta, J. C., and Vazquez, M. (eds.), ASP Conf. Ser. Vol. 118, p. 178.

[123] Stenflo, J. O.: 1973, *Solar Phys.*, **32**, 41.

[124] Stenflo, J. O.: 1984, *Applied Optics*, **23**, 1267.

[125] Stenflo, J. O.: 1994, *Solar Magnetic fields: Polarized Radiation Diagnostics*, Kluwer Academic Publishers, Dordrecht.

[126] Stepanov, V. E.: 1960, *Izv. Krymsk. Astrofiz. Obs.*, **19**, 20.

[127] Stepanov, V. E., and Severny, A. B.: 1962, *Publ. Crim. Astrophys. Obs.*, **28**, 166.

[128] Stockman, H. S.: 1982, *Proceedings SPIE*, **331**, 76.

[129] Stromer: 1892, *Somptes Rendus*, Feb. 20, p. 1911.

[130] Thomas, J. H.: 1992, *in: Sunspots: Theory and Observations*, Thomas, J. H and Weiss, N. O., (eds.), NATO ASI Series C Vol. 375, Kluwer Academic, Dordrecht.

[131] Treanor, P. J.: 1960, *Mon. Not. Roy. Astr. Soc.*, **120**, 412.

[132] Tousey, R.: 1939, *J. Opt. Soc. Amer.*, **29**, 235.

[133] Unno, W.: 1956, *Publ. Astron. Soc. Japan.*, **8**, 108.

[134] van Ballegooijen, A. A.: 1986, *Astrophys. J.*, **311**, 1001.

[135] Walter, D. G.: 1978, *Hand Book of Optics*, McGraw-Hill Book Company, New York.

[136] Wang, Z., Bryanston-cross, P. J., and Whitehouse, D. J.: 1996a, *Optics and Laser Technology*, **28**, 417.

[137] Wang, Z., Graca, S., Bryanston-cross, P. J., and Whitehouse, D. J.: 1996b, *Optical Engineering*, **35**, 2327.

[138] West, E. A., and Smith, M. H.: 1995, *Optical Engineering*, **34**, 1574.

[139] Westendorp Plaza, C., del Toro Iniesta, J. C., Ruiz Cobo, B., and Martinez Pillet, V.:1997a, *in: 1st Advances in Solar Physics Euroconference. Advances in Physics of Sunspots*, Schmieder, B., del Toro Iniesta, J. C., and Vazquez, M. (eds.), ASP Conf. Ser. Vol. 118, p. 202.

[140] Westendorp Plaza, C., del Toro Iniesta, J. C., Ruiz Cobo, B., Martinez Pillet, V., Lites, B. W., Skumanich, A.: 1997b, *Nature*, **389**, 47.

[141] Westendorp Plaza, C., del Toro Iniesta, J. C., Ruiz Cobo, B., Martinez Pillet, V., Lites, B. W., Skumanich, A.: 1998, *Astrophys. J.*, **494**, 453.

[142] White, H. E.: 1934, *Introduction to Atomic Spectra*, McGraw-Hill, New York.

[143] Wittman, A.: 1974a, *Solar Phys.*, **35**, 11.

[144] Wittman, A.: 1974b, *Solar Phys.*, **36**, 29.

[145] Wittman, A.: 1977, *Astron. Astrophys.*, **54**, 175.

[146] Ye Shi-hui: 1994, *Magnetic Fields of Celestial Bodies*, Kluwer Academic Publishers, Dordrecht.

[147] Zeeman, P: 1896, *Proc. R. Acad. Amsterdam*, **5**, 181.

[148] Zwann, C.: 1978, *Solar Phys.*, **60**, 213.